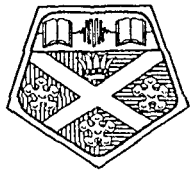

THE UNIVERSITY OF STRATHCLYDE

Glucose Sensing Based on the Intrinsic Time Dependent Fluorescence from Proteins: Application of pulsed ultraviolet light emitting diodes and sol-gel derived matrices.

Colin Douglas McGuinness
Photophysics Research Group
Department of Physics

Thesis submitted to the University of Strathclyde in part fulfillment of the requirements for the Degree of Doctor of Philosophy.

May 2006

Copyright

To Helen

Publications

C. D. McGuinness, K. Sagoo, D. McLoskey and D. J. S. Birch, "A new sub-nanosecond LED at 280nm: Application to protein fluorescence", *Meas. Sci. Technol.*, **15**, (2004), L19.

C. D. McGuinness, K. Sagoo, D. McLoskey and D. J. S. Birch, "Selective excitation of tryptophan fluorescence decay in proteins using a subnanosecond 295 nm light-emitting diode and time-correlated single-photon counting", *Appl. Phys. Lett.*, **86**, (2005), 261911.

C. D. McGuinness, A. M. Macmillan, K. Sagoo, D. McLoskey and D. J. S. Birch, "Excitation of fluorescence decay using a 265 nm light-emitting diode: evidence for aqueous phenylalanine rotamers.", *Appl. Phys. Lett.*, **89**, (2006), 063901.

Conference Presentations

F. Hussain, J. C. Pickup, C. D. McGuinness, O. J. Rolinski & D. J. S. Birch, *Glucose Sensing in Sol Gels*, Poster Presentation at 8th MAFS, Prague (2003).

C. D. McGuinness & D. J. S. Birch, *Biosensors - Proteins Encapsulated in Sol Gel Glasses,* Oral and Poster Presentation at 4th PIMoP, Prague (2004).

C. D. McGuinness, K. Sagoo, D. McLoskey & D. J. S. Birch, *A New 280 nm Pulsed Source for Exciting Fluorescence,* Poster Presentation at Photon04, Glasgow (2004)

C. D. McGuinness, K. Sagoo, D. McLoskey & D. J. S. Birch, *A New Pulsed LED Source for Exciting Fluorescence - Application to Biosensors,* Poster Presentation at RSC Young Researchers Meeting, RAL Oxfordshire (2004).

C. D. McGuinness, K. Sagoo, D. McLoskey & D. J. S. Birch, *A New Pulsed LED Source for Exciting Fluorescence - Application to Biosensors,* Poster Presentation at SUPA Launch Meeting, Edinburgh (2005).

C. D. McGuinness, K. Sagoo, D. McLoskey & D. J. S. Birch, *A sub-nanosecond 295nm LED: selective tryptophan excitation & a step towards Lab-On-A-Chip Biosensors*, Poster Presentation at SUPA Photonics Division Launch, Glasgow (2005).

C. D. McGuinness, J. C. Pickup & D. J. S. Birch, *Sol Gel Biosensors,* Poster Presentation at 9th MAFS, Lisbon (2005).

C. D. McGuinness, D. J. S. Birch & J. C. Pickup, *Glucose Sensing Using Time-Correlated Single-Photon Counting,* Poster Presentation at RSC Semi-conductor Photocatalysis and Applied Photochemistry, Runcorn (2006).

Acknowledgements

Firstly, I would like to thank my supervisor, Professor David Birch, for his help, guidance and encouragement, and indeed for the opportunity to complete this PhD project.

I would also like to thank Professor John Pickup, our colleague at Guy's Hospital, London, for guidance and discussions on non-invasive glucose sensing.

I am indebted to John Broadfoot in electronics support, John Revie in mechanical support and Paul Thompson in optics support for their indispensable technical assistance and expertise, as if it were not for them, there would be no results in this thesis!

David McLoskey and Kulwinder Sagoo at Horiba Jobin Yvon IBH Ltd., Glasgow, provided the new UV LEDs for my research, and for this I owe them great thanks. Indeed I owe thanks to the Glasgow team at Horiba Jobin Yvon IBH Ltd. for the use of equipment for the completion of certain experiments.

I would like to express my gratitude to Alaine Martin of the Department of Pure and Applied Chemistry for carrying out my sol-gel NMRs despite her busy schedule, and to Dr. John Parkinson for his assistance in the interpretation of the spectra.

I would also like to thank my colleagues, past and present, in the Photophysics Research Group for showing me the ropes, for many useful discussions on various aspects of this project and for an enjoyable time in the group.

Thanks are extended to the Engineering and Physical Sciences Research Council (EPSRC) for the tenure of the research studentship.

Many thanks to Helen Barley for proof reading this manuscript and for her continued support and encouragement over the years.

My greatest debt, however, is to my parents, who have endlessly supported me throughout my whole university education and without them; none of this would be possible.

Glossary

A300	Aerosil 300 silica
ADC	Analogue-to-Digital Converter
aTf	Apo-transferrin
Chisq (χ^2)	Goodness of fit indicator
ConA	Concanavalin A
D	*dextro* – Latin for "right". See §2.5.1 – Amino Acids
FWHM	Full-Width Half-Maximum
[G]	Glucose concentration
GFP	Green Fluorescent Protein from *Aequorea victoria* jellyfish
H^+	"Extra" proton in aqueous acid
HSA	Human Serum Albumin
kDa	kilodaltons
L	*levo* – Latin for "left". See §2.5.1 – Amino Acids
LED	Light-emitting diode
MCA	Multichannel Analyser
mol (or M)	moles
NATA	N-acetyl-L-tryptophanamide
NMR	Nuclear Magnetic Resonance
PBS	Phosphate buffered saline
ppm	parts per million
R^2	Co-efficient of determination
TAC	Time-to-amplitude converter
TCSPC	Time-correlated single-photon counting
TMOS	Tetramethoxysilane
TPHC	Time-to-pulse-height conversion, TAC output to ADC
UV	Ultraviolet
W	Tryptophan
X*	Excited state of molecule or complex "X"

Abstract

The use of intrinsic tryptophan fluorescence is a key tool available to the protein researcher when investigating protein dynamics. Until recently, the sources required for excitation of intrinsic fluorescence decays from proteins were bulky, expensive or high maintenance. Compact aluminium gallium nitride ultraviolet light-emitted diodes have been demonstrated in this work to be ideal sources for excitation of protein intrinsic fluorescence decays, and associated fluorescence anisotropy, with ease of use, fast collection times and reproducible results. Their compact nature lends themselves to the eventual fabrication of "lab-on-a-chip" metabolite sensors based on fluorescence decays.

Specific molecular recognition has many applications in medicine. It is possible to sense for metabolites by entrapping biomolecules in silica sol-gel derived matrices, providing the resultant sol-gel is biocompatible, porous and ultraviolet transparent. This work shows that this can be achieved in using simple methods. Utilising the new pulsed ultraviolet light emitting diodes, it is now easy to use the information contained within a biomolecule's intrinsic fluorescence decay as a possible method for *in vivo* monitoring. The ease of use of these devices has also provided further insight in to the way in which the fluorescence of the enzyme hexokinase is influenced by the binding of glucose. In addition, as shown in this work, they can provide information on the nature of the sol-gel microenvironment in a quick and convenient way.

Contents

1

Introduction

Photophysics can be considered as the cornerstone of the interaction of radiation with molecular systems, since it is an integral constituent of every other interaction where there is a loss of electronic excitation energy[1]. Luminescence, quenching and energy transfer are the important aspects of photophysics. There are two types of luminescence: fluorescence and phosphorescence. Fluorescence is of particular interest in analytical sciences as it is highly sensitive and can detect fluorophores in concentrations of a few parts per billion. In addition, fluorescence emission occurs in the time scale of 10^{-10} sec – 10^{-5} sec, and so is comparable to that of many molecular processes. With this fluorescence lifetime, time-resolved fluorescence is widely practiced due to the increased information available from the data compared with simple steady state or stationary measurements.

Fluorescence spectroscopy and its multiple applications to the life sciences have undergone rapid development. In recent years this progress has been driven by the numerous technical advances in time resolution, methods of data analysis and improved instrumentation. These developments have enabled research in numerous areas of science from basic analytical chemistry to practical clinical applications.

The early works of many scientists, such as Debye and Edwards[2], have shown that proteins in aqueous solution possess intrinsic fluorescence in the near ultraviolet region, which can be used for structural and physiochemical studies of proteins. For

some time now, scientists have exploited the characteristics of intrinsic fluorescence from biosystems such as enzymes, proteins and cells to probe their function, or for their use in sensors. For example, intrinsic tryptophan fluorescence has been used to monitor the unfolding and refolding mechanisms of apohorseradish peroxidase[3].

The use of extrinsic probes is also widely utilised. Recently, *Aequorea victoria* Green Fluorescent Protein (GFP) has become the extrinsic probe of choice in many applications, for example the expression of GFP from adeno-associated virus and adenovirus vectors within the bronchial epithelium of New Zealand white rabbits, by incorporating filters for detection of GFP into an existing video endoscopy fibre optic system[4]. Fluorescence from GFP has also been used to monitor protein phosphorylation in single living cells[5], and to monitor the folding of *Escherichia Coli* (*E-Coli*)[6].

However, with the rapidly increasing use of the time-resolved fluorescence from tryptophan as a method for monitoring specific functions, the need has never been greater for affordable, simple and compact ultraviolet pulsed excitation sources. Ultraviolet sources that are currently in use are flashlamps, lasers or synchrotrons. However these are either expensive or high maintenance, and require extensive knowledge and care to operate, and for this reason, are off-putting to many protein researchers. It is shown in this work that the use of light-emitting diodes is an excellent, and preferable alternative to more established sources for protein fluorescence decays.

Silica sol-gel synthetic chemistry is adopted to encapsulate the proteins whilst still retaining biological functions. Many researchers have investigated silica sol-gels for over 150 years. In the early days, silica sol-gels had little uses, as the chemistry behind their synthesis was little understood. Today, silica sol-gels are used in a variety of applications and research from bone repair and implants, to bioreactor design, to optical sensors. They lend themselves to these applications due to their

inert nature. In this work, the porous nature of silica can be exploited for encapsulation of a protein, acting as a fluorescent sensor, and diffusion of metabolites to the protein. In conjunction with the new UV LEDs and miniaturised detectors, it can pave the way for further research in to "lab-on-a-chip" sensors.

Lab-on-a-chip essentially describes a system that can integrate many laboratory functions on a single integrated circuit perhaps just a few millimeters in diameter. In this context, the idea of lab-on-a-chip biosensors capable of handling small volumes and incorporating all components, such as light source, probe, detector etc, is the ultimate goal. The major advantages of such systems are compactness, higher throughput analysis, lower fabrication costs and a safe platform for biological analysis because of large integration of functionality.

The work presented in this thesis ultimately seeks to exploit the benefits of ultra-violet light-emitting diodes in exciting intrinsic enzyme fluorescence decays, and use the information in those decays as a means of investigating time-resolved fluorescence as a means of detecting metabolites of interest. Silica sol-gels are known for their porous nature and ability to trap molecules. This work also pursues the concept of enzyme entrapment as a step towards glucose sensing in sol-gels.

Chapter 2 describes the theoretical aspects of fluorescence, fluorescence anisotropy and associated parameters required in the work presented. Also included is a brief outline of the basic building blocks of proteins and their function. Tryptophan is the most widely used intrinsically fluorescent amino acid in proteins, and the one used in this work, therefore the photophysics of tryptophan are discussed.

Chapter 3 contains a brief description of the specialist solid-state chemistry and physics involved in the construction of light-emitting diodes (LEDs). The instrumental characteristics of pulsed LEDs with wavelength emissions of 265 nm, 280 nm and 295 nm are illustrated. A comparison of the LEDs for fluorescence

decays is made with a typical co-axial nanosecond flashlamp, yielding comparable and reproducible decay parameters but with several advantages. Also illustrated is a comparison of the 280 nm device and the 295 nm device in the fluorescence depolarisation of human serum albumin. This demonstrates the importance of 295 nm excitation in molecules containing tryptophan and tyrosine because excitation at 280 nm gives unwanted energy transfer from tyrosine to tryptophan. The usefulness of the device is further demonstrated with excitation of fluorescence decays and depolarisation of other biomolecules with particular clinical importance, and their rotational decay times used to calculate their molecular volumes consistent with measurements using other techniques. Finally, the strengths of the 265 nm device are exemplified by way of rapid collection of fluorescence decays from low concentration and weakly fluorescent aqueous phenylalanine. The data provided further supports the rotamer model for phenylalanine; a model accepted for tyrosine and tryptophan.

Chapter 4 presents the synthetic conditions required to produce silica-sol gel matrices suitable for labile protein encapsulation. There are a number of research groups providing many different sol-gel encapsulation techniques, based on various precursors. This work will discuss the techniques of sol-gel production based on synthesis from sodium silicate solution and from the inorganic precursor, tetramethoxysilane.

Chapter 5 concerns further investigation of the use of the glucose transport enzyme hexokinase as a potential sensor for glucose, with applications in patients with diabetes mellitus. Discussed in the chapter are possible processes to account for the variation in fluorescence decay of hexokinase with increasing glucose concentrations. The investigation not only give an opportunity to measure glucose concentrations using intrinsic fluorescence decays from hexokinase, but also provide an insight into the mechanisms present during glucose binding. Also included is the encapsulation of the protein in a sol-gel derived matrix for possible use as an *in vivo*

glucose sensor. Results are discussed and the limitations of the concept using sol-gel encapsulation techniques are presented in chapter 4. Other fluorescence techniques, although perhaps not suitable for sensors, may provide some information on the binding and are also demonstrated.

2

Background Theory

2.1 Photophysical Processes

A photophysical process is defined as a physical process resulting from the electronic excitation of a molecule or system of molecules by non-ionizing electromagnetic radiation (photons)[1]. The process is one that does not involve any chemical changes, as a photochemical change does. The unimolecular electronic transitions that take place in systems can be easily represented by the Jabłoński diagram[7]. Figure 2.1 illustrates the electronic energy levels that may be occupied by molecules and the transitions that can take place upon excitation. The energy associated with each level is related to its vertical position. S_0 represents the ground state with S_1, S_2, etc representing higher energy singlet states and T_1, T_2, etc representing triplet states. Each electronic energy level is also split into levels of vibrational and rotational energy where the total energy of a system (E) is the sum of the electronic (E_e), vibrational (E_v) and rotational (E_r) energies. The typical energy difference between electronic, vibrational and rotational levels is 30,000 cm^{-1}, 1,000 cm^{-1} and 10 cm^{-1} respectively[1].

Transitions involving only rotational energy levels yield the rotational absorption spectrum, which can be observed in the far infrared region. Transitions involving vibrational and rotational levels yield the vibrational and rotational-vibrational spectrum, which can be observed in the near infrared region. Finally, transitions involving electronic and vibrational energy levels give rise to the electronic and vibrational-electronic absorption, which can be observed in the visible and ultraviolet region. In transitions such as these, the rotational energy transitions can be

neglected. It is these absorption transitions that can give rise to the fluorescence transitions that will be discussed later (§2.2).

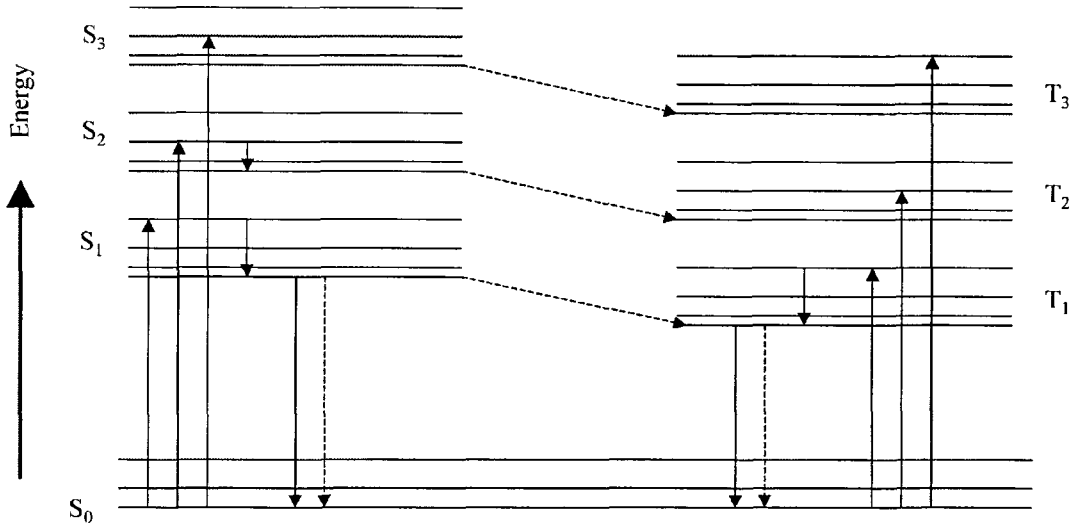

Figure 2.1

Jabłoński diagram indicating electronic and vibrational energy levels and transitions. Solid arrow lines indicate radiative processes and dashed arrow lines indicate non-radiative processes.

At room temperature, the majority of de-excited systems will occupy the lowest vibrational energy level of the ground electronic state S_0. The $S_0 - S_1$, S_2 or S_3 absorption transitions are spin allowed and correspond to the main electronic absorption spectrum observed. These transitions take place in time scales of the order of 10^{-15} s. The relationship between incident and transmitted light from a sample can be simply described. If a monochromatic beam of light of intensity $I_0(\nu)$ is incident on a sample of concentration c (mol l^{-1}) in a cell of path length l (cm), the intensity of the emergent beam $I(\nu)$ can be written as

$$I(\nu)=I_0(\nu)e^{-\varepsilon cl} \tag{2.1}$$

where $\varepsilon(\nu)$ is defined as the extinction co-efficient with units 1 mol^{-1} cm^{-1} (or M^{-1} cm^{-1}). The $S_0 - T_1$ or T_2 absorption transitions are spin forbidden but can be observed using long light paths or intense light sources. S_1 to higher singlet state and T_1 to higher triplet state absorption transitions are commonly observed by flash photolysis.

The luminescence transitions can be categorised into two types: fluorescence and phosphorescence. The $S_1 - S_0$ luminescence transition is of duration $1 - 10^3$ ns and is the normal fluorescence emission (§2.2). Transitions from higher singlet states to the ground state S_0 have been observed but are not as common. The $T_1 - S_0$ luminescence transition is the normal phosphorescence emission and is of a duration longer than that of fluorescence ($1 - 10^4$ ms) because it is also a spin forbidden transition. Again, transitions from higher triplet states to the ground state S_0 are known, but they too are uncommon.

The $S_1 - S_0$ non-radiative internal conversion usually occurs very rapidly and competes with the normal fluorescence. The $S_1 - T_1$ transition constitutes the internal quenching of S_1 and also competes with the normal fluorescence. Similarly, the $T_1 - S_0$ non-radiative internal conversion is usually very rapid and competes with normal phosphorescence.

2.2 Fluorescence Spectroscopy Fundamentals

The luminescence transition $S_1 - S_0$ is the inverse of the $S_0 - S_1$ absorption and is the transition that gives rise to the fluorescence. The process is shown in detail in Figure 2.2. If the energy of the fundamental vibrational mode is E_v, then the total energy (E) of a state is given by

$$E=E_e+\left(m+\frac{1}{2}\right)E_v \qquad (2.2)$$

where m is the vibrational quantum number. During absorption, excitation usually takes place from the lowest vibrational level of S_0 ($m=0$) to a vibrational level of S_1. Transitions from vibrationally excited electronic ground states to S_1 are known as hot bands and are of lower energy than the lowest energy transition ($m=0 \rightarrow n=0$)[1].

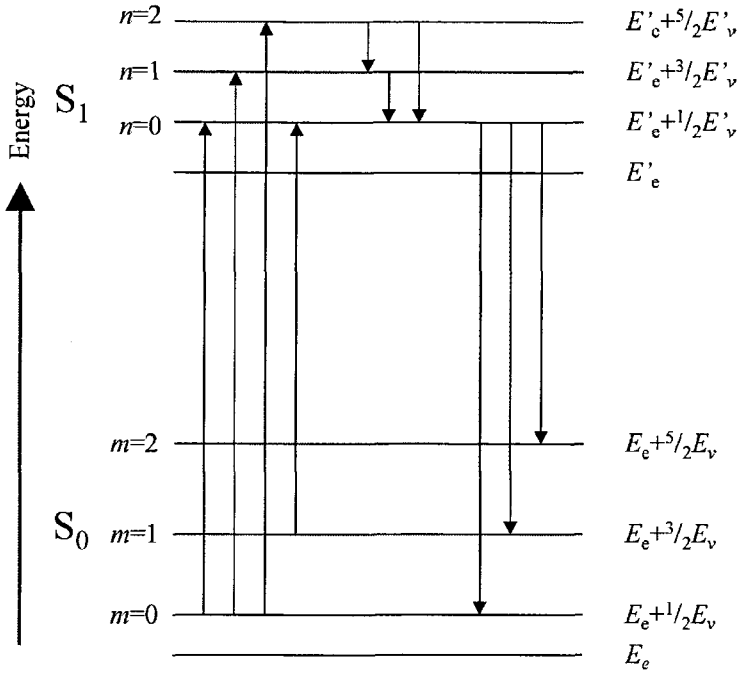

Figure 2.2:
Jabłoński diagram showing absorption and fluorescence transitions between vibrational levels of states S_0 and S_1. Here m and n are the vibrational quantum numbers in the states S_0 and S_1 respectively.

After excitation to a vibrational level of S_1 from S_0, a system can undergo an internal conversion whereby the system rapidly relaxes non-radiatively to the lowest vibrational energy level of S_1. Systems almost always relax back to S_0 from the lowest vibrational level of S_1. This internal conversion reveals that the energy of emission is typically less than that of the absorption energy and gives rise to the

"Stokes Shift" first observed in 1852 by Sir George Gabriel Stokes[8]. Consequently, we see fluorescence emission red shifted from that of the absorption spectrum. In the majority of absorption and emission cases, the Frank-Condon principle applies. This states that, because the time required for an electronic transition is negligible compared to that of nuclear motion, the most probable transition is one that has no change in the nuclear co-ordinates. The transition represents a vertical transition on a potential energy diagram, illustrated in Figure 2.3. As a result, if a particular transition probability factor is largest in absorption, the reciprocal transition is most probable in emission[9] (Figure 2.3). These absorption and emission spectra are mirror images of each other.

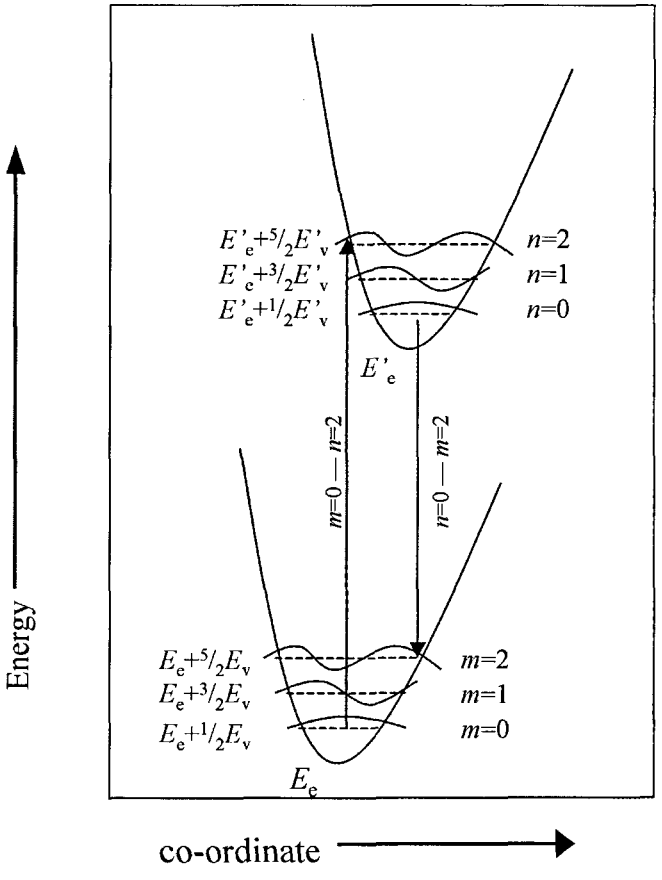

Figure 2.3:

Potential energy diagram plotting total energy as a function of configuration co-ordinate, illustrating Frank-Condon principle.

2.3 Fluorescence Parameters

2.3.1 Quantum Yield

Additionally, as discussed in §2.1 and illustrated in Figure 2.1, there are a number of non-radiative transition processes that can compete with the normal fluorescence after absorption. If the combined rate of the non-radiative processes is k_{NR} and the rate of fluorescence is k_F, we can define the fluorescence quantum yield ϕ as (using the Birks notation)[1]:

$$\phi = \frac{k_F}{k_F + k_{NR}} \tag{2.3}$$

The quantum yield is simply the ratio of emitted to absorbed photon rates.

The molecular fluorescence spectrum $F(\nu)$ can then be defined as the relative fluorescence quantum intensity at frequency ν, normalised by the relation:

$$\phi = \int_0^\infty F(\nu) d\nu \tag{2.4}$$

2.3.2. Fluorescence Lifetime

The fluorescence lifetime τ_M is defined as the average time a system spends in the excited state before returning to the ground state. Of course, the emission process is random and very few molecules in a system will emit photons at precisely $t=\tau_M$. Generally, fluorescence lifetimes are of the order of 10 ns.[9] Simply, the fluorescence

lifetime is the reciprocal of the sum of the radiative (i.e. fluorescence) and non-radiative rates.

$$\tau_{\mathrm{M}} = \frac{1}{k_{\mathrm{F}} + k_{\mathrm{NR}}} \tag{2.5}$$

The lifetime of the fluorophore in the absence of non-radiative processes (i.e. $k_{\mathrm{NR}} = 0$ & $\phi = 1$) is known as the natural or the intrinsic lifetime, τ_{n}, and is given by

$$\tau_{\mathrm{n}} = \frac{1}{k_{\mathrm{F}}} \tag{2.6}$$

The radiative rate and the intrinsic lifetime can be described in quantum mechanical terms by the Einstein A co-efficient[1]. The Einstein A co-efficient determines the probability of luminescence and its relation to the fluorescence spectrum.

$$k_{\mathrm{F}} = 1/\tau_{\mathrm{n}} = \sum_{m} A_{u0 \rightarrow lm} \tag{2.7}$$

where the Einstein A co-efficient is summed over the complete fluorescence spectrum attributed to transitions from the zeroth vibrational level (n=0) of the upper singlet state (u) to different vibrational levels (m) of the lowest singlet, or ground, state (l).

The intrinsic lifetime can, therefore in principle, be calculated from the absorption spectrum $\varepsilon(\bar{\nu})$, and emission spectrum $F(\bar{\nu})$, of the fluorophore, plotted in wavenumbers $\bar{\nu}$ (cm^{-1}), using the Strickler-Berg equation[1].

$$1/\tau_n = 2.88\times10^{-9}\frac{n_F^3}{n_a}\frac{\int F(\bar{\nu})d\bar{\nu}}{\int F(\bar{\nu})d\bar{\nu}/\bar{\nu}^3}\int\frac{\varepsilon(\bar{\nu})d\bar{\nu}}{\bar{\nu}} \qquad (2.8)$$

where n_F and n_a are the mean refractive indices associated with the fluorescence and absorption spectra respectively. The integrals are calculated over the S_0 – S_1 absorption and emission spectra. The intrinsic lifetime can also be calculated from the measured lifetime τ_M and the quantum yield ϕ

$$\tau_n = \tau_M/\phi \qquad (2.9)$$

Here, equation 2.9 is derived from equations 2.4, 2.5 and 2.8. There are sometimes occasions where there can be discrepancies between the values of τ_n obtained from equations 2.7 and 2.9 for many reasons, such as fractions of fluorophores being located near quenching groups[9].

2.3.3. Excitation Conditions

Two types of excitation conditions are commonly considered in discussing fluorescence: photostationary and transient. Photostationary conditions correspond to steady state excitation with light of intensity I_0 to produce a concentration of excited state molecules [^{1}M*]. Under steady state conditions $d[^1M^*]/dt = 0$. The rate equation for [^{1}M*] is

$$\frac{d[^1M^*]}{dt} = I_0 - (k_F + k_{NR})[^1M^*] \qquad (2.10)$$

Transient conditions correspond to excitation at $t=0$ by a δ-function light flash, i.e. a light pulse of negligible duration, to produce an initial concentration of excited molecules $[^1M^*]_0$. The fluorescence response function $i(t)$ of any molecular system is defined as the fluorescence at time t following such a δ-function excitation[10]. The rate of depopulation of excited states (i.e. $t>0$) is

$$\frac{d[^1M^*]}{dt} = -(k_F + k_{NR})[^1M^*] \tag{2.11}$$

so that

$$\begin{aligned} i(t) &= k_F \frac{[^1M^*]}{[^1M]} \\ &= k_F e^{-(k_F+k_{NR})t} \\ &= k_F e^{-t/\tau_M} \end{aligned} \tag{2.12}$$

where τ_M is defined as the molecular fluorescence lifetime equal to the reciprocal of the sum of the fluorescence and non-radiative rates. This is known as a monoexponential model of the fluorescence response function. This is a suitable description for many dilute solutions of fluorophores with a single excited state in homogeneous media. It also provides the most suitable model with which to test the time-resolution of a fluorometer and the level of systematic errors[11]. However, many fluorophores do not fit this model and there are a number of more complex models used to describe their kinetics, each containing up to five exponential components. However, one must be cautious when using more than three components in the $i(t)$ function, as there is a danger of over-parameterisation without the decay components having any physical significance.

The determination of fluorescence lifetimes can be achieved using a number of methods, the most common being phase and modulation fluorometry and pulse fluorometry. Pulse fluorometry using the time-correlated single-photon counting (TCSPC) technique will be discussed later (§2.4).

2.3.4. Fluorescence Quenching

Fluorescence quenching refers to any processes which attenuate the fluorescence intensity of a sample. There are a number of molecular interactions that can give rise to quenching, namely excited state reactions, molecular re-arrangements, energy transfer[12] and collisional quenching. Collisional (or dynamic) quenching is the most commonly encountered and will be discussed in this work. Static quenching can be a complicating factor when analysing quenching data, although it can also be a valuable source of information regarding binding between the fluorophore and the quencher. Common quenchers are oxygen, halides, some transition metal ions and acrylamide.

Collisional quenching of fluorescence is described by the Stern-Volmer equation

$$I_0/I = 1 + k_Q \tau_M [Q] \tag{2.13}$$

where I_0 and I are the fluorescence intensities in the absence and presence of quencher respectively, k_Q is the bimolecular quenching constant, τ_M is the fluorescence lifetime of the fluorophore in the absence of quencher and [Q] is the concentration of quencher. The Stern-Volmer quenching constant K_{SV} is given by $k_Q \tau_M$.

Quenching data is usually represented on I_0/I versus [Q] plots because I_0/I is expected to be linearly dependent upon the quencher concentration [Q]. Deviations from the Stern-Volmer relation are often observed in applications due to further complicating factors such as static quenching. A simple method to eliminate static quenching is to use fluorescence lifetimes to construct a Stern-Volmer plot. The fluorescence lifetime τ_M, and therefore the lifetime in the absence of quencher, is given by equation 2.5. Equation 2.5 can be modified to give the fluorescence lifetime in the presence of quencher, τ as

$$\tau = (k_F + k_{NR} + k_Q[Q])^{-1} \tag{2.14}$$

This gives

$$\tau_M / \tau = 1 + k_Q \tau_M [Q] \tag{2.15}$$

Equations 2.13 and 2.15 illustrate the important characteristic of collisional quenching, i.e. an equivalent decrease in fluorescence intensity and fluorescence lifetime.

Although, as will be discussed in chapter 5, the quenching of tryptophan residues in proteins (as with many other systems) do not follow a simple Stern-Volmer relation and a modified relation is required.

2.3.5 Anisotropy

Fluorescence anisotropy decay is a relaxation method which monitors the time dependence of the transition of a specific fluorophore to a random orientation in space which occurs via Brownian rotational diffusion[13]. From the nature of the

change in anisotropy with time, information can be derived as to the rotational mobility (how readily the molecule can tumble in solution) of the fluorophore. If the fluorophore is part of a larger molecule, such as tryptophan residues in proteins, the rotational mobility may reflect the overall rotation of the molecule as well as the localised motion of the fluorophore[14].

The radiation emitted by a fluorophore may be polarised upon excitation using polarised light. Usually the radiation is observed at 90° to exciting beam. Figure 2.4 illustrates a schematic of the optical set up for both steady state and time-resolved conditions.

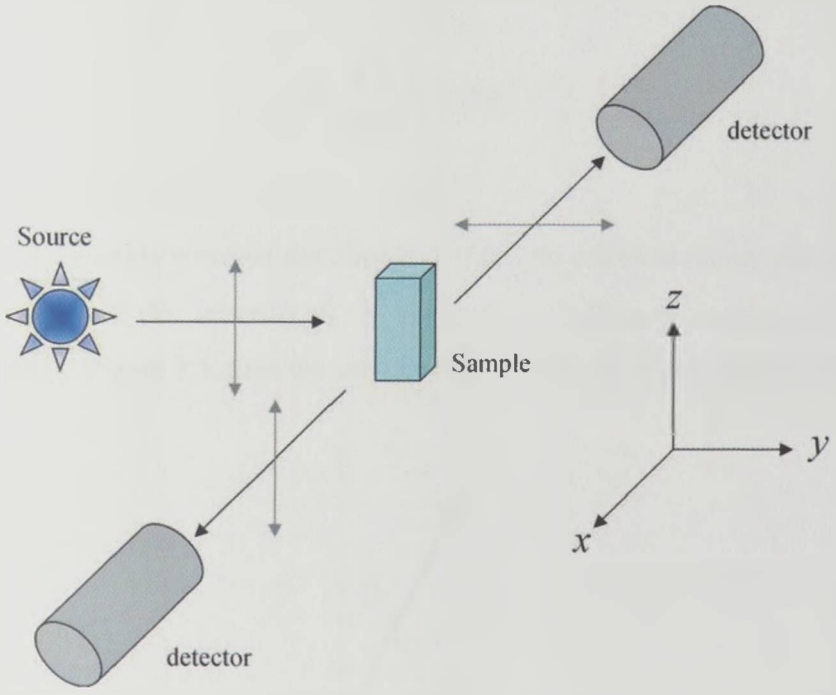

Figure 2.4:
Optical geometry for anisotropy measurements. Emission is collected with vertical and horizontal polarisations as shown. Either L-geometry or T-geometry (illustrated) can be adopted.

The components of the total fluorescence intensity along the three space axes are I_x, I_y and I_z. The sum of these components S is

$$S = I_x + I_y + I_z \tag{2.16}$$

As illustrated in Figure 2.4, it is usual for the excitation light to be polarised in the z-direction. Under these circumstances, symmetry dictates that $I_x = I_y$. This is a result of the transmission properties of polarisers, in particular, the dependence of the intensity on $\cos^2 \theta$, where θ is the angle between the transition moment transmitting direction of the polariser[9]. If the total intensity of a collection of fluorophores I_i, is observed through a polariser oriented through an axis p, the intensity is given as

$$I_p = \sum_{i=1}^{n} I_i \cos^2 \theta_{pi} \tag{2.17}$$

where θ_{pi} is the angle between the direction of the ith emission dipole and the axis of the polariser. If the intensity I_p is summed over three Cartesian co-ordinates represented by Figure 2.5, then the total intensity can be given by equation 2.18.

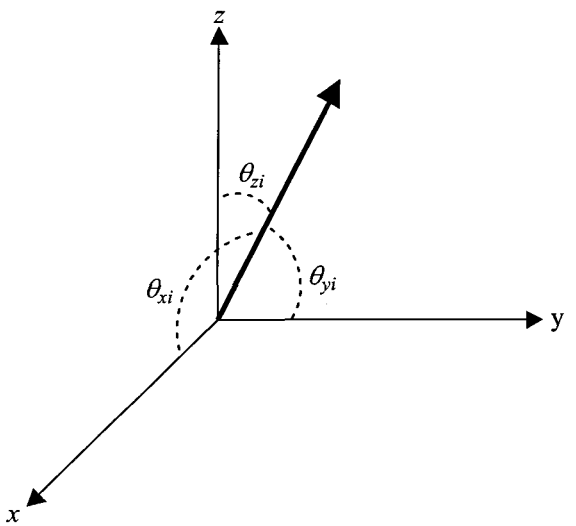

Figure 2.5

Fluorophore (bold arrow) at an arbitrary orientation in Cartesian co-ordinates.

$$I_x + I_y + I_z = \sum_{i=1}^{n} I_i \left(\cos^2 \theta_{xi} + \cos^2 \theta_{yi} + \cos^2 \theta_{zi} \right) \qquad (2.18)$$

Since the following equation is always correct

$$\cos^2 \theta_{xi} + \cos^2 \theta_{yi} + \cos^2 \theta_{zi} = 1 \qquad (2.19)$$

and symmetry dictates $I_x = I_y$ when using light polarised in the z-direction, this gives

$$S = I_z + 2I_y \qquad (2.20)$$

Now I_z can be defined as the parallel component $I_{\parallel}$ and I_y defined as the perpendicular component $I_{\perp}$. The fluorescence anisotropy, r, can be defined by

$$r = \frac{I_{\parallel} - I_{\perp}}{I_{\parallel} + 2I_{\perp}} = \frac{D}{S} \qquad (2.21)$$

where $D = I_{\parallel} - I_{\perp}$ and $S = I_{\parallel} + 2I_{\perp}$. The sum S contains information on the fluorescence only, whereas the difference D contains both fluorescence and rotational information.

In earlier literature, another measure of polarisation, the degree of polarisation (P), is used and is defined by

$$P = \frac{I_{\parallel} - I_{\perp}}{I_{\parallel} + I_{\perp}} \qquad (2.22)$$

where P and r are related by

$$P = \frac{3r}{2+r} \tag{2.23}$$

and

$$r = \frac{2P}{3-P} \tag{2.24}$$

Although the notation for polarisation is perfectly correct, the term anisotropy is preferred as it leads to simpler expressions.

In the time domain, equation 2.21 can be written simply as

$$r(t) = \frac{I_{\parallel}(t) - I_{\perp}(t)}{I_{\parallel}(t) + 2I_{\perp}(t)} = \frac{D(t)}{S(t)} \tag{2.25}$$

In time-resolved anisotropy experiments, the time dependent decays of the polarised emission components, $I_{\parallel}$ and $I_{\perp}$ are measured. These are given by

$$I_{\parallel}(t) = \frac{1}{3} I(t)[1 + 2r(t)] \tag{2.26}$$

and

$$I_{\perp}(t) = \frac{1}{3} I(t)[1 - 2r(t)] \tag{2.27}$$

Provided the rotational time, τ_r, is of the order of the fluorescence lifetime τ_M, $r(t)$ can be described in the simplest case in terms of a rigid spherically symmetric unbound rotor performing Brownian rotation in an isotropic medium by equation 2.28.

$$r(t) = r_0 e^{-t/\tau_r} \tag{2.28}$$

where r_0 is the initial anisotropy. The initial anisotropy is expressed in equation 2.29. If a fluorophore is immobilised in the above mentioned medium so that the Brownian rotation cannot occur, the anisotropy is independent of time and, for vertically polarised light, is given by

$$r_0 = \frac{1}{5}(3\cos^2 \vartheta - 1) \tag{2.29}$$

where ϑ is the angle between the absorption and emission dipoles. If we take ϑ equal to 90° and 0°, we obtain maximum values of –0.2 and 0.4 for r_0 respectively. Values of r_0 outside this range are usually due to instrumental effects or the inclusion of scattered light in the fluorescence signal.

Many molecules, however, will not be spherical and the rigid spherically symmetric rotor model will not be appropriate. In the case of these asymmetric molecules, the anisotropy can be described as a multiexponential decay

$$r(t) = r_0 \sum_j A_j \exp\left(-\frac{t}{\tau_r}\right) \tag{2.30}$$

where A_j are the associated fractional amplitudes in the decay.

For fluorophores bound to larger molecules (e.g. tryptophan residues in proteins) it is assumed that the fluorophore is embedded in an anisotropic medium. In this system the rotations are hindered and the fluorescence anisotropy will not decay to zero, but rather to a residual r_∞. A simple exponential decay law can be used to account for these effects.

$$r(t) = r_\infty + (r_0 - r_\infty)\mathrm{e}^{\left(-t/\tau_r\right)} \tag{2.31}$$

The rotational time in the fluorescence anisotropy is related to the molecular volume using the Stokes-Einstein theory. In the Stokes-Einstein theory the Brownian motion is dependent on the viscosity of the suspending fluid, the temperature and the size of the particles. The particle size (i.e. the hydrodynamic diameter) can be evaluated from a measurement of the particle motion, if viscosity and temperature are known (equation 2.32). Recently, it has been shown that particle growth in porous media can be monitored using fluorescence anisotropy[15].

$$\tau_r = \frac{1}{6D} = \frac{\eta V}{k_B T} \tag{2.32}$$

where D is the diffusional co-efficient, η is the viscosity of the microenvironment experienced by the fluorophore, V is the molecular volume, k_B is Boltzmann's constant and T is the absolute temperature.

2.3.6 Magic Angle

The magic angle is a precisely defined angle, θ_m, the value of which is approximately 54.7°. It is a root of a second-order Legendre polynomial

$$P_2(\cos\theta_m) = \frac{1}{2}(3\cos^2\theta_m - 1) = 0 \qquad (2.33)$$

Any interaction which depends on this second-order Legendre polynomial vanishes at the magic angle.

The use of "magic angle" conditions is important for intensity decay measurements. The total intensity I_T is not proportional to $I_{\parallel} + 2I_{\perp}$, rather it is proportional to some combination of $I_{\parallel}$ and $I_{\perp}$. The magic angle conditions makes I_T proportional to $I_{\parallel} + 2I_{\perp}$ irrespective of the degree of polarisation of the sample as the polarisation is dependent on the second-order Legendre polynomial (equation 2.33). The conditions require the excitation polariser to be orientated to the vertical position and the emission polariser to be orientated to the magic angle, 54.7° from the vertical, thus resulting in $I_{\perp}$ being selected two-fold over $I_{\parallel}$. This occurs as $\cos^2 54.7° = 0.333$ and $\sin^2 54.7° = 0.667$. Thus, the intensity from vertical and horizontal polarised components are properly weighted. If they were not, incorrect decay times would be measured. However, if the anisotropy were zero, the correct decay times would be obtained regardless of polariser orientation.

2.4 Fluorescence Lifetimes using TCSPC

2.4.1 Overview of Instrumentation and Principles

Time-resolved measurements are widely used in fluorescence spectroscopy because the data can often contain more information than steady-state data. Two techniques of measuring time-resolved fluorescence are common today, the time-domain and frequency-domain methods. In the frequency-domain, or phase modulation, method the sample is excited with intensity modulated light (usually sine or square wave modulation is utilised). When a fluorescent sample is excited in this manner, the emission is forced to respond at the same modulation frequency. The lifetime of the sample gives rise to a phase difference between excitation and emission modulations. This in turn can be used to calculate the fluorescence decay time τ, whereas in the time-domain, or pulse-domain, the sample is excited with a very short pulse of light. This light pulse should ideally be much shorter than the lifetime of the sample. The time-dependent intensity is measured following the excitation pulse. Although from the slope of a log $I(t)$ versus t plot, the decay time τ can be calculated simply, but fitting to the whole curve $I(t)$ is preferred. Fluorescence measurements in the time domain possess a much greater information content about the rates and therefore the kinetics of intra and intermolecular processes[16]. This work is concerned with the use of the time-correlated single-photon counting time domain technique.

The first report in scientific literature of the TCSPC technique was by Bollinger and Thomas in 1961, where they reported the measurement of the scintillation response for various crystals using gamma, neutron and alpha excitation[17]. A schematic diagram of a conventional TCSPC instrument is shown in Figure 2.6. The single photon counting measurement relies on the concept that the probability distribution for emission of a single photon after an excitation event yields the actual intensity against time distribution of all the photons emitted as a result of the excitation. By

sampling the single photon emission following a large number of excitation flashes, the experiment constructs this probability distribution[18].

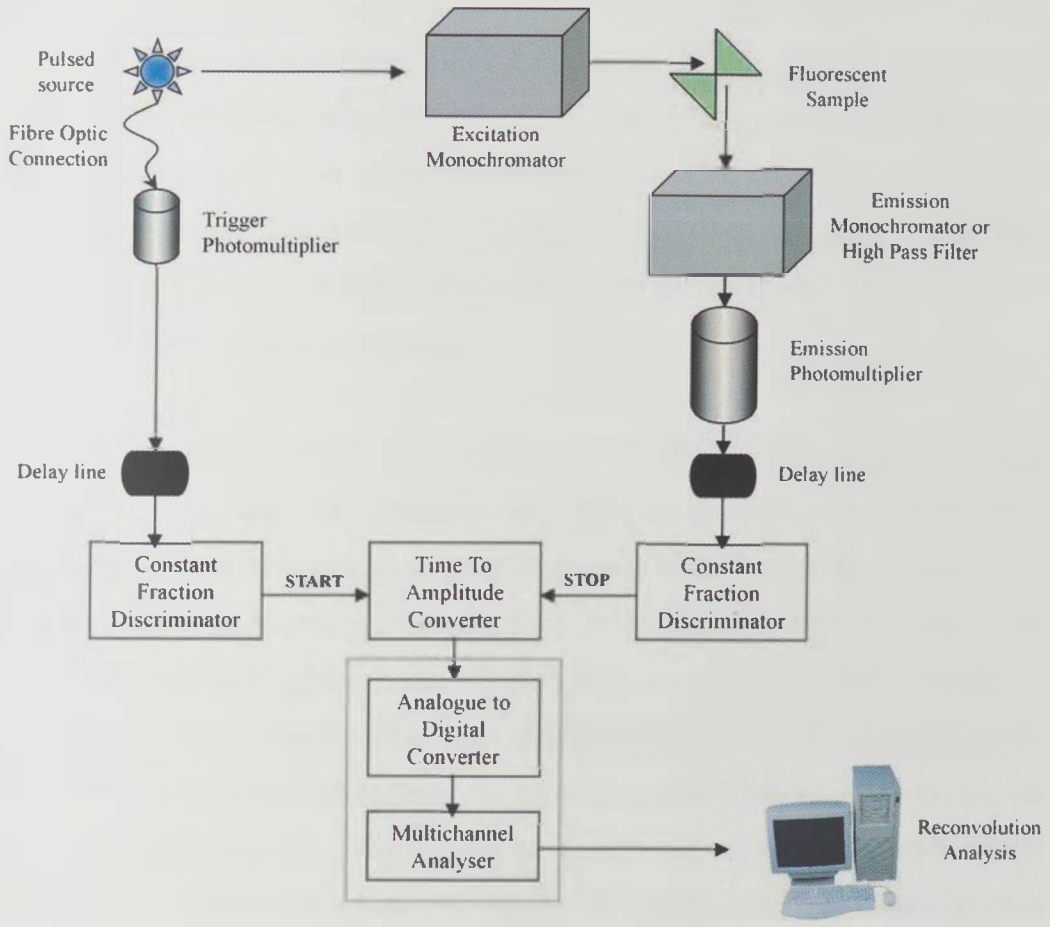

Figure 2.6:
Schematic diagram of a conventional single photon counting instrument

A pulsed source, such as a discharge lamp, radiation from a synchrotron, a mode locked laser or light emitting diode (LED), generate multiphoton excitation pulses which are absorbed by an assembly of sample molecules. The principle component in the timing set up is the time-to-amplitude-converter (TAC). The TAC can be considered to be analogous to a fast stopwatch. When an excitation pulse occurs, the trigger photomultiplier initiates a "start" pulse, which triggers the charging of a capacitor in the TAC. The voltage in the capacitor increases until either a preset time

is reached or a "stop" pulse is received, furnished by the emission photomultiplier. The time between "start" and "stop" pulses generates a proportional voltage across the capacitor. This is the time-to-pulse height (TPHC) conversion. This voltage is then digitised by the analogue to digital converter (ADC) inside the multichannel analyser (MCA) where it is allocated to an appropriate channel number. This process repeats until a histogram is collected which is equivalent to the actual fluorescence decay. Discriminators are utilised to minimise the registering of noise pulses and to ensure that the timing definition of "start" and "stop" pulses is independent of the signal pulse height.

The TAC operation is such as to only register a "stop" pulse detected after a "start" pulse. Therefore, the "stop" rate must be significantly low for the probability of detecting more than one photon per excitation pulse to be negligible. Consequently, the probability of detecting one photon also must be small; therefore, the "start" rate must be greater than the "stop" rate. If this condition is not met, the TAC will detect photons occurring at shorter times, thus affecting the fluorescence decay data such that the decay time will appear faster than it really is. This is photon pileup, and can lead to inefficiencies in the TCSPC technique, as the source may have to be reduced in intensity to ensure the absence of pileup. However, in dilute samples or weak sources, this is rarely an issue.

$$\alpha = \frac{S_p}{S_t} \leq 0.02 \tag{2.34}$$

Equation 2.34 defines the throughput of the apparatus a in terms of the rate of start pulses, S_t and the rate of photomultiplier anode pulses of fluorescence photons over all delay times S_p. Although a throughput of $\leq 2\%$ is widely considered as an acceptable value, experiments have been carried out with throughputs in excess of 30%. Therefore, the maximum count rate is not a theoretical limit, rather it is an

experimental limit governed by the deadtime of the electronics (i.e. time when no further inputs are recognised and conversions may be lost).

When operating at high source excitation repetition rates ($\gtrsim 10^5$ Hz, such as in mode-locked lasers or modern MHz pulsed LEDs), the ability of the TAC to reset between the occurrence of successive excitation pulses becomes a considerable issue. Distortions will be present in the fluorescence decay if the data is collected using the instrumental set up illustrated in Figure 2.6. A common method of addressing this issue is to operate the TAC in "reverse" mode. In this mode, trigger signals are routed to the "stop" input of the TAC and emission signals are routed to the "start" input. In addition, caution must be taken when measuring with sources of high conversion rates. These high repetition rates can lead to systematic changes in TAC calibration and a degradation of time resolution to varying levels, depending on the TAC manufacturer[19].

2.4.2 Decay Data Analysis

In §2.3.3, it was discussed that, under transient conditions, a molecule is excited at $t=0$ with a δ-function optical source. Although a true δ-function is not strictly possible with optical sources, it is a good assumption to make in many experimental cases when the excitation pulse full width half maximum, Δt_e, is much shorter than the fluorescence lifetime τ. Even if such fast pulsing sources are utilised, an effective δ-function is not measured, due to the timing jitter introduced by the detector, timing electronics or some optical components such as monochromators. If the timing jitter introduced by the ith component of the apparatus has a full width half maximum of Δt_i, the measured full width half maximum Δt_m is approximated by using addition in quadrature

$$\Delta t_m \approx \sqrt{\Delta t_e^2 + \sum_i \left(\Delta t_i^2\right)} \qquad (2.35)$$

For example, a typical modern detector device, such as the IBH TBX-04, has a maximum timing jitter of ~200 ps, so if an excitation pulse is measured at 640 ps, the actual optical pulse duration would be ~600 ps.

With these instrumental effects present, the measured fluorescence decay will deviate from the theoretical fluorescence response, $i(t)$, given in equation 2.12, since a δ-function is required for equation 2.12 to hold. The measured fluorescence can still be analysed, but it must be initially expressed as the convolution of the instrumental response $P(t)$, and the theoretical response function, thus

$$F(t) = \int_0^t P(t')i(t-t')dt' \tag{2.36}$$

where t' is defined as the variable time delays (i.e. channel numbers) of infinitesimally small time widths dt' (i.e. channel widths) of which $P(t)$ is composed.

Equation 2.36 is often expressed as

$$F(i) = P(i) \otimes {}^{1}\!/_{\tau} \exp\left(-{}^{i}\!/_{\tau}\right) \tag{2.37}$$

where the symbol ⊗ represents the operation of numerical convolution. Here the fluorescence decay is given in terms of the integer i representing the data channels. The convoluted form of the fluorescence decay can be obtained by assuming a functional form of the theoretical response. The convolution is applied to the theoretical model prior to comparison with the decay data. This is reconvolution analysis and is used in the analysis of decays in this work.

For fitting an assumed function, equation 2.37 can take the form

$$F_D(i) = A + B\big(F(i+\Delta)\big) \tag{2.38}$$

The integer i again denotes the data channels (from which τ can be obtained), A is a factor representing background noise, B is an amplitude scaling factor and Δ is the shift parameter included due to an inevitable mis-match in the positioning of the data channels of time $t=0$ and the position of the lamp profile. This is due to quantisation of the MCA, noise and wavelength effects[20].

Equation 2.38 must now be fitted to the actual fluorescence decay data $Y(i)$. In this work, the iterative least squares method is adopted. The "goodness of fit" between the convoluted form of the decay $F_D(t)$ and the actual fluorescence data $Y(i)$ is expressed using the quantity χ^2. The method will iteratively vary the values of A, B, τ and Δ to obtain the best fit, yielding the lowest value for χ^2.

By definition

$$\begin{aligned}\chi^2 &= \sum_{\text{DATA}} \left[\frac{\text{actual deviation}}{\text{expected deviation}}\right]^2 \\ &= \sum_{\text{DATA}} \left[\frac{Y(i)-F_D(i)}{\sigma(i)}\right]^2 \\ &= \sum_{\text{DATA}} [W(i)]^2\end{aligned} \tag{2.39}$$

where $\sigma(i)$ is the statistical uncertainty of the ith data point and $W(i)$ is the weighted residual. If the fitting function is appropriate, the weighted residual will be 1 for each data point and the value χ^2 would just be equal to the number of data points N.

It is not entirely correct for χ^2 to equal the number of data points since the expected deviation is a statistical expectation and is therefore a mean value, and the number of fitted parameters υ must be considered such that

$$\chi^2_{\mathrm{N}} = \frac{\chi^2}{(N-\upsilon)} \tag{2.40}$$

Here $(N-\upsilon)$ is the number of degrees of freedom, and should be used in place of N. It is usual to normalise χ^2, so that its value is independent of the number of degrees of freedom. This normalised value χ^2_{N} should be unity for a good fit, although a range of 0.9 to 1.2 is acceptable.

If the fluorescence decay determined experimentally and via convolution do not agree to acceptable statistical limits, the theoretical model may be inappropriate. In this event, an alternative model to describe the fluorescence is required. It is also possible that systematic errors can cause experimental and theoretical values to disagree. Typical systematic errors include scattered light, changes to the excitation pulse profile and fluorescence from filters. If systematic errors are present, they cannot necessarily be accounted for by using a more complicated model for the fluorescence decay.

Equation 2.25 can now be modified to accept the actual fluorescence data

$$Y_r(i) = \frac{G \times Y_{\parallel}(i) - Y_{\perp}(i)}{G \times Y_{\parallel}(i) + 2Y_{\perp}(i)} = \frac{Y_D(i)}{Y_S(i)} \tag{2.42}$$

with the integer i representing the channel number. As mentioned in §2.3.5, the sum function contains only fluorescence information, free from anisotropy information, and it can be analysed using the methods discussed in §2.4.3. However, since the difference function contains fluorescence and anisotropy parameters, it is considerably more complex to analyse. To obtain just the anisotropy parameters, the fluorescence parameters of the difference function $Y_D(i)$ are fixed, accepting the numbers from the decay analysis of the sum function $Y_S(i)$. If this constraint were not implemented, analysis of $Y_D(i)$ would be meaningless.

If $I_S(i)$, $I_D(i)$ and $I_r(i)$ are the impulse response functions for sum, difference and anisotropy respectively, equation 2.25 can be written as

$$I_S(i) \times I_r(i) = I_D(i) \tag{2.43}$$

In writing equation 2.25 in this form, both sides of the equation can be convoluted with the lamp pulse $P(i)$ to obtain two equivalent expressions for a fitting function for $Y_D(i)$. For fitting, $I_r(i)$ can take the form

$$I_r(t) = r_\infty + B_1 \exp\left(-\frac{i}{\tau_{r1}}\right) + B_2 \exp\left(-\frac{i}{\tau_{r2}}\right) \tag{2.44}$$

where B_1 and B_2 are the amplitude scaling factors, and

$$r_0 = r_\infty + B_1 + B_2 \tag{2.45}$$

Equations 2.44 and 2.45 allow two anisotropy decay times along with the initial (r_0) and residual (r_∞) anisotropies to be extracted from $Y_D(i)$. The χ^2 goodness of fit is given by

$$\chi^2 = \sum_i \left\{ \frac{Y_D(i) - [I_r(i) \times I_S(i) \otimes P(i)}{[Y_D(i)]^{1/2}} \right\}^2 \tag{2.46}$$

2.4.4 Light Source - Flashlamp

For pulsed fluorometry, there are four possible light source choices, namely: discharge flashlamps, synchrotron radiation, mode-locked lasers and light emitting diodes (LED). In this work, the intrinsic fluorescence of proteins requires the use of deep UV sources. Until mid-2004, the use of LEDs for intrinsic protein fluorescence was not an option as hitherto the lowest wavelength emission obtainable from pulsed LEDs was ~370 nm.[21] The use of UV LEDs in pulsed fluorometry will be discussed in Chapter 3. Previous to UV LEDs, the coaxial nanosecond flashlamp, although not modern technology, was the most popular choice due to its relative low cost and ease of use. The coaxial nanosecond flashlamp was also used extensively in the present work and the results will be discussed in Chapter 3.

Flashlamps can be either externally gated to give controlled breakdown, or can be free running in the mode of a relaxation oscillator. Cáceres, Goñi and Alvarez Rivas have demonstrated that externally gated flashlamps are more stable over extended periods of operation and can produce greater light intensity[22]. In general, gated flashlamps are capable of operation over a wider range of conditions. A diagram of the coaxial nanosecond flashlamp, developed by Birch and Imhof[23], is shown in Figure 2.7.

The coaxial flashlamp is of brass construction, which is fully demountable, with the hydrogen thyratron placed coaxially above the discharge chamber. Beneath the discharge chamber is the charging resistor box containing a high power low inductance charging resistor of approximately 3 MΩ connected to the anode of the lamp. The discharge chamber is isolated from the other compartments using Pyrex insulators and Viton o-rings. The electrodes are made from 2 mm tungsten rod with the anode pointed and the cathode flat. A 1 MΩ resistor across the spark gap improves gating control and a 270 kΩ resistor close to the anode reduces stray capacitance. One side of the chamber is fitted with a Swagelok coupling for connection to a gas system and the other side has a window for visual inspection of the spark via fibre optic cable. The optical system consists of an *f*/1 computer optimised focused silica lens which can be adjusted.

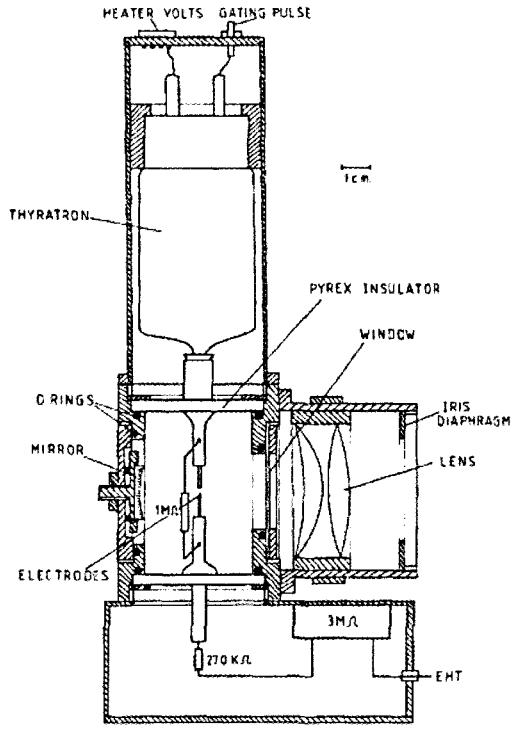

Figure 2.7

Diagram of Birch & Imhof coaxial nanosecond flashlamp. Reproduced with permission.

The hydrogen thyratron is key to the successful operation of the gated flashlamp. It is essentially a high-voltage, high-power, fast-acting, jitter-free switch with a short recovery time[24]. It has been observed that thyratrons cannot generate electric power, but they are ideally adapted to the task of converting it from one form to another without motion, noise or wear[25]. In flashlamp operation, the EHT supply will charge the cathode to the set voltage, while at the same time the current leaks through the 1 MΩ resistor across the spark gap until the anode is at the same voltage. When the switching voltage (~200 V) is applied to the thyratron, the anode is rapidly grounded to produce a potential across the gap. The potential will preferentially discharge across the gap, thus producing a spark.

2.5 Proteins

The great importance of proteins is implied in their name which comes from the Greek word "*proteios*" meaning "first place". Proteins account for more than 50% of the dry weight of most cells. They are instrumental in almost every aspect of an organism's function[26]. Proteins observed in nature have evolved through selective pressure to perform specific functions. Proteins are used for structural support, storage, transport, co-ordination of activities, response, movement, defence and enzymatic function. The functional properties of proteins depend upon their three-dimensional structures. The three-dimensional structures arise from the folding of particular sequences of amino acid chains, to generate, from linear chains, compact domains with specific three dimensional structures[27]. The folded domains can serve as modules for building up large assemblies such as virus particles, or to provide the functions described.

2.5.1 Amino Acids

Amino acids are organic molecules, all possessing a common central carbon atom (C_α), to which there is attached a hydrogen atom, an amino group ($-NH_2$) and a carboxyl group (-COOH) as shown in Figure 2.8.

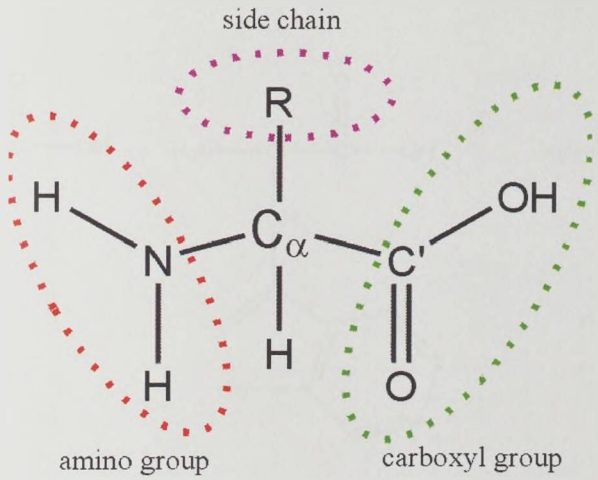

Figure 2.8

Common amino acid structure. The different side chains, represented as R, determines one amino acid from another

The variable R group attached to the fourth valence of the central carbon atom can be as simple as a hydrogen atom, for glycine (gly), or it may be a large carbon skeleton with various additional functional groups attached, as is the case for glutamine (glu). The chemical and physical properties of the variable functional group will determine the unique characteristics of a particular amino acid. Of the 20 amino acids, only three are intrinsically fluorescent. These are phenylalanine (phe), tryptophan (trp) and tyrosine (tyr) as shown in Figure 2.9. Tryptophan is the most common intrinsic probe for protein fluorescence, and indeed the one principally used in this work, and will be discussed later.

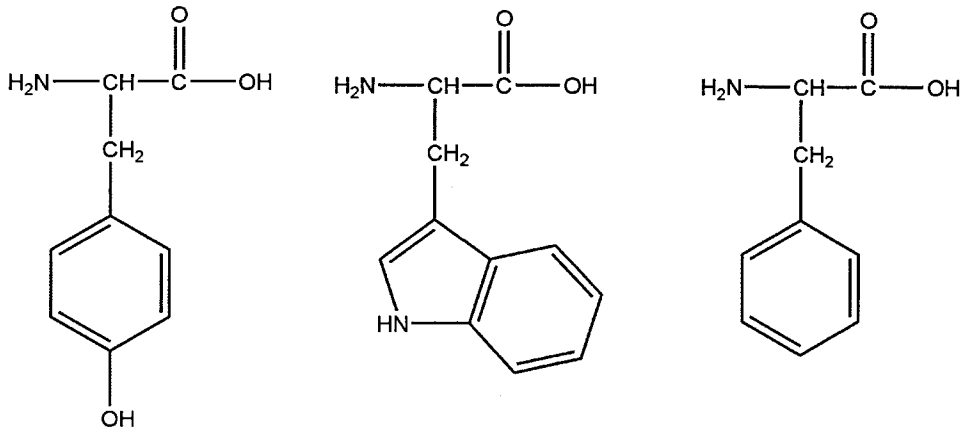

Figure 2.9.

The intrinsically fluorescent amino acids, tyrosine (tyr), tryptophan (trp) and phenylalanine (phe). All contain aromatic ring systems.

Amino acids are joined together in protein synthesis by means of a condensation reaction. The resultant covalent bond is called a peptide bond. The process can repeat to form an elongated or polypeptide chain. At the one end of the polypeptide chain will be an intact amino group and at the other end, an intact carboxyl group. The chain is said to extend from its amino (or N) terminus to its carboxy (or C) terminus. The formation of this polypeptide chain generates the "main chain" or "backbone" to which are attached the different appendages, i.e. the side chains of the amino acids.

The four groups attached to the central carbon atom (C_α) are chemically different for all amino acids, except glycine, which has two indistinguishable hydrogen atoms attached to C_α. Other than glycine, all amino acids are therefore chiral, from the

Greek word for hand, (i.e. not super imposable on its mirror image) and thus can exist in two different forms: L- or D-forms, as illustrated in Figure 2.10. The mechanisms for protein synthesis have evolved to use only the L-forms of amino acids, however there is no obvious reason for why this is the case.

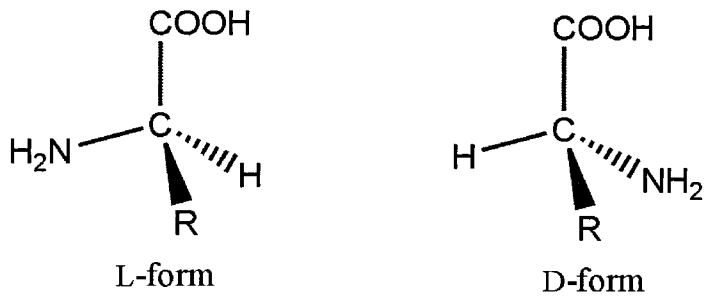

Figure 2.10

L- and D-forms of amino acids[28] (except glycine).

2.5.2 Protein Structure and Function

The polypeptide chain is not quite synonymous with the protein. A fully functioning protein is not just a polypeptide chain, rather it is one or more than one polypeptides precisely twisted, folded and coiled into a molecule of unique shape. The only degrees of freedom possessed by a polypeptide chain are the rotations around the C_α-N and C_α-C' bonds. These angles are denoted ϕ and ψ respectively. The polypeptide contains the information on the amino acid sequence, and it is this information that determines the three-dimensional shape the protein will have, given by ϕ and ψ. The polypeptide chain is formed by a polycondensation reaction of amino acids (Figure 2.11).

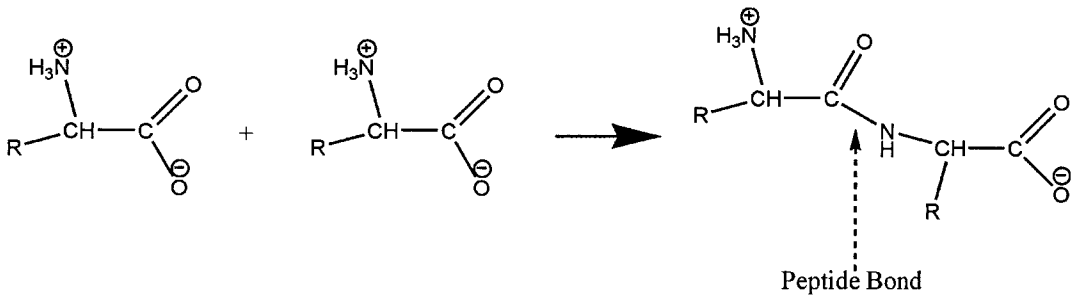

Figure 2.11

Condensation reaction between two L-amino acids to form a peptide bond.

Proteins can be globular or fibrous in shape, and within these broad categories countless variations are possible. It is possible to track a protein through its intermediate stages of folding. This can be achieved by characterisation of all states of the folding pathway. Characterisation of these states is not trivial and requires techniques such as NMR, hydrogen exchange, spectroscopy and thermochemistry. Despite the difficulty of the task, techniques for testing simulations by experiment and characterising a protein folding intermediate have been reported[29,30]. In addition, the discovery of proteins that assist in the folding of other proteins, called "chaperone proteins", is another promising step towards the understanding of protein folding[26]. However, despite considerable efforts in research, extensively reviewed by Finkelstein & Galzitskaya[31] and by Tramontano[32], it is still not possible to predict or deduce the three-dimensional structure a protein will take from its amino acid sequence and this is still one of the most fundamental and intellectual challenges in molecular biology.

There are four levels of protein structure: primary, secondary, tertiary and quaternary. The **primary structure** of a protein is its unique sequence of amino acids in polypeptide bonds. The primary structure is analogous to a very long word with the amino acids making up the letters of the word. If left to chance there would

be N^n possible different ways of arranging N amino acids in a polypeptide of n amino acids long analogous to the creation of nonsense words. The precise primary structure of a protein is not determined by a random linking of the amino acids, but by inherited genetic information. A slight change in the primary structure sequence can affect the ability of a protein to function.

Most proteins possess segments of their polypeptide chain that are repeatedly coiled or folded in patterns that contribute to the overall conformation of a protein. These coils and folds are collectively referred to as the **secondary structure**. They are the result of hydrogen bonding at regular intervals along the polypeptide backbone and can support a particular shape for that part of the protein. There are two particular shapes structured by the backbone: a helix, known as the α-helix, and a pleated sheet, known as the β-sheet. The α-helix, described in 1951 by Linus Pauling and Robert Corey[33-41], is a delicate coil held together by hydrogen bonds between every fourth peptide bond. The β-sheet is a structure in which the polypeptide chain folds back and forth, or where two regions of the chain are parallel to each other and where hydrogen bonds hold the structure together. Proteins can be constructed of any ratio of both structures or indeed almost entirely of one or the other.

The **tertiary structure** of a protein is superimposed on the patterns of the secondary structure, and consists of irregular contortions from bonding between the side chains of various amino acids (not hydrogen bonding as in secondary structure). The hydrophobic interaction is one factor that contributes to the tertiary structure. As a polypeptide chain folds into its functional conformation, amino acids with hydrophobic functional groups will usually congregate at the centre of the protein, out of contact with water. Their mutual exclusion of water is what keeps the hydrophobic side chains together in clusters. The hydrophobic interaction is actually caused by the behaviour of water molecules which exclude non-polar substances as the water molecules hydrogen bond to other water molecules and to hydrophilic molecules. In addition, further hydrogen bonding between side chains of certain

amino acids, and ionic bonding between positively and negatively charged side chains help to stabilise the tertiary structure. The conformation can be further strengthened by the strong covalent disulphide bridges, formed from the reaction between the –SH groups of two cysteine monomers.

Some proteins can consist of two or more polypeptide chains aggregated to form one functional macromolecule. The **quaternary structure** is the overall protein structure that results from this aggregation of polypeptide subunits. It is the overall product, the macromolecule with its unique shape, that works in a cell and its specific function arises from its architecture.

Protein conformation is also heavily dependent on the physical and chemical conditions of its environment. If conditions such as pH, salt concentration, temperature or solvent are altered, a protein may unravel and loose its native conformation and may become biologically inactive. Most proteins have a pH, salt concentration and temperature range that they will continue to function in. However, most proteins become denatured if they are exposed to an organic solvent, such as ethers, chlorinated hydrocarbons or alcohols. The protein can turn itself inside out as its hydrophobic regions change place with hydrophilic portions. When a protein is denatured, it may re-form its functional shape when it is returned to its native environment.

2.5.3. Fluorescence from Tryptophan

Along with nuclear magnetic resonance (NMR), electron paramagnetic resonance (EPR), infrared spectroscopy (IR), circular dichroism (CD), etc, protein intrinsic fluorescence and its associated observation of fluorescence anisotropy, collisional quenching and energy transfer are key tools available to the protein researcher[42]. Fluorescence has many advantages in that the usual nanosecond time window of

fluorescence is shorter than that of NMR or EPR and it is a technique sensing local environment, which distinguishes it from generalised techniques such as CD or IR[43].

As discussed in §2.5.1, tryptophan is the most widely used of the three fluorescent residues in the study of intrinsic protein fluorescence. This is due to tryptophan's high quantum yield and its sensitivity to its local environment. It is also a relatively infrequent residue in proteins, with a relative occurrence of around 1.1%.[44] Besides its nutritional value, L-tryptophan influences several physiological processes, such as brain function, hypertension, and behaviour[45]. The photophysics of even isolated tryptophan, however, are not trivial and a great deal of research papers have been published on models in an attempt to describe it.

The simplest model for tryptophan is its derivative indole (Figure 2.12).

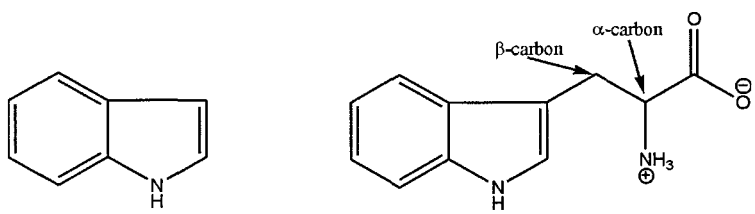

indole tryptophan

Figure 2.12
Tryptophan and its derivative indole (at pH 7). The indole system is connected to the α-carbon via the β-carbon.

Indole exhibits principle absorption peaks at 225 nm and 270 nm, whereas in tryptophan, the electron withdrawing properties of the carboxyl group give rise to absorption maxima at 280 nm (ε_{280} =5,600 M^{-1}) and at 218 nm (ε_{218} =33,000 M^{-1}). The longer wavelength band has weak vibrational structure: a shoulder at 271 nm, the main maximum at 279.5 nm, and a sharp peak at 288 nm. Absorption bands are caused by electron-vibrational transitions between π bonding orbitals and π^*

antibonding orbitals in the aromatic π-system of the indole ring[46]. In tryptophan containing proteins, the absorption at 295 nm is due to the tryptophan residues. The absorption of these species above 260 nm is a superposition of bands due to the electronic transitions $^1L_a \leftarrow {}^1A$ with $\lambda_{max} \approx 270$ nm and $^1L_b \leftarrow {}^1A$ with $\lambda_{max} \approx 280$ nm and 290 nm. The band at ~220 nm is the $^1B_a \leftarrow {}^1A$ transition. The $^1L_a \leftarrow {}^1A$ transition is the most susceptible to solvent, exhibiting a marked Stokes shift in moving from non-polar to polar solvents. The $^1L_b \leftarrow {}^1A$ is barely affected. These shifts are attributed to an increase in the dipole moment upon ^1L_a state excitation.

Early work indicated that the fluorescence decay of tryptophan was single exponential with a decay time of ~3 ns. However, De Lauder and Wahl studied tryptophan over a pH range of 2 to 10.6, and concluded there were three decay times, assigning them simply to cationic, zwitterionic and anionic forms[47]. In a review by Creed, it was suggested that a single decay time for each ionic species of tryptophan was inadequate to account for newer observed results, such as a bi-exponential decay for pHs where the zwitterionic form predominates[48].

Rayner and Szabo suggested the excitation of tryptophan to its manifold of excited singlet states results in rapid partitioning between coupled ^1L_a and ^1L_b states, initially having a solvent environment similar to that of the ground state[49]. The population distribution of the two states is dependent on the initial distribution prior to solvent re-orientation after which the two states are no longer interconvertible. Rayner and Szabo attributed this to the double exponential decay parameters of tryptophan of 0.5 ns and 3.1 ns. In a subsequent publication, Szabo and Rayner introduced the concept of the tryptophan conformer model[50] which, or at least a variant of it, is still the most accepted model for tryptophan photophysics. The rotamer model is shown as Newman projections (Figure 2.13).

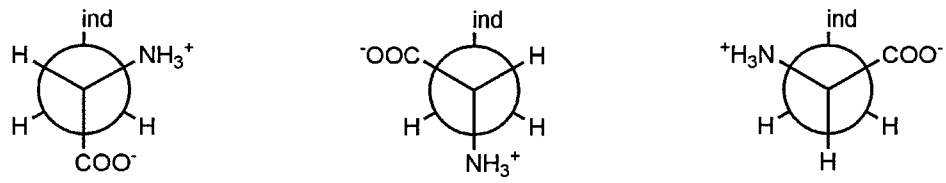

A B C

Figure 2.13.

Newman projections of the three tryptophan conformers introduced by Szabo & Rayner. The projection and rotation is along the C_α-C_β bond and shows the tryptophan zwitterion at pH 7. The label "ind" represents the indole ring system.

In the rotamer model, it was proposed that the different conformers allowed different degrees of charge transfer from the excited indole ring system to the electron withdrawing positively charged amine group and carboxyl group. The model was later modified to state that the 0.5 ns component is a result of conformers A and C since, in the zwitterion form, charge transfer to the positively charged amine group closest to the indole system[51,52]. This can be confirmed at higher pHs, where the amine group is deprotonated, thus removing its positive charge. Under these conditions the short decay component can no longer be observed. Now the tryptophan zwitterion is accepted to possess three decay components, with the longest component of ~6 ns attributable to rotamer B where charge transfer from the aromatic indole system to the positively charged amine group is longest.

Despite the three-exponential decay model of tryptophan, it was assumed that a tryptophanyl residue in proteins would be monoexponential for a given protein conformation. The justification for this was the assumed monoexponential decay of the analogue N-acetyl-L-tryptophanamide (NATA) due to the two peptide bonds on

either side of the α-carbon, initially making it widely regarded as a good model for tryptophan residues in proteins. However, intrinsic tryptophan fluorescence from proteins is rarely monoexponential and NATA has been shown to exhibit a bi-exponential decay[53].

There are however, a number of models used to represent the fluorescence from tryptophan in proteins. An alternative concept to the modified conformer model is given by Bajzer and Prendergast. They have invoked a multiexponential model where decays can be analysed by 2^N exponentials. It assumes that there are interactions between the indole moiety and the protein matrix and/or solvent, which are unique to each conformational state, and which therefore cause a specific lifetime[54]. However, this approach has been challenged and recent simulations have provided further evidence in support of the tryptophan conformer model, suggesting that the multiexponential fluorescence decays are caused by multiple non-radiative processes[55]. The results from fluorescence decay data must be substantiated with other techniques, such as NMR[56] or quenching[57] before absolute conformations can be deduced. However, for monitoring variations in structure[3] and for probing interactions with proteins[58] the fluorescence of tryptophan is a powerful tool as demonstrated in this work. Indeed, Czabotar, Martin and Hay have used the intrinsic tryptophan fluorescence of the influenza A virus to monitor structural changes[59].

3

New Pulsed Ultra-Violet Light-Emitting Diodes

3.1 Outline

The study of fluorescence in the time domain using light-emitting diodes (LED) is not a new phenomenon, and has been investigated thoroughly using many different fluorophores, LED drive circuitries and LED wavelengths[60-64]. There are also many commercially available pulsed LEDs over a wide range of wavelengths. However, the study of the intrinsic fluorescence from proteins using LEDs has hitherto been impossible due to LED technology permitting wavelength emissions no shorter than ~370 nm. The uses of deep-UV LEDs have applications far beyond time resolved fluorescence, such as bio-agent detection, water and air purification and food sterilisation. Consequently the research into group 3 nitride based high power deep UV LEDs is of international interest, and has been investigated by many research groups.

Reports of UV LEDs in the past 3 years or so have been numerous. In 2002, Yasan *et al* reported ultraviolet LEDs consisting of AlInGaN/AlInGaN multiple quantum wells with a peak emission wavelength of 280 nm,[65] and also a 280 nm UV LED using low-dislocation density hydride vapour phase epitaxy grown GaN as a substrate[66]. Adivarahan *et al* have reported sub-milliwatt LEDs with emission at 285 nm.[67] In addition, there have been steady reports of 280 – 290 nm LEDs of milliwatt outputs[68-70], also reporting on their characteristics under various temperature conditions[71]. During this time, LEDs have also been fabricated with wavelength emissions shorter than 280 nm. Yasan *et al* report the fabrication of a 4.5 mW LED at 267 nm,[72] Bilenko *et al* report the fabrication of a 265 nm with 10 mW pulsed operation[73] and Allerman *et al* report a 237 nm LED[74].

In the field of fluorescence spectroscopy, Peng *et al* report the use of a pulsed 340 nm LED and its application to the fluorescence decay parameters of nicotinamide adenine dinucleotide (NADH)[75], an important fluorescence indicator in cell metabolism. Also reported by the Photophysics Research Group at Strathclyde University, in collaboration with Glasgow-based Horiba Jobin Yvon IBH Ltd, is the first ever measurement of protein fluorescence decays using an LED[21]. In addition, the first pulsed LED for selective excitation of tryptophan fluorescence in proteins[76], and the excitation of aqueous phenylalanine using a 265 nm LED[77] are also reported by the Photophysics Research Group and will be discussed in this section.

The above-mentioned pulsed UV LED sources are of great importance, as they can excite important biomolecules, like NADH or proteins, conveniently, reliably and inexpensively. Previously, the study of the time-resolved fluorescence of such molecules required the use of bulky or expensive optical devices such as radiation from a synchrotron[14], mode-locked lasers[78] or flashlamps[23], the latter option being the most popular due to low cost and ease of operation. However, when compared to a LED, the flashlamp is much less convenient due to high maintenance, lower repetition rate and a greater susceptibility to radio frequency distortions. In biomolecular fluorescence research, the LEDs have the potential to replace the high cost or high maintenance sources mentioned above.

Light emitting diodes are fabricated from a direct band gap material. Electromagnetic radiation, or electroluminescence, is generated upon the recombination of electron hole pairs injected into the depletion region. Intrinsic semiconductors, such as silicon, have a similar band structure to insulators, but the band gap is not very large, usually in the range of 0.5 – 3.0 eV. This allows electrons to jump between conduction and valence bands on application of an electrical current (Figure 3.1)[79]. However, silicon has an indirect band gap, where the electron in the conduction band cannot rejoin the valence band by radiative recombination.

Electrons will return via less efficient means, hence these materials are unsuitable for LED or laser diode fabrication.

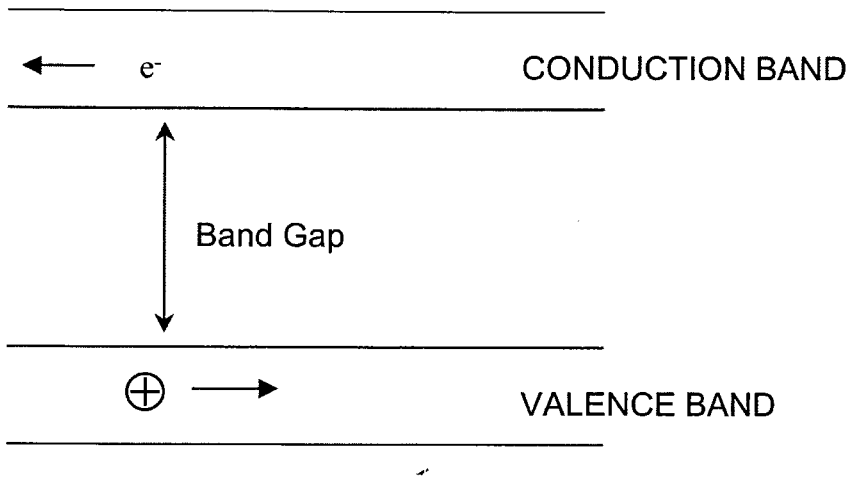

Figure 3.1
Schematic representation of direct semiconductor band gap

The electrical conductivity of a semiconductor can be increased by adding doping elements. For example, if a trace of an element with 5 outer electrons such as arsenic is added to a crystal of silicon with 4 outer electrons per atom, it provides an extra electron which is free to move throughout the material. This is called an *n*-type semiconductor where *n* stands for negative since the electrical carrier is a negatively charged electron. In the band description in Figure 3.1, these extra electrons occupy a discrete level about 0.1 eV below the bottom of the conduction band. These electrons cannot move directly as there are insufficient numbers to form a continuous band, but they have sufficient thermal energy to enter the conduction band where they are free to move.

Conversely, if a trace of an element with 3 outer electrons, such as gallium is added to a silicon crystal, it creates an electron shortage. This is known as a *p*-type semiconductor. Here *p* is for positive since the electrical carrier can be considered as a positively charged hole. Again, using band theory in Figure 3.1, a Ga-Si bond will

not form part of the valence band of the material. Instead it will occupy a discrete level or orbital just above the valence band. Again, this gap will be ~0.1 eV, so electrons from the valence band have sufficient thermal energy to be promoted to these levels. If the dopant level is low, these levels will not contribute to conduction, and the positive holes left behind in the valence band are free to move. When *p*-type and *n*-type regions are grown side by side, the result is a *p*-*n* junction, with electrons on one side and positive holes on the other. This allows current to flow in just one direction and is the basis of the diode.

The LED devices used in this work were based on aluminium gallium nitride (AlGaN) fabrication technology grown on AlN epilayers. The first type of junction laser diode produced was from the direct gap semiconductor gallium arsenide, followed by gallium arsenide phosphide and belong to the same class as AlGaN. The band gap of AlGaN alloy lies in the UV region between 200 and 363 nm.[80] The benefits of AlN epilayers over GaN epilayers are that they exhibit higher output powers and that they have better thermal stability. Using AlN epilayers as a template for nitride devices is also beneficial as they have excellent UV transparency down to 200 nm. These epilayers are grown on sapphires by metal-organic chemical vapour deposition (MOCVD)[81]. A typical UV LED structure is shown in Figure 3.2

Figure 3.2

Typical UV LED structure based on an AlN epilayer.

For deep-UV emission (λ <340 nm), the quantum well structure based LED requires an active layer with Al composition higher than 20%, although achieving *p*-AlGaN with high Al composition is a challenging issue. Kim *et al*[82] describe the construction of a 290 nm LED using the above technology. On the AlN epilayer, a 1.5 mm Si-doped *n*-$Al_{0.6}Ga_{0.4}N$ layer is grown as the *n*-type contact layer. On this contact layer is the active region consisting of an $Al_{0.4}Ga_{0.6}N$ (2.5 nm)/$Al_{0.5}Ga_{0.5}N$ (3.0 nm) multiple quantum well. A *p*-$Al_{0.7}Ga_{0.3}N$ layer of 10 nm is also employed as an electron-blocking layer to effectively inhibit electron overflow, since it is difficult to produce an AlGaN alloy with high Al composition. This layer enhances the electron-hole radiative combination in the quantum wells. The final layer of the LED is a 60 Å Mg-doped *p*-$Al_{0.6}Ga_{0.4}N$ and 150 nm heavily doped *p*-$Al_{0.1}Ga_{0.9}N$ as the *p* contact layer[82].

As will be discussed in chapter 5, these LEDs are a step towards eventual fabrication of "lab-on-a-chip" biosensors based on fluorescence lifetimes, due their compact nature (Figure 3.3).

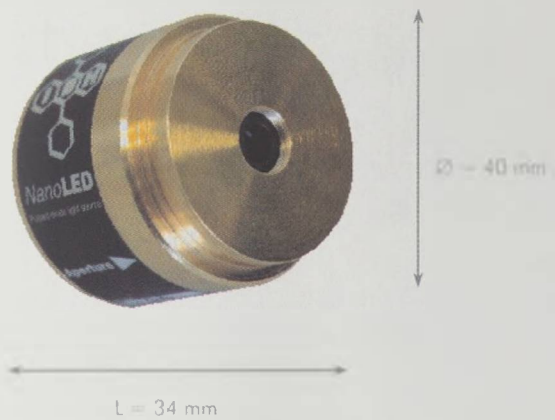

Figure 3.3
The IBH NanoLED pulsed LED device, showing length and diameter dimensions

The compact and portable excitation source has been the missing element in the goal to achieve "lab-on-a-chip" sensors based on intrinsic fluorescence lifetimes of proteins, since semiconductor detector devices have been available for a number of years in the form of avalanche photodiodes[83].

In all fluorescence lifetime experiments using the 265 nm, 280 nm and 295 nm LEDs, illustrated in the following sections, TCSPC measurements were conducted using the IBH 5000U Fluorescence Lifetime System (Horiba Jobin Yvon IBH Ltd, Glasgow) to record data and the IBH Decay Analysis Software Library for Microsoft Windows to analyse the decays. The LEDs were installed and configured in the IBH NanoLED drive circuitry, operating at 1 MHz, used to achieve LED pulsing and TCSPC synchronisation. The IBH 5000U is a compact fluorescence lifetime system similar to the schematic representation illustrated in Figure 2.6. The major differences between the 5000U and the schematic in Figure 2.6 are: the trigger photomultiplier and leading edge discriminator are replaced with the IBH NanoLED drive electronics, the constant fraction discriminator is incorporated into the IBH TBX-04 photon detection module, and the ADC and MCA are installed in the computer.

3.2. The 280 nm Light Emitting Diode

3.2.1. Characterisation of the Diode

The 280 nm LED (Zhang *et al*[84]) is characterised and compared with the IBH 5000F coaxial nanosecond hydrogen flashlamp. The 5000F flashlamp is the fourth generation of lamp originating from the Birch and Imhof design[23] illustrated in §2.4.4 with the discharge chamber filled with hydrogen to 0.5 bar, the electrode gap set at 1 mm and the EHT voltage set to ~8 kV for this work. The typical spectral profile of the device is shown in Figure 3.4. The extended spectral profile to 550 nm is shown in Figure 3.5. The profile was recorded with an IBH *f*/3 monochromator, incorporating a holographic grating in a Seya Namioka geometry, and a 2 nm bandpass.

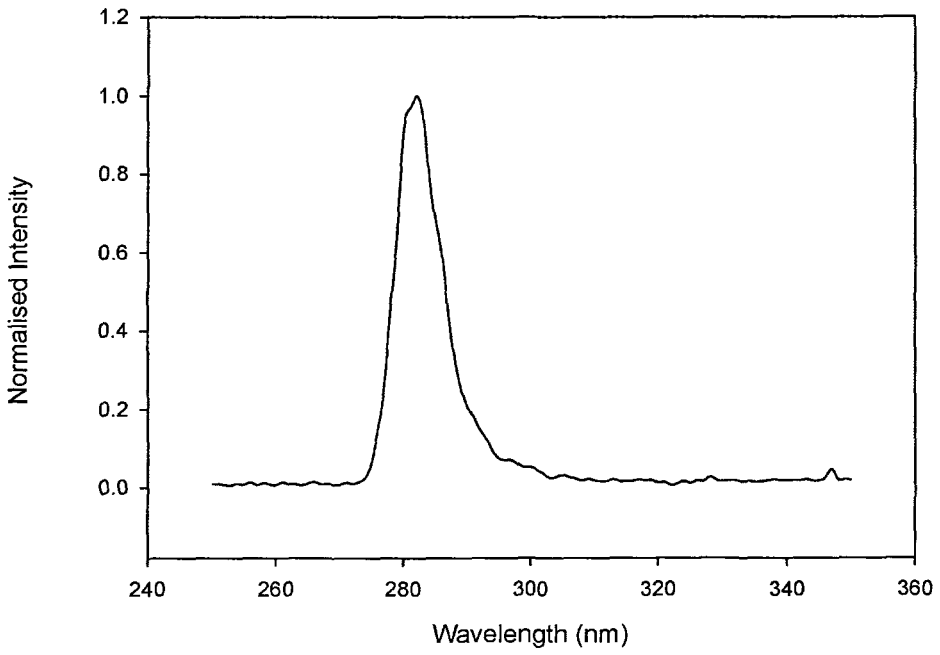

Figure 3.4
Spectral profile of 280 nm LED (actual peak 282 nm), with 2 nm bandpass.

Figure 3.4 shows the full-width half maximum of the spectral output to be ~10 nm. Extending the scan to 550 nm (Figure 3.5) highlights a long wavelength emission at ~430 nm. This emission peak cannot be used for exciting other fluorophores as it has a long decay time of ~500 μs. These long wavelength peaks arise from the carrier recombination from the conduction band to the deep acceptor levels in the *p*-AlGaN layers[85]. To ensure this unwanted longer wavelength emission is not detected along with the Stokes shifted fluorescence signal, it is necessary to use a monochromator to pre-filter the output from the LED, rather than exciting the sample directly. Similarly, although the use of high pass filters provides greater sensitivity, the long wavelength emission is further discriminated against by using a monochromator to select the fluorescence wavelength.

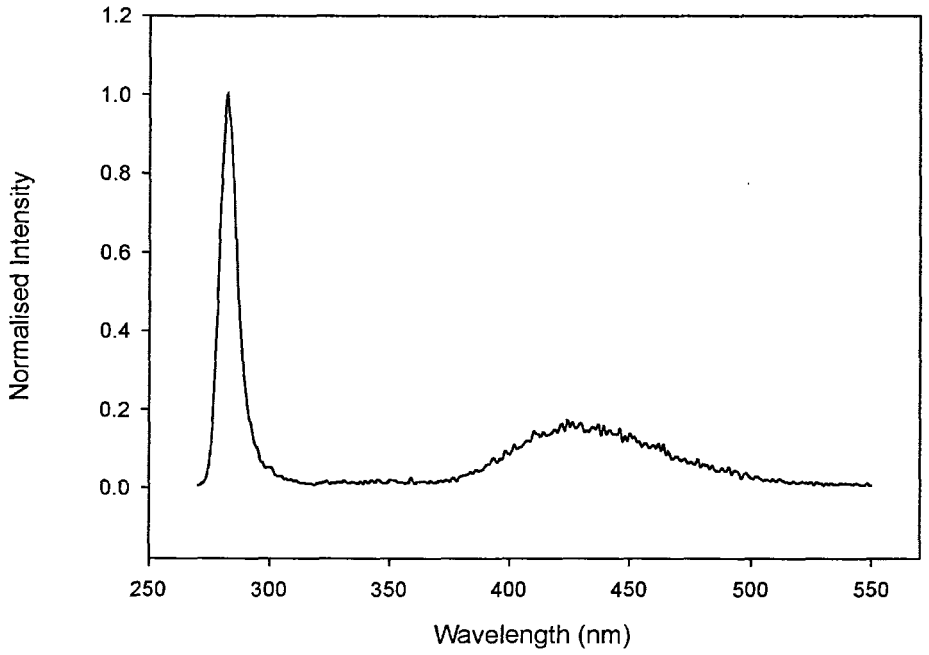

Figure 3.5

Extended spectral profile of 280 nm LED showing long wavelength emission peak at ~430 nm.

A typical instrumental pulse is illustrated in Figure 3.6. The pulse was measured with the IBH TBX-04 single photon detection module under TCSPC conditions.

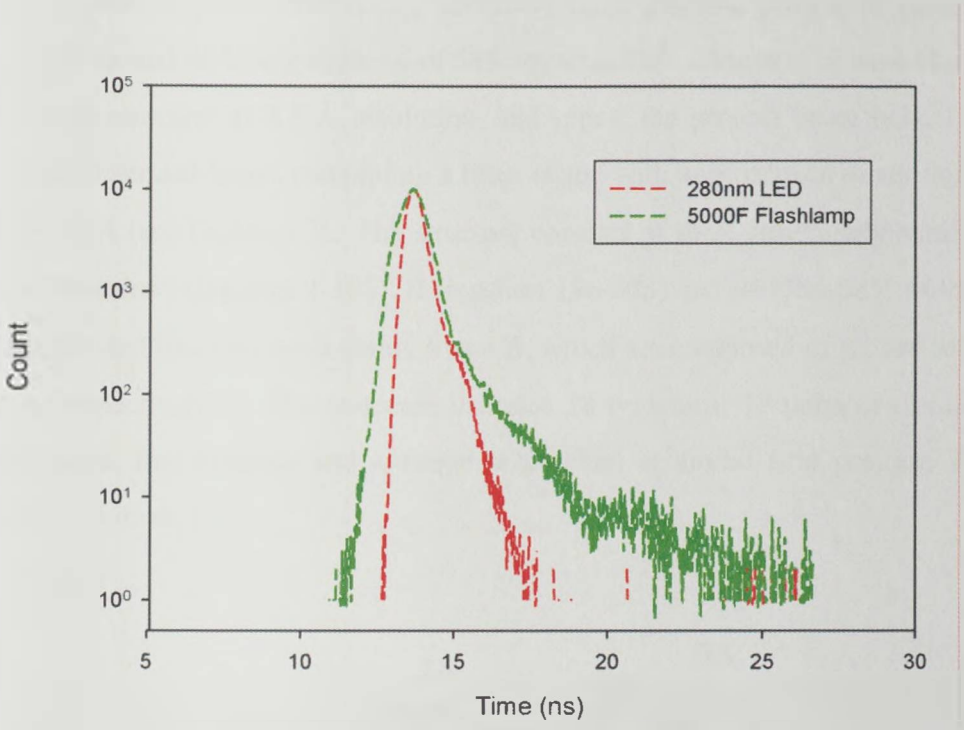

Figure 3.6.
Pulse width of 280 nm LED. Pulse width of IBH 5000F flashlamp included for comparison.

The measured full-width half maximum (FWHM) of the diode is 600 ps. If we assume the detector exhibits its stated nominal timing jitter of ~200 ps, using addition in quadrature, the optical pulse width is calculated as ~565 ps. This is considerably faster than previous pulsed LED sources and compares favourably with the coaxial nanosecond flashlamp with a FWHM of ~900 ps. The faster pulsing allows for better resolution of shorter lifetime components. The semi-logarithmic plot shows the LED to be free from afterglow and pre- or after-pulsing. The peak and average power of the LED were measured using a Hamamatsu S1277-1010BQ photodetector. A summary of output powers from all devices is displayed in Table 3.2.

3.2.2. Measurements on Human Serum Albumin

Human Serum Albumin (HSA) is a relatively large globular protein of molecular weight of around 66 kDa consisting of 585 amino acids[86]. Sugio *et al* have obtained the crystal structure at 2.5 Å resolution, and report the protein being helical with turns and extended loops, resembling a heart shape with approximate dimensions 80 × 80 × 30 Å (see Figure 3.7). The structure consists of three structurally similar α-helical domains I (residues 1-195), II (residues 196-383) and III (384-585) which are further divided into two subdomains A and B, which are composed of six and four α-helices respectively[87]. The molecule includes 18 tyrosines, 17 pairs of disulphide bridges, one free cysteine and a single tryptophan at amino acid position W214 located in domain IIA.

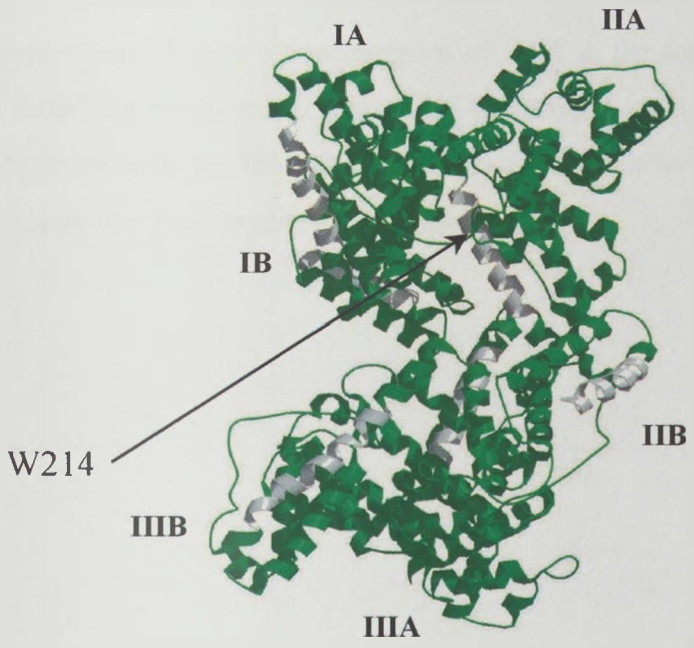

Figure 3.7

Schematic drawing of the Human Serum Albumin molecule showing position of W214 and subdomain areas. Structure from The Protein Data Bank[88].

HSA is the most abundant protein in blood plasma with a typical concentration of 640 μmol l^{-1} or 5 g/100 ml. It has a wide affinity for a number of metabolites such as Cu^{2+}, Zn^{2+} and also for amino acids and many hydrophobic ligands including fatty acids, bilirubin, thyroxine and hæmin. The most important physiological role of HSA is thought to be to bring such species in the bloodstream to their target organs, as well as maintain the pH and osmotic pressure of blood plasma.

Human Serum Albumin (HSA) (99%, Sigma-Aldrich, Dorset) was immobilised in an alcohol free and pH neutral hydrated silica sol-gel matrix synthesised from the precursor tetramethoxysilane. The encapsulation of HSA in sol-gel derived matrices, prepared by a variety of synthesis methods, has been previously investigated[89,90]. The preparation and properties of silica sol-gels and the encapsulation of proteins within them will be discussed in detail in Chapter 4. Initial concentrations and volumes were chosen to give a concentration of HSA in the sol gel of 2.5 mg/ml. Figure 3.8 shows the emission spectrum of HSA in sol-gel, excited with the 280 nm LED and recorded using the IBH 5000U. All measurements were carried out using 4×1×1 cm quartz type fluorometric cells (Optiglass Ltd.).

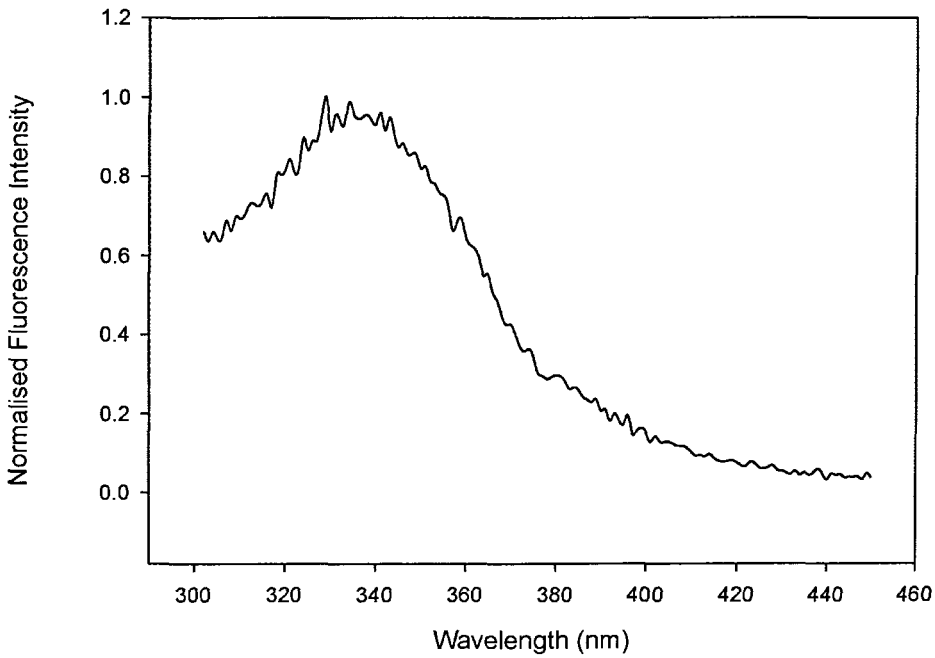

Figure 3.8

Sol-gel encapsulated HSA emission spectrum measured with the 280 nm LED and a bandpass of 6 nm.

The steady-state emission spectrum curve is less smooth than that of a spectrum measured with a continuous wave spectrometer. Since the spectrum was collected using TCSPC conditions, it is the fluorescence photon count from the sample that is measured from 300 – 450 nm in 1 nm increments rather than directly measuring the fluorescence intensity. Although a continuous wave spectrometer is preferred for steady-state fluorescence experiments, the pulsed 280 nm LED can provide a spectrum is identical to that measured with continuous wave spectrometers. In addition, the emission maximum from the single tryptophan residue in HSA is the same for HSA in solution as it is for HSA in sol-gel. It is known that some solvents such as methanol, and large changes from neutral pH can have a detrimental effect on biomolecules by altering their conformation[91]. The presence of harmful solvents and excessively high or low pH can be detected by a spectral shift in tryptophan

emission[92,93]. Since no change in tryptophan emission wavelength is seen, it can be concluded that the protein is significantly unaltered as the tryptophan environment is not detectably perturbed by the presence of the sol-gel confirming a solvent suitable and pH neutral environment.

The fluorescence decay of HSA in sol-gel was also measured and is shown in Figure 3.9 including the fitted function and weighted residuals. Decays were recorded on the IBH 5000U incorporating an excitation and emission monochromator with the latter tuned to 335 nm to select the tryptophan residue fluorescence signal.

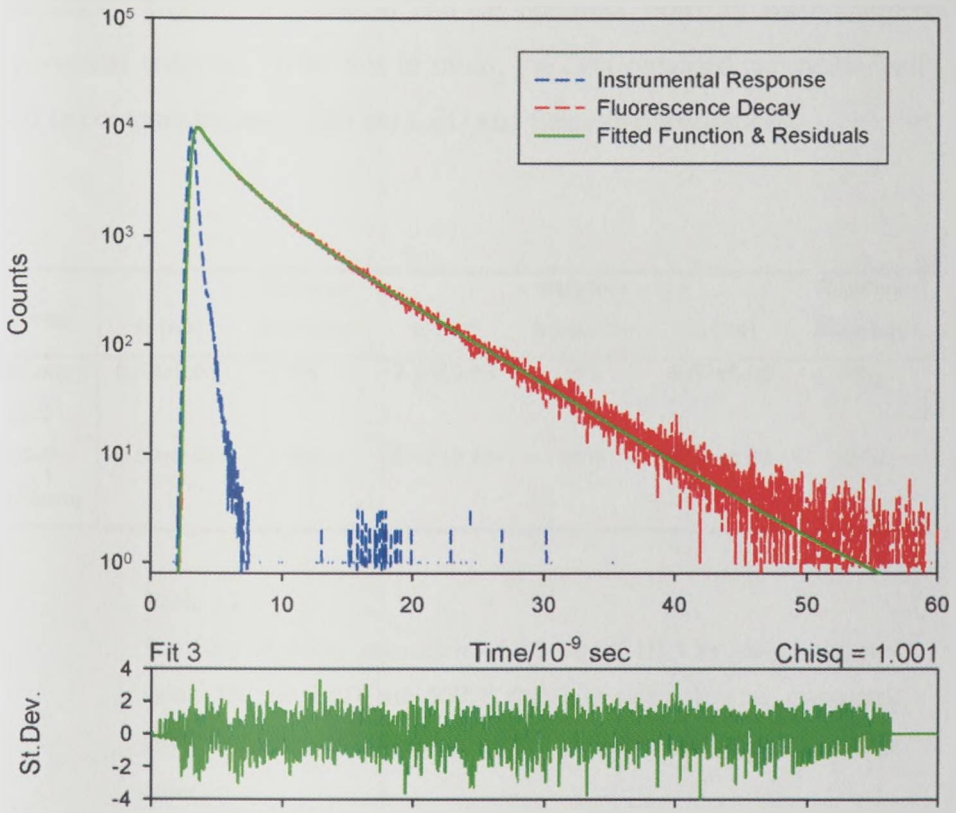

Figure 3.9

Fluorescence decay of 2.5 mg/ml HSA in sol-gel including instrumental pulse, fitted function and residuals

The semi-logarithmic scale again shows the LED pulse to be free of unwanted afterglow or after-pulsing. The fluorescence decay was fitted to a three-exponential model, and compared to the results obtained using the IBH 5000F nanosecond flashlamp with its monochromator tuned to 280 nm. These results are summarised in Table 3.1. The three-exponential function is consistent with the now widely accepted modified tryptophan conformer model[50-52], however, a three-exponential model may not be strictly correct. Excitation of HSA fluorescence at 280 nm is known to give rise to energy transfer from tyrosine to tryptophan, and ideally this effect should be included in the model for the fluorescence decay. Due to this extra complexity, limited information can be obtained from an over simplified three-exponential analysis. With this in mind, the data obtained can realistically only be used to compare between 280 nm LED and flashlamp excitation.

Source	τ_1 (ns)	Relative Intensity	τ_2 (ns)	Relative Intensity	τ_3 (ns)	Relative Intensity	χ^2
280 nm LED	0.53±0.05	8%	2.43±0.15	38%	6.07±0.05	54%	1.00
5000F flashlamp	0.59±0.06	9%	2.47±0.19	36%	6.04±0.05	55%	1.08

Table 3.1

Summary of decay parameters of 2.5 mg/ml HSA in sol-gel obtained using 280 nm LED and 5000F flashlamp, also showing component errors to 3 standard deviations, relative intensities and χ^2 goodness of fit criterion.

The results obtained from the 280 nm diode are in good agreement with the well-established hydrogen flashlamp, and confirm the suitability of the device as a suitable excitation source. The data is also consistent with work from another laboratory, using a mode-locked laser[94]. The χ^2 goodness of fit criterion of 1.00

shows the decay to be free from scattered excitation light or scattered fluorescence that might be expected from a porous material like silica sol-gel. This data bodes well for eventual fabrication of "lab-on-a-chip" biosensors based on protein immunoassays. In these preliminary experiments using this device, a factor of ~12× greater fluorescence count rate over the hydrogen flashlamp was obtained. Higher fluorescence count rates are obtainable and will be discussed in §3.3.

The suitability and accurateness of the 280 nm device has been demonstrated. However, although the protein HSA contains a single tryptophan residue that simplifies the kinetics, with 280 nm excitation, as well as direct tryptophan excitation, energy transfer from the 18 tyrosines to tryptophan also takes place thus complicating the analysis. The device is ideal for exciting tyrosine[95], but if tryptophan is to be preferentially excited, a device emitting at 295 nm is more suited. This will be discussed in the following section. As well as proteins, the device can be used for excitation of organic molecules such as naphthalene and stilbene (Figure 3.10).

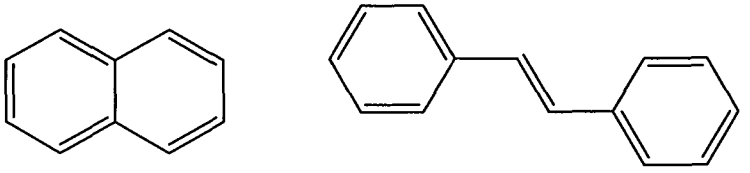

naphthalene stilbene

Figure 3.10 – Structures of Naphthalene and Stilbene

3.3 The 295 nm Light Emitting Diode

3.3.1 Characterisation of the Diode

In this section, the measurements using the 295 nm diode (Sensor Electronic Technology Inc.) are compared with a later, more intense, 280 nm device[68] and the IBH 5000F nanosecond flashlamp. A summary of the output powers of all devices used are shown in Table 3.2. The powers of the 280 nm device discussed in the previous section are included for comparison.

Source	Average Power	Peak Power
IBH 5000F Flashlamp	0.45 μW	12 mW
295 nm diode	0.35 μW	0.6 mW
Later 280 nm diode	0.7 μW	1.2 mW
Initial 280 nm diode	0.42 μW	0.7 mW

Table 3.2
Comparison of average power and peak power of all devices discussed in this chapter.

For the LEDs, the average power output was obtained by pulsing the LED using the IBH NanoLED drive circuitry (1 MHz repetition rate), and placing the LED close to the power meter. The output powers from the flashlamp, operating at a repetition rate of 40 kHz, are calculated by integrating over the wavelength range 200 – 1,000 nm over a solid angle of 4π.

Figure 3.11 shows an extended spectral profile to 520 nm of the 295 nm diode recorded using a SPEX FluoroMax2 at 2 nm spectral bandwidth. The spectral FWHM of the device is ~12 nm.

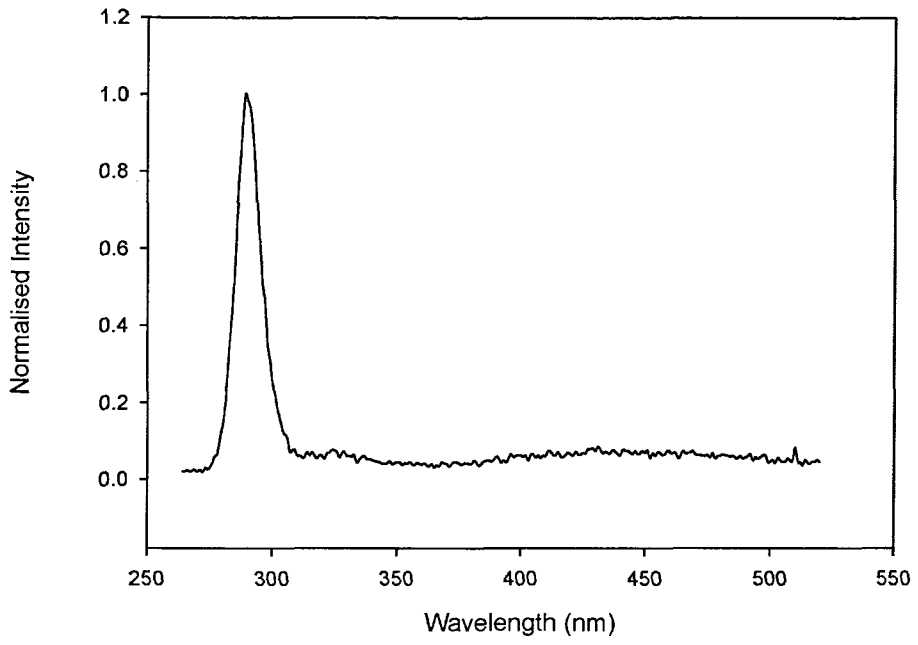

Figure 3.11

Spectral profile of the 295 nm LED (actual peak =296 nm)

The extended profile shows the device to be free from long wavelength emission previously observed with the 280 nm device (see Figure 3.5).

Figure 3.12 shows the pulse profile of the device. Included is the pulse profile of the IBH 5000F flashlamp for comparison.

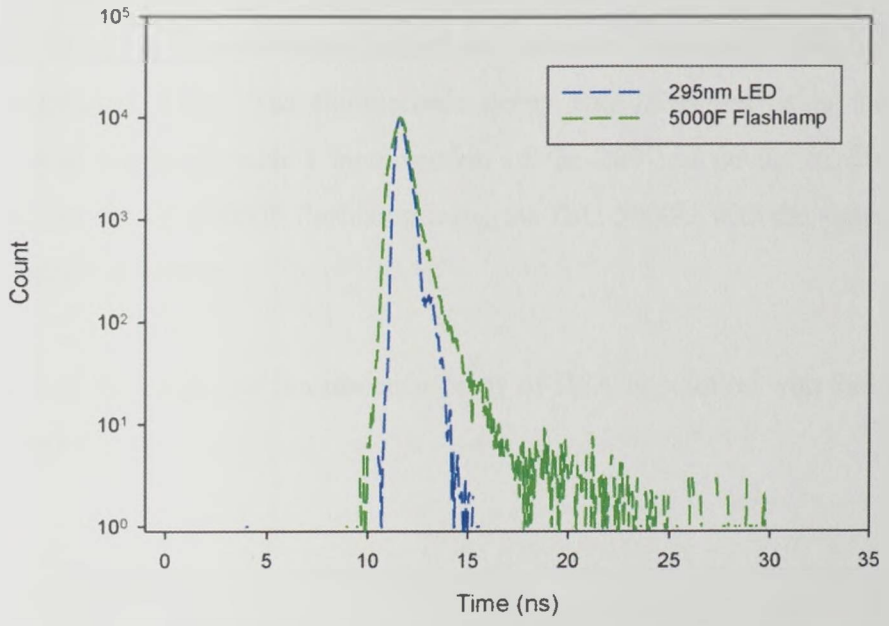

Figure 3.12

Pulse profile of 295 nm and IBH 5000F flashlamp (semi-logarithmic scale)

The measured instrumental FWHM of the diode is 640 ps. As with the 280 nm device, if we assume the detector exhibits its stated nominal timing jitter of ~200 ps, using addition in quadrature, the optical pulse width is calculated as ~600 ps. This device is also comparable with the flashlamp (~900 ps), and the semi logarithmic scale indicates it is free from pre- or after pulses.

3.3.2. Measurements on Human Serum Albumin

A 2.5 mg/ml solution of HSA in phosphate buffered saline (PBS) (pH 7.4) was prepared, and all measurements carried out in 4×1×1 cm quartz type fluorometric cells (Optiglass Ltd). The fluorescence decay was measured using the 295 nm device and compared with a later version of the 280 nm device in the previous section and the IBH 5000F flashlamp using the IBH 5000U with the same set up as in the previous section.

Figure 3.13 illustrates the fluorescence decay of HSA in solution with 295 nm diode excitation.

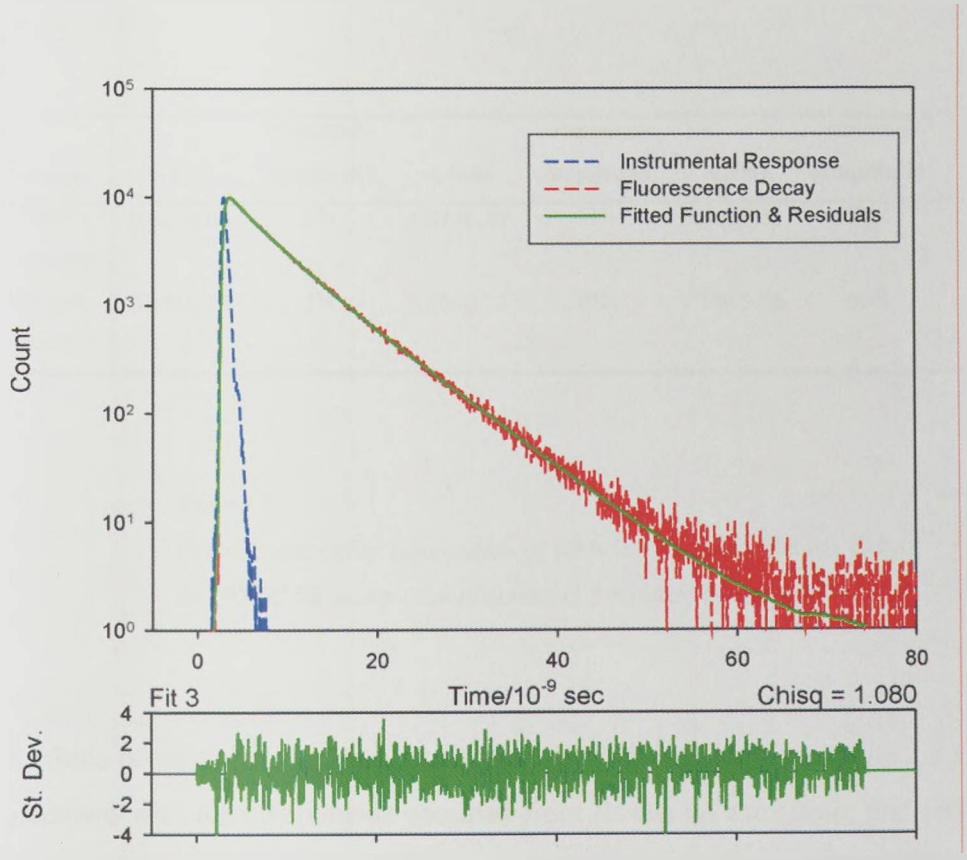

Figure 3.13

Fluorescence decay of 2.5 mg/ml HSA in PBS with 295 nm LED excitation

Again, the three exponential fit is attributed to the tryptophan conformer model. The LED gave a factor of ~20× greater fluorescence intensity than the flashlamp. This intensity equates to a collection time of <2 minutes, compared to ~30 minutes for the flashlamp collecting over 2,048 channels and to 10,000 counts in the peak channel. The χ^2 of 1.08 indicates the decay is free from scattered light, radio frequency interferences or temporal instabilities.

The fluorescence decay parameters are shown in Table 3.2. The parameters obtained from the flashlamp, with its monochromator tuned to 295 nm, are included for comparison.

Source	τ_1 (ns)	Relative Amplitude	τ_2 (ns)	Relative Amplitude	τ_3 (ns)	Relative Amplitude	χ^2
5000F flashlamp	0.92±0.41	3%	4.27±0.31	44%	7.45±0.11	53%	1.07
295 nm diode	0.45±0.26	2%	3.95±0.27	38%	7.25±0.08	60%	1.08

Table 3.3.
Fluorescence decay components of HSA in PBS using 295 nm diode and 5000F flashlamp. Errors quoted to 3 standard deviations.

The three decay components obtained from the 295 nm diode excitation are in good agreement with the components obtained from flashlamp excitation, and are within error of three standard deviations. The results are also consistent with triple exponential analysis by Vos, Hoek and Visser using an excitation wavelength of 295 nm.[96]

Fluorescence anisotropy measurements on the HSA in PBS sample were measured with the 295 nm diode and compared with a later, more intense 280 nm source. These experiments were carried out using the IBH 5000U fluorescence lifetime system equipped with rotating polarisers in a L-configuration (see Figure 2.4). With vertical excitation polariser orientation, the fluorescence decays were collected until a difference of 10,000 counts in the peak channel was obtained between vertical and horizontal emission orientations. Table 3.4 compares the rotational decay parameters between the 295 nm diode and the more intense 280 nm diode, when fitting to the anisotropy decay. Figure 3.14 shows the best fit plot to the fluorescence decay.

Source	τ_{r1} (ns)	Relative Intensity	τ_{r2} (ns)	Relative Intensity	Initial Anisotropy	χ^2
295 nm diode	1.04±0.68	0.4%	32.29±1.96	99.6%	0.198	0.98
280 nm diode	0.72±0.32	1.3%	20.56±1.28	98.7%	0.136	0.95

Table 3.4

Rotational parameters, and initial anisotropies, obtained from 295 nm and 280 nm devices. Errors are to three standard deviations.

Figure 3.14 shows the two-rotational decay of the protein with a zero residual anisotropy. As expected, the Brownian rotation of the whole protein is the dominant parameter (long decay component). Also, the 280 nm diode yields shorter decay components due to the energy transfer from the 18 tyrosines to the single tryptophan, and the loss of orientation during the transfer process, thus causing a more rapid fluorescence depolarisation in addition to that caused by tryptophan local motion. The effect of a decrease in anisotropy due to energy transfer has also been observed in the tryptophanyltryptophan dipeptide[9]. Although these decreases in anisotropy can be used to detect energy transfer it is difficult to use the data in a quantitative

manner. Even if the extent of depolarisation were known for a model compound, the effect may be different in a complex system such as HSA.

Vos, Hoek and Visser obtained a Brownian rotational time of HSA of 26 ns for excitation at 300 nm. This is shorter than the above value however, their data was fitted to a single rotational time[96] not taking into account the tryptophan local motion. Fluorescence anisotropy measurements using a flashlamp are very time consuming and close to the limit of what is comfortably measurable. The UV LEDs can allow anisotropy decay information to be obtained in a fraction of the time.

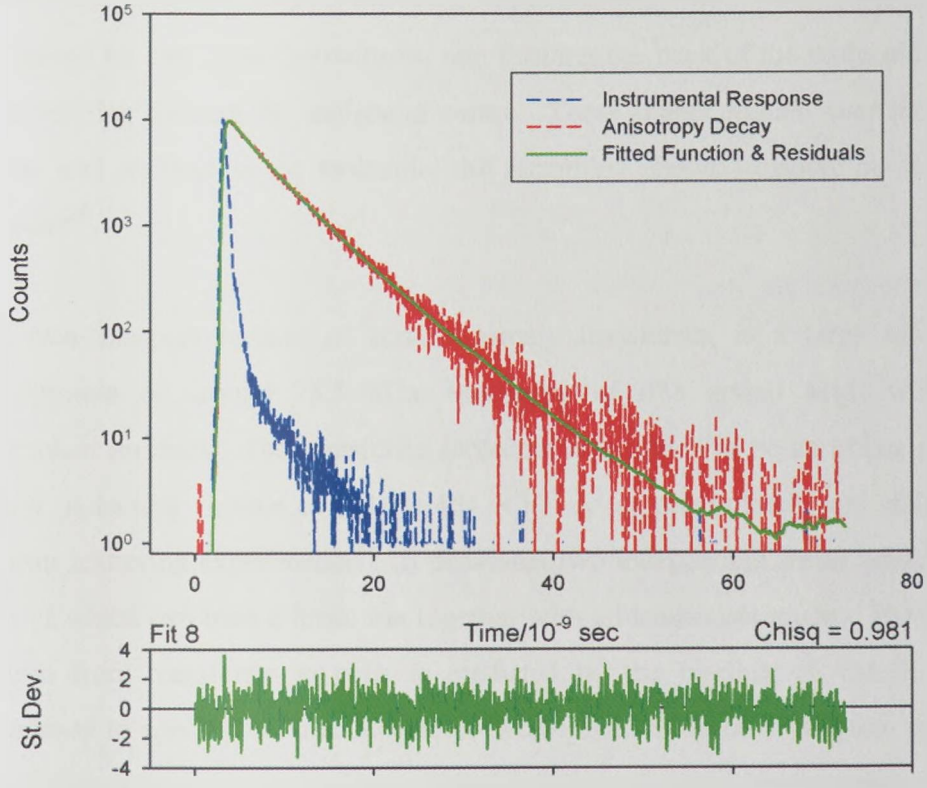

Figure 3.14

Fitted function to the anisotropy decay of 2.5 mg/ml HSA in PBS, using 295 nm diode excitation.

3.3.3 Measurements on Concanavalin A and Apo-Transferrin

Fluorescence decay and anisotropy measurements were also carried out on the proteins concanavalin A (conA) and apo-transferrin (aTf) to further demonstrate the usefulness of the 295 nm source. ConA is a relatively small protein consisting of identical protomers of molecular weight 25.5 kDa and a backbone of 237 amino acids. However at neutral pH it exists largely as a tetramer that dissociates to a dimer as the pH approaches 5.5.[97] Each monomer contains one saccharide binding site and therefore the tetrameric conA molecule can bind four saccharides. The protomer is a dome shaped molecule approximately 42 × 40 × 39 Å in size, dominated by two large β-structures, one forming the back of the molecule and the other running through the molecular centre. These sheets contain over half of the amino acid residues in the molecule; the remaining residues display no secondary structure[98].

The iron-transport protein of serum, namely transferrin, is a large monomeric glycoprotein of around 75.5 kDa, consisting of 678 amino acids with eight tryptophan residues. The transferrin molecule is assumed to be an oblate spheroid with a molecular volume of $(144 \pm 45) \times 10^3$ Å^3 as determined from small angle neutron scattering experiments[99]. It possesses two independent metal binding sites, each of which can bind a ferric ion together with a bicarbonate anion. The delivery of iron from transferrin to cells is mediated by the binding of transferrin-Fe^{3+} complexes to specific cellular receptors. Transferrin molecules therefore possess a specific receptor-recognition site in addition to the two metal binding sites. Around 14% of the polypeptide chain has a high probability of being α-helical and 10% of the chain are in an extended configuration[100].

Both of these proteins are of great clinical importance as they provide an opportunity for metabolite sensing. It has been demonstrated that there is potential for the use of

the glucose binding conA in sensing for glucose in diabetes[101-105], while the iron binding protein aTf has the potential for iron sensing in diseases such as anæmia[106-108].

Both conA (99.9%, Sigma-Aldrich Ltd, Dorset) and aTf (99%, Sigma-Aldrich, Dorset) were prepared at a concentration of 1 mg/ml in phosphate buffered saline at pH 7.4. Fluorescence measurements were carried out as before. The fluorescence decay parameters of both proteins are displayed in Table 3.5. The fitted functions to the decays of conA and aTf are illustrated in Figures 3.12 and 3.13 respectively.

Protein	τ_1 (ns)	Relative Intensity	τ_2 (ns)	Relative Intensity	τ_3 (ns)	Relative Intensity	χ^2
conA	0.68±0.03	16.9%	2.53±0.18	45.8%	5.74±0.07	37.3%	0.97
aTf	0.55±0.07	12.3%	2.32±0.06	65.6%	5.15±0.10	22.1%	1.01

Table 3.5
Fluorescence decay parameters of conA and aTf measured using 295 nm diode

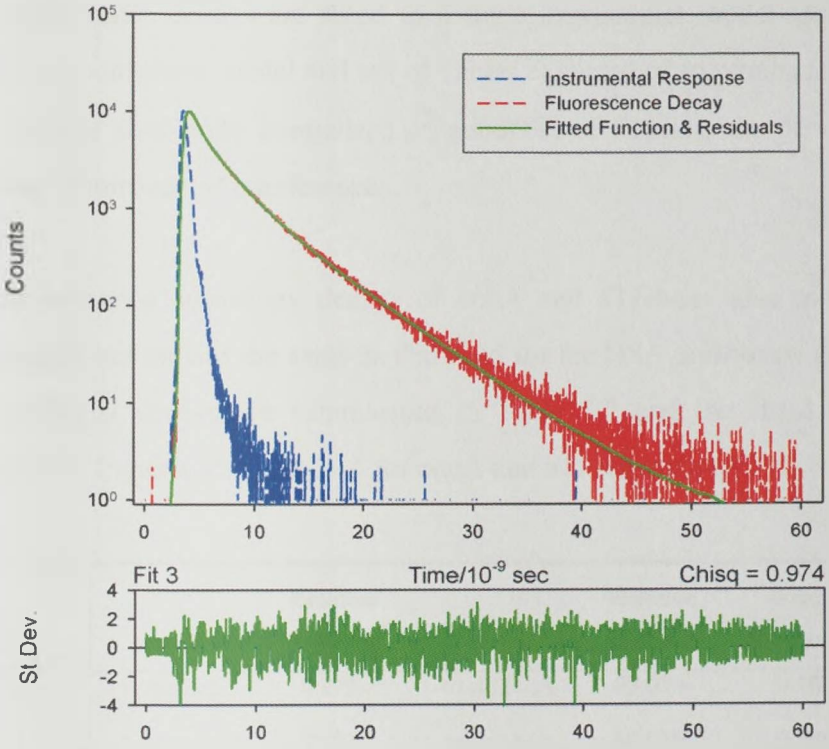

Figure 3.15 – Fitted function to fluorescence of conA

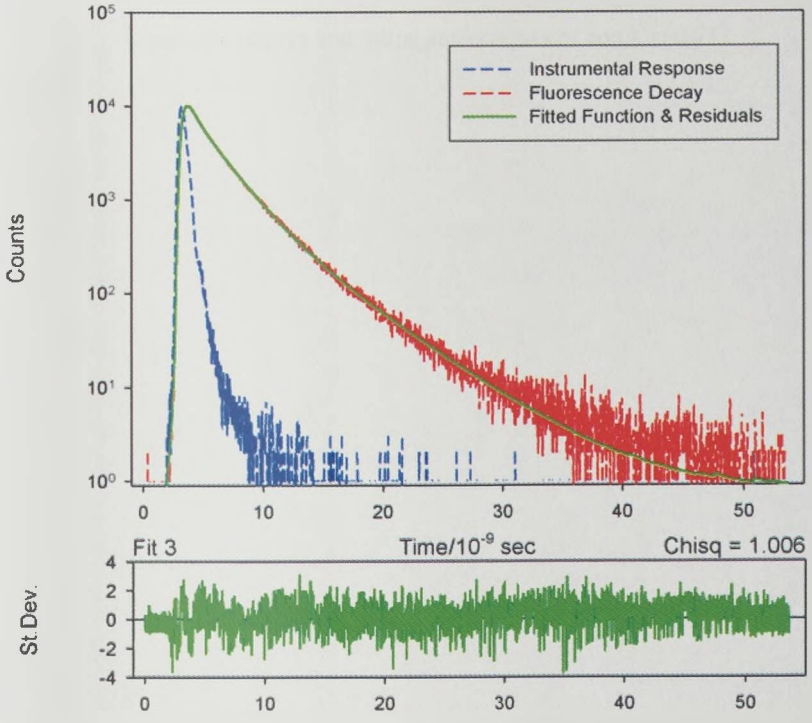

Figure 3.16 – Fitted function of fluorescence of aTf

The fluorescence decays are fitted to a three exponential model attributed to the tryptophan conformer model and are of values expected of tryptophan residues. The plots and the near unity normalised χ^2 goodness of fit show the decays to be free from any distortions or interferences.

The fluorescence anisotropy decays of conA and aTf were also measured. The instrumental set up was the same as that used for the HSA anisotropy measurements. The rotational decays are summarised in Table 3.7 and the fitted functions are displayed in Figures 3.13 and 3.14 for conA and aTf respectively.

Protein	τ_{r1} (ns)	Relative Intensity	τ_{r2} (ns)	Relative Intensity	Initial Anisotropy	χ^2
conA	1.05±0.28	0.97%	41.43±4.99	99.03%	0.197	1.05
aTf	1.16±0.19	0.03%	44.81±6.21	99.97%	0.183	1.09

Table 3.7

Rotational decays and initial anisotropies of conA and aTf

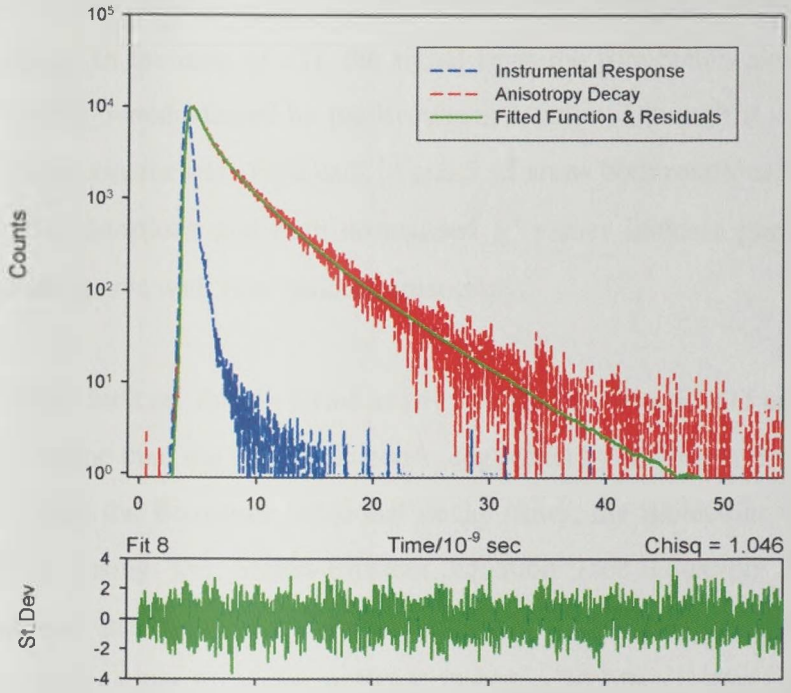

Figure 3.17 – Fitted function to anisotropy decay of conA.

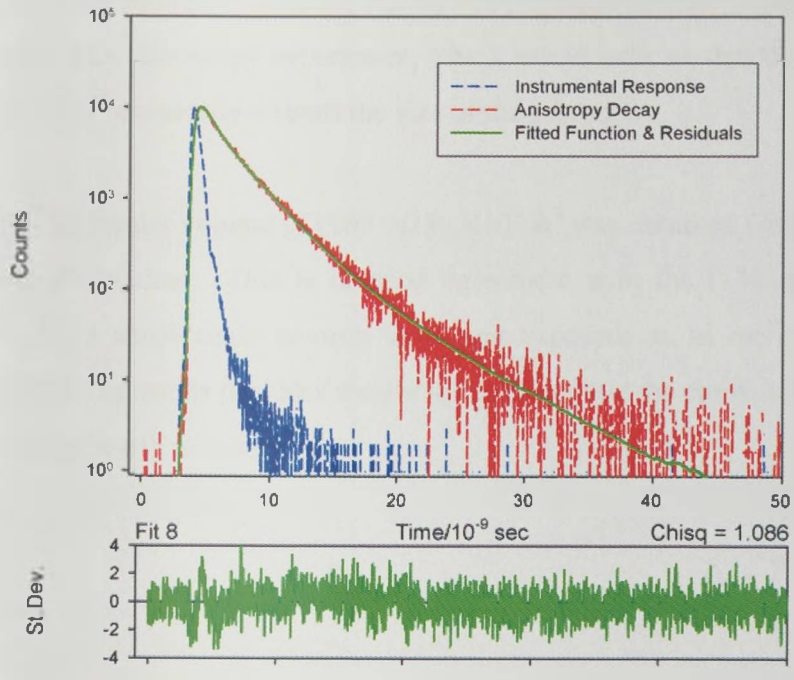

Figure 3.18 – Fitted function to the anisotropy decay of aTf.

For both conA and aTf, Table 3.7 shows that the Brownian rotation is the dominant parameter. In the case of aTf, the signal from the tryptophan local motion is very weak and is overshadowed by the Brownian rotation, although it is still visible with this device nonetheless. Figures 3.14 and 3.15 show both rotational decays to be free from any distortions and both normalised χ^2 values indicate good fits to the two rotational decays with zero residual anisotropy.

The results indicate that in saline at pH 7.4, the monomeric aTf occupies a slightly larger volume than the tetrameric conA, suggested by its longer Brownian rotational time. From the Brownian rotational decay times, the molecular volume V can be calculated using the Stokes-Einstein equation (see equation 2.33). For the calculations, the viscosity of the phosphate buffer solution (η) at 293 K is assumed to be the same as that for water at 293 K (1.005×10^{-3} Pa s). For conA, a molecular volume of (167 ± 20) $\times 10^3$ Å^3 was obtained. If we assume the conA tetramer at pH 7.4 is exactly 4 times the volume of the conA protomer, a volume of approximately 262×10^3 Å^3 is obtained[98]. This is significantly smaller that the value obtained from the fluorescence anisotropy experiment, which would indicate that the volume of the tetramer is not necessarily 4 times the size of the protomer.

For aTf, a molecular volume of (180 ± 25) $\times 10^3$ Å^3 was obtained from the Brownian rotational decay time. This is in good agreement with the (144 ± 45) $\times 10^3$ Å^3 obtained from small angle neutron scattering experiments as mentioned earlier[99]. The similarity in results provides weight to the claim that the conA tetramer is indeed smaller than the aTf monomer.

In measurements on various proteins, it has been demonstrated that the 295 nm pulsed diode has the ability to selectively excite tryptophan residues in proteins. Even in multi tryptophan residue proteins, although the kinetics are more complicated, fluorescence and anisotropy decay components are easily obtainable. This diode will provide greater opportunities for "lab-on-a-chip" devices based on intrinsic protein fluorescence.

3.4 The 265 nm Light-Emitting Diode

3.4.1 Characterisation of the Diode

In this section, the fluorescence decay of aqueous phenylalanine is measured using a 265 nm LED (Sensor Electronic Technology Inc.[73]), possibly the shortest wavelength demonstrated for this type of application. The results from the LED are compared to results from the IBH 5000F nanosecond flashlamp. The output power of this LED is 1.32 μW average power and 2.3 mW peak power. This compares favourably with the previous sources summarised in Table 3.2. The powers were measured (Hamamatsu power meter Type No. S1227-1010BQ) as described in the previous sections of this chapter. Figure 3.19 illustrates the spectral profile of the LED recorded using a SPEX FluoroMax2 with 2 nm spectral bandwidth.

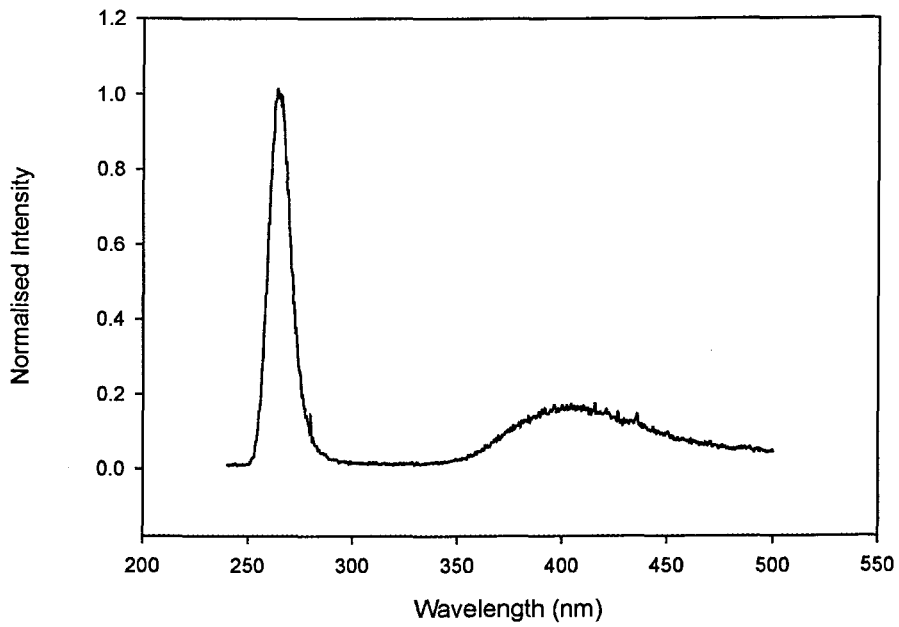

Figure 3.19

Spectral profile of the 265 nm LED (actual peak =265 nm).

The spectral FWHM of the 265 nm LED is ~12 nm. The extended scan to 500 nm illustrates the presence of a long wavelength emission as seen in the initial 280 nm device[21]. As in the 280 nm LED experiments, it was necessary to first pre-filter the LED source to ensure the long wavelength peak is not detected along with the Stokes-shifted fluorescence. This long wavelength emission is further discriminated against by using a second monochromator to select fluorescence. This long wavelength emission, similar to the long wavelength emission from the 280 nm device, cannot be used to excite other fluorophores due to its long decay time.

A typical LED pulse width is illustrated in Figure 3.20. The pulse width of the IBH 5000F nanosecond flashlamp is included for comparison.

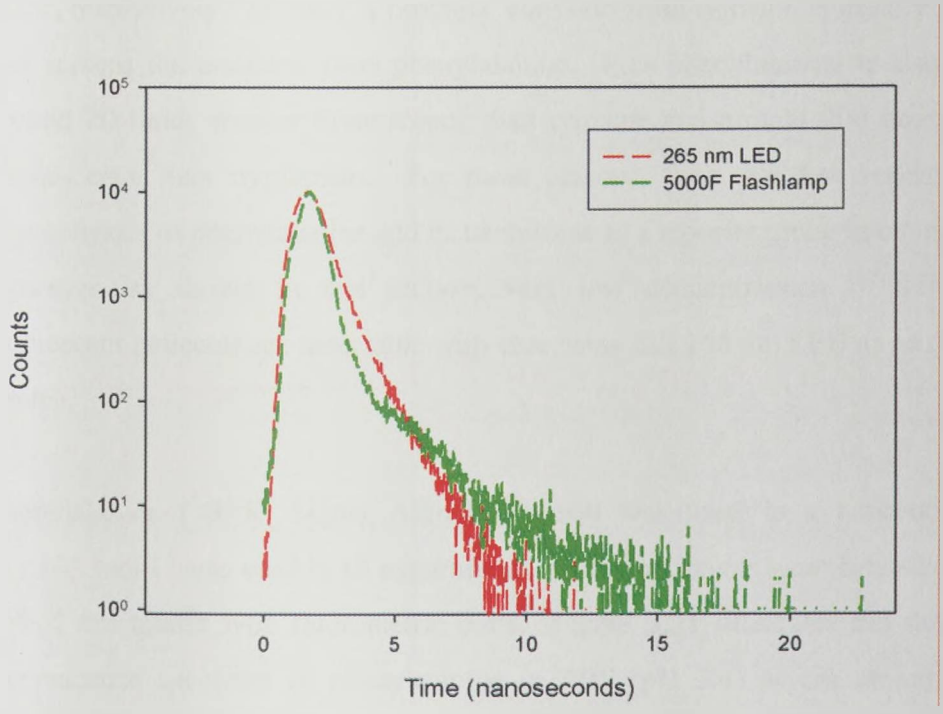

Figure 3.20

Pulse profile of the 265 nm LED with the IBH 5000F included for comparison (semi-logarithmic scale).

The measured FWHM of the diode is 1.2 ns and is comparable to the nanosecond flashlamp (~0.9 ns), although slightly broader. The semi-logarithmic scale indicates the source is free from unwanted pre- or after pulses.

3.4.2 Measurements on Aqueous Phenylalanine

Phenylalanine is the one of the naturally occurring intrinsically fluorescent amino acids (see Figure 2.9). When all three intrinsically amino acids are present in a protein, the protein is referred to as a "class B protein" and when only phenylalanine and tyrosine are present, the protein is referred to as a "class A protein"[109]. In class B proteins, tryptophan can be selectively excited at a wavelength of 295 nm or above. Below 290 nm and 270 nm absorption into tyrosine and phenylalanine takes place, respectively. In class A proteins, emission from tyrosine is usually strongest and screens the emission from phenylalanine. Free phenylalanine is also exhibits around 20 times weaker fluorescence than tyrosine and around 200 times weaker fluorescence than tryptophan. For these reasons, there are few reports on the photophysics of phenylalanine and its usefulness as a reporter probe in biomolecules. However, as shown in this section, very low concentrations of this weakly fluorescent molecule are detectable with ease using this 265 nm LED as an excitation source.

Phenylalanine (≥99%, Sigma Aldrich, Dorset) was used in a concentration of 3×10^{-6} mol l^{-1} was used in all experiments. All experiments were carried out using $4 \times 1 \times 1$ cm quartz type fluorometric cells. Figure 3.21 illustrates the steady-state fluorescence spectrum of phenylalanine in PBS (pH 7.4) at the aforementioned concentration recorded using the 265 nm LED under TCSPC conditions. Figure 3.21 illustrates that the well-known fluorescence spectrum of phenylalanine is replicated without distortion or artefacts[110].

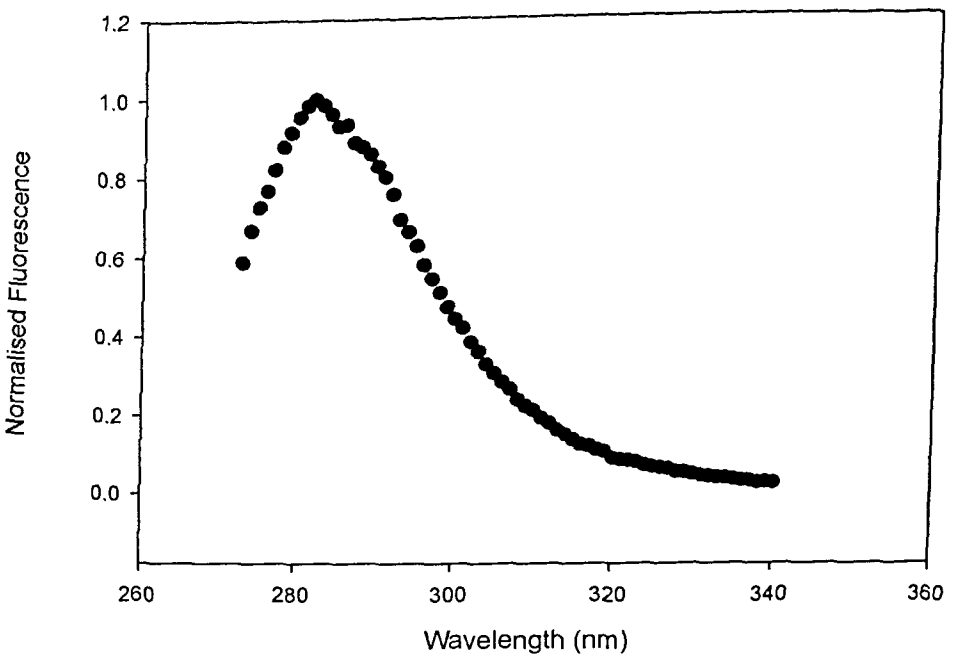

Figure 3.21

Steady-state fluorescence spectrum of phenylalanine in PBS (pH 7.4, 3×10^{-6} mol l^{-1}) using the 265 nm LED under TCSPC conditions.

The fluorescence decay parameters of phenylalanine were also recorded using the IBH 5000U fluorescence lifetime system, set up as before with a resolution of 29 ps per channel. A phenylalanine fluorescence count rate of 6.4 kHz was achieved with the LED using 8 nm excitation and emission bandpasses. This is a $\geq$200 times greater count rate than with the flashlamp at the same bandpass lowering the collection times to a few minutes, thus reducing the susceptibility of systematic errors.

Initially the fluorescence decay of phenylalanine at pH 7.4 was fitted to a mono-exponential function as used by others[111,112]. Using reconvolution with the χ^2 goodness of fit criterion, a decay time of 7.47 $\pm$0.01 ns was obtained, consistent with previous results[111,113]. Although the low χ^2 of 1.095 suggests little possibility of a second excited species, a less intense component was observed when fitting to a two-

exponential function with $\chi^2 = 1.077$ (see Table 3.8). Figure 3.22 shows the fluorescence decay with one- and two-exponential fitted functions and residuals for phenylalanine at pH 7.4.

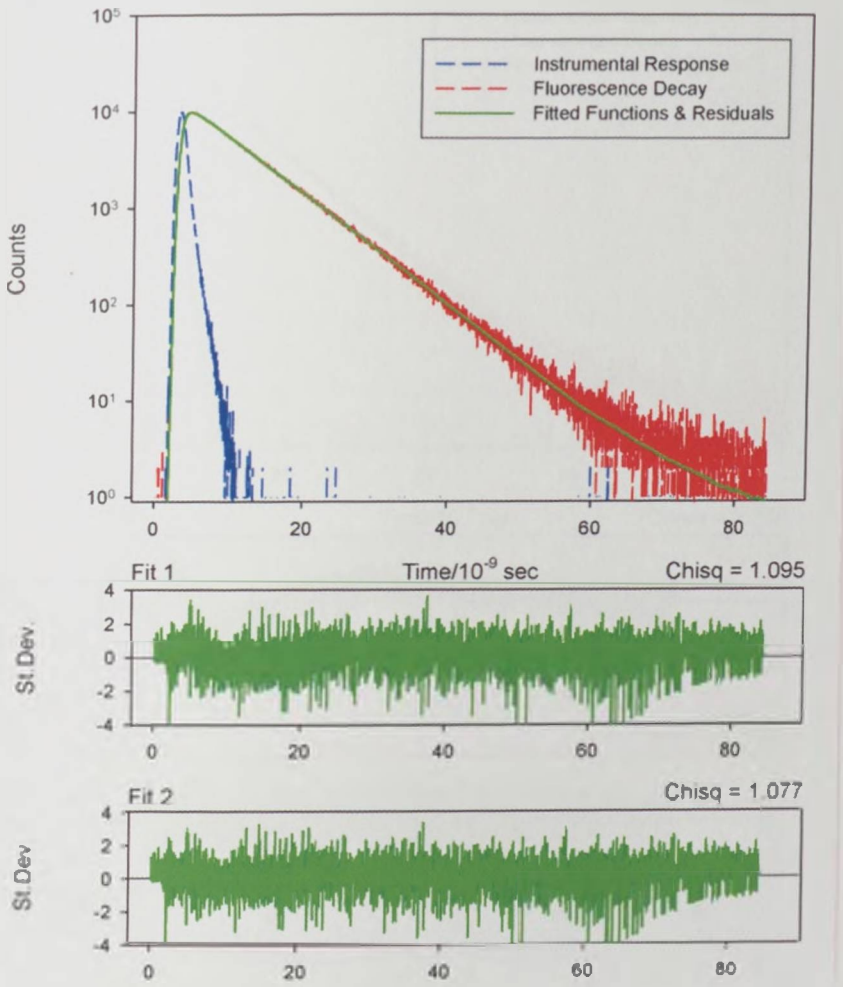

Figure 3.22

Phenylalanine in PBS (pH 7.4) fluorescence decay fitted to one- (Fit 1) and two-exponential (Fit 2) functions showing residuals for both functions. Obtained using the 265 nm LED.

The second component becomes more evident as the pH is increased from 7.4 to 9.2, observed with both LED and flashlamp sources. Here it is clear that a mono-

exponential function provides an inadequate fit to the data, and a second component is essential (Figure 3.23)

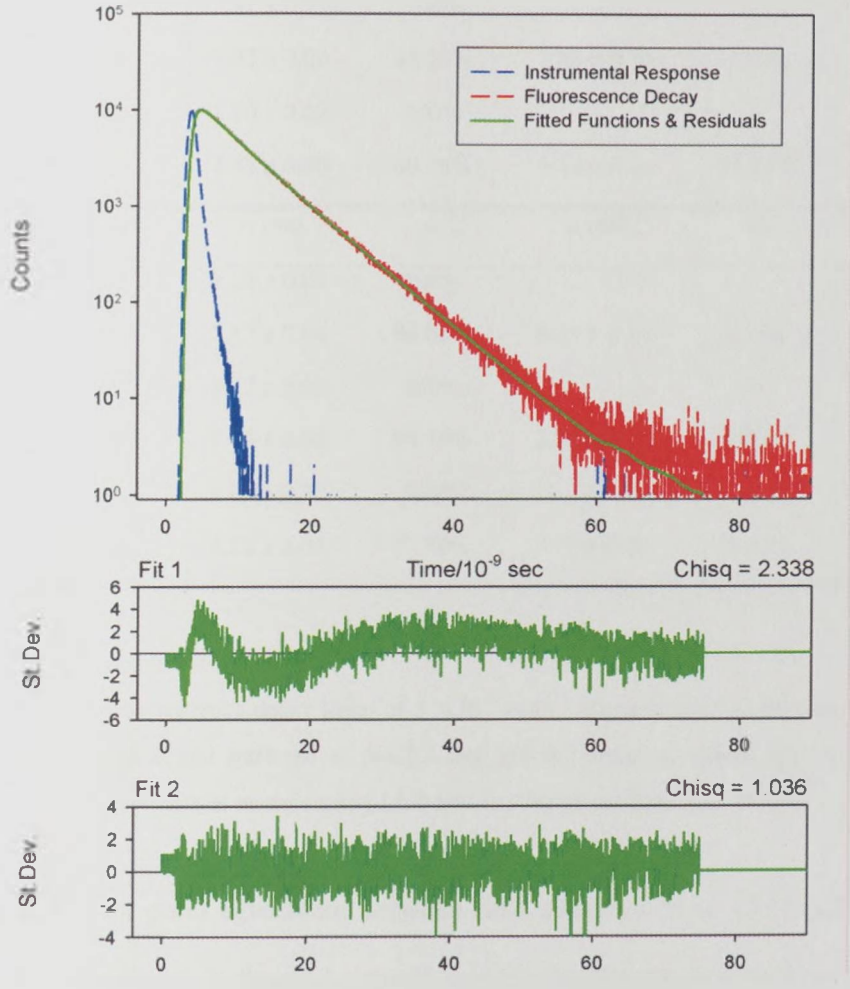

Figure 3.23

Phenylalanine in borate buffer (pH 9.2) fluorescence decay fitted to one- (Fit 1) and two-exponential (Fit 2) functions showing residuals for both functions. Obtained using the 265 nm LED.

Fluorescence from the water or buffer solution was negligible. Table 3.8 summarises the decay components obtained from LED and flashlamp excitation for phenylalanine at pHs 6, 7.4 and 9.2.

Phe, LED exc.	τ_1 (ns)	α_1	τ_2 (ns)	α_2	χ^2
pH 6.0 – 1 exp	6.95 ± 0.02	100%	–	–	1.21
pH 6.0 – 2 exp	7.12 ± 0.04	95.19%	3.61 ± 0.10	4.81%	1.08
pH 7.4 – 1 exp	7.47 ± 0.01	100%	–	–	1.10
pH 7.4 – 2 exp	7.53 ± 0.03	98.25%	3.86 ± 0.13	1.25%	1.08
pH 9.2 – 1 exp	7.29 ± 0.02	100%	–	–	2.34
pH 9.2 – 2 exp	7.31 ± 0.05	68.76%	4.43 ± 0.24	31.24%	1.04
Phe, flashlamp exc.	τ_1 (ns)	α_1	τ_2 (ns)	α_2	χ^2
pH 6.0 – 1 exp	7.33 ± 0.02	100%			1.24
pH 6.0 – 2 exp	7.47 ± 0.04	94.85%	4.01 ± 0.10	5.15%	1.09
pH 7.4 – 1 exp	7.43 ± 0.02	100%	–	–	1.29
pH 7.4 – 2 exp	7.60 ± 0.03	96.10%	2.89 ± 0.54	3.90%	1.02
pH 9.2 – 1 exp	6.00 ± 0.02	100%	–	–	2.48
pH 9.2 – 2 exp	6.72 ± 0.05	73.70%	3.76 ± 0.23	26.30%	1.05

Table 3.8

Fluorescence decay times of 3 $\times 10^{-6}$ mol l^{-1} phenylalanine in water at pH 6 and buffered at pH 7.4 and pH 9.2 fitted to mono and bi-exponential models using LED and flashlamp excitations at 265 nm.

Table 3.8 shows good agreement between data obtained from LED and flashlamp excitation. However, it should be noted that the flashlamp data required correction for scattered excitation light due to the wider bandpass of 16 nm excitation and 32 nm emission required due to the low concentration and weak fluorescence of phenylalanine.

Unlike the other two fluorescent amino acids tyrosine and tryptophan, previous studies on aqueous phenylalanine over a range of pHs (including pH 6 reported here)

and in other homogeneous solvents, seem only to have reported evidence for a mono-exponential fluorescence decay. When comparing to tyrosine and tryptophan, this is in some ways surprising given that the identical side-chain containing carboxyl and amino groups (Figure 2.9) occurs in all three fluorescent amino acids. Moreover, the rotamer model describing rotations of the side chain is widely accepted as a suitable model to explain the complex multi-exponential fluorescence decay kinetics of tyrosine[114] and tryptophan[49,50,55]. It is this rotamer which can perturb according to pH, the phenyl π-electrons responsible for the fluorescence. However, the existence of rotamers in phenylalanine has hitherto lacked supporting evidence because of its apparent mono-exponential decay in solution[111-113]. The findings presented here differ from these previous results and confirms there is much more commonality between the photophysics of all three fluorescent aromatic amino acids than has hitherto been recognised. This data suggests there are at least two ground state rotamers of phenylalanine, which co-exist on a time-scale longer than their fluorescence decay times. The increased relative intensity of the shorter component at pH 9.2, may be due to an orientation of the molecule where the deprotonated carboxyl group is closest to the phenyl ring, similar to tryptophan. At neutral pHs the decay due to this orientation is less perhaps due the lesser electron density on the carboxyl group. In this context it should be noted that a tri-exponential fluorescence decay of phenylalanine embedded in a peptide sequence has been reported previously[113].

The convenience and ease of use of the 265 nm LED may well stimulate further research using phenylalanine photophysics in protein folding via energy transfer

from phenylalanine to tyrosine and/or tryptophan, or where only phenylalanine residues occur. While the 265 nm LED completes the semiconductor wavelengths available for exciting all three fluorescent amino acids it should be noted that other fluorescent systems, for example organic polymers such as polystyrene, skin chromophores such as urocanic acid and other small aromatic molecules such as toluene, can also be efficiently excited at 265 nm.

3.5 Summary

The use of the 280 nm diode in the Section 3.2 was a significant step in miniaturisation of pulsed UV sources and was ideal for tyrosine excitation. However, excitation of 295 nm is preferred for protein fluorescence so as to only excite tryptophan residues as it is the most commonly used intrinsic probe in the investigation of class B proteins. Although in class A proteins, the 280 nm diode would be most useful. The use of phenylalanine as a probe for protein behaviour may be more widely used in the future, as the 265 nm diode can excite phenylalanine fluorescence decays with ease. The most noticeable and important difference between these UV sources and the coaxial flashlamp is their ability to allow collection of fluorescence decays in a short time. For standard fluorescence decay measurements on the same sample, the flashlamp will require around 30 minutes of operation to allow collection of 10,000 counts in the peak channel, compared to around 2 minutes for the LED.

In fluorescence anisotropy measurements, the LED can allow peak channel collection to 10,000 counts of a difference between polarisations in less than 1 hour, whereas similar measurements using flashlamps can command collection times in excess of 5 hours. This swift collection time also eliminates the risk of drift in components when collecting over extended periods of time. The similarity in molecular volume values obtained from anisotropy measurements when compared

with previous scattering measurements, demonstrates that this source can be used reliably in many volume sizing experiments. This is of particular advantage as fluorescence anisotropy measurements can be carried out at a fraction of the cost of X-ray or neutron scattering experiments.

It is expected that there will be greater use of UV LEDs for time resolved fluorescence research. Most recently, researchers at the University of Hawaii and ISS Inc. have incorporated 280 nm and 300 nm LEDs into the study of proteins in frequency domain fluorescence spectroscopy[115] and researchers at Vilnius University and Sensor Electronic Technology Inc. have reported high-frequency modulation of 340 nm and 280 nm UV LEDs up to 200 MHz and their application for frequency domain fluorescence[116]. This increasing use of UV LEDs may not necessarily lead to the demise of the nanosecond flashlamp due to its broadband spectrum, which is essential for time resolved emission spectroscopy. Also, the ultra fast pulses of mode-locked lasers still offer the best in time resolution. On the other hand, the compactness and ease of use of the LEDs will make time-resolved fluorescence more widely used by researchers not only in areas mentioned above, but also in emission spectroscopy, microscopy and imaging.

Although the advent of UV LEDs for fluorescence is significant, it may one day be superceded by the design of UV laser diodes. Currently, laser diodes can be fabricated using similar drive circuitry and package sizing as LEDs. They are superior to LEDs due to their sharper spectral and pulse widths, however the shortest wavelength available is ~370 nm, precluding them from intrinsic protein fluorescence studies. It will however, only be a matter of time before laser diode design permits the fabrication of compact UV laser diodes, thus providing the ultimate in pulsed UV sources.

4

Silica Sol-Gel Synthesis

4.1 Introduction

4.1.1 Outline

The work and discussion in this chapter is concerned with the synthesis of UV transparent, pH neutral and harmful by-product free silica sol-gels for the entrapment of biologically active molecules for the use in "lab-on-a-chip" sensors based on fluorescence spectroscopy. Sol-gels typically exhibit pore sizes of <10 nm,[117] and are capable of excluding high molecular weight interferents, so are perfectly suited to such sensor applications.

The interfacing of biological reagents to inorganic surfaces has been a topic of extensive research for three decades and has applications other than sensors, such as separation science and bioreactor design[118]. Additionally, ceramics including those based on sol-gels can be used in applications in the repair of bone defects, bone augmentation and coatings for metal implants[119].

The first such report of protein encapsulation in a sol-gel matrix was in 1990 by Braun *et al*[120]. The preparation of biologically doped materials via the sol-gel process requires that several parameters be accommodated simultaneously: 1. The material must be amenable to aqueous solutions, 2. The reaction must be compatible with pH and ionic strength, 3. The process must be carried out at near room temperature, 4. The pore size must be sufficiently small to prevent leaching of the biomolecule but large enough to allow smaller analytes to enter the matrix, 5. The internal environment should be modified to maximise biomolecule activity, 6. The

material should be optically transparent and 7. The process should be easily reproducible and amenable to bulk glasses, thin films etc[121].

The sol-gel process for oxides is the name given to any of a number of processes that involve a single phase liquid, or, a stable suspension of colloidal particles that undergoes a transition to a rigid two phase system of solid and solvent filed pores[122]. The term "sol" is given to dispersions of colloidal particles in a liquid and the term "colloid" is given to solid particles with diameters of 1-100 nm. A "gel" is an interconnected rigid network with pores of submicrometre dimensions and polymeric chains whose average length is greater than a micrometre. The interest in the sol-gel processing of inorganic and glass materials began in the mid-1800s with Ebelman reporting on obtaining glass-like material from tetraethoxysilane (TEOS)[123] and drawing fibres from the viscous gel[124]. Also, Graham reported on the properties of silicic acid and other analogous colloidal substances[125]. However, at this time extremely long drying times of around one year or more were necessary to avoid the fracturing of silica gels into a fine powder, so consequently the interest was limited. The difference between modern derived sol-gel materials and the initial works of Ebelman and Graham is that gels can be obtained in minutes, rather than years. A problem still remaining is that of the fracturing of the gels. The synthesis conditions are critical to successful accomplishment of fracture-free gels.

Hench and West classify the three processes in which sol-gels are synthesised, namely: 1, gelation of a solution of colloidal powders, 2, the hydrolysis and condensation of an alkoxide or nitrate precursor followed by hypercritical drying of gels, and 3, hydrolysis and condensation of alkoxide precursors followed by aging at ambient conditions[126]. This work will discuss the first and third methods for synthesis of a biocompatible sol-gel. The common reaction of sol-gel processing in this work is the condensation reaction in silicic acid. Silicic acid is a highly reactive species and rapidly clusters to form the rigid network, with the elimination of water, as represented in Figure 4.1

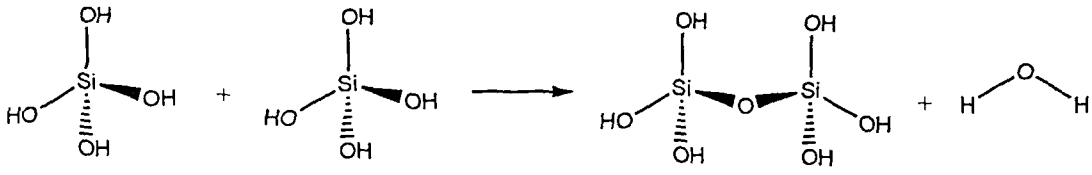

Figure 4.1

The first step in the polycondensation reaction of silicic acid.

Other centres such as titanium, vanadium, aluminium or cerium may be used in place of silicon in Figure 4.1 to alter the material properties.

4.1.2 Gelation

The gelation point of a sol-gel system is easy to observe qualitatively and easy to define in abstract terms. However, it is very difficult to measure this analytically. The gelation point, t_{gel}, can be defined as the point in the reaction when the sol becomes a gel and it can support a stress elastically. It can also be defined as the point when the network spans the vessel. The collisions that occur between silicic acid species lead to further polycondensation, resulting in the formation of a gel by way of covalent siloxane bonds. However these covalent siloxane bonds may be cleaved, which allows gels to exhibit slow but irreversible deformations. This gives rise to the concept of "strong" and "weak" gels depending on whether siloxane bonds are permanent or cleavable. As a consequence, the chemical reactions that give rise to the gelation continue long beyond the point of gelation, permitting flow and producing gradual changes in the structure and properties of the gel[117]. For this reason, the definition of t_{gel} can be a crude one. If t_{gel} corresponds to when a gel reaches a certain viscosity in one system, it may be observed seconds or even hours before or after in another system. For this reason a more elegant way to look for the gelation point, based on measuring the viscoelastic behaviour of the gel as a function

of the shear rate is carried out, although this will not be discussed in this work. It has also been shown by Assink and Kay that NMR provides a means to investigate the chemical kinetics and structure of a sol-gel throughout its reaction process, in considerable detail[127].

The aggregation and gelation can be described in its simplest form, by the Smoluchowski or kinetic rate equation. The equation is useful as it can provide a qualitatively correct mean field description of the gelation process and it is a useful framework in which to classify growth. However it cannot predict cluster structure, although growth kinetics and size distributions predicted can be in agreement with experimental data because of the limitless number of reaction kernels[128]. The Smoluchowski equation can be expressed in terms of the time evolution of m-mers, $N(m)$, in terms of the reaction kernel K_{ij}, which gives the probability of an i-mer reacting with a j-mer.

$$\frac{dN(m)}{dt} = \frac{1}{2}\sum_{i+j=m} N(i)K_{ij}N(j) - N(m)\sum_{j=1}^{\infty} K_{ij}N(j) \qquad (4.1)$$

The first summation represents the creation of m-mers from binary collisions of i-mers and $(m\text{-}i)$-mers and the second summation represents the annihilation of m-mers due to binary collisions with other clusters. It can be difficult to determine a reaction kernel for a given physical system, but fortunately it can be simplified by the homogeneity of the kernel dominating the time evolution of $N(m)$. The kernels can be classified by the relative probabilities of large clusters sticking to large clusters and small clusters sticking to large clusters.

Aggregation of clusters is highly dependent, among other factors, on the pH and the temperature of the solution[117]. At neutral pH, the pH of interest in this work, the gelation time is shortest and can be represented by the following graph:

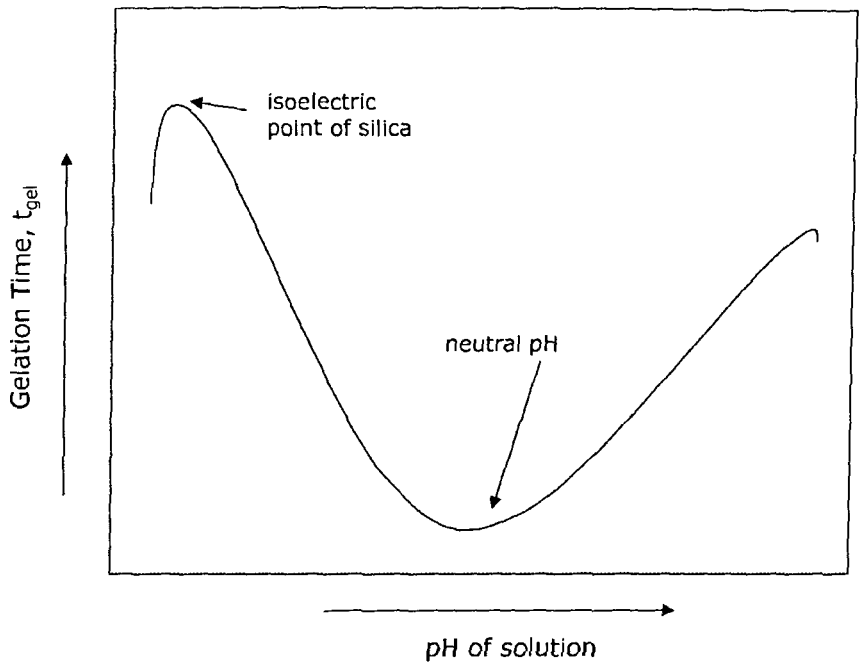

Figure 4.2

Representation of gelation time t_{gel} as a function of solution pH.

Gels prepared by destabilisation of a silica sol will have a maximum gelation time near the isoelectric point of silica, around pH 2, and a minimum gelation time at near neutral pHs[129]. The gelation time of two solutions sols at the same pH may not be identical as other factors such as counterions in acid or base catalysed reactions, water content and metal ions will affect gelation time.

4.1.3 Ageing

The chemical reactions that cause gelation continue long after the gel point to produce strengthening, stiffening and shrinkage of the network. It is currently accepted to categorise the processes of change after gelation as "polymerisation",

"syneresis" and "coarsening"[117,126]. Polymerisation is the increase in connectivity of the network produced by further condensation reactions. In addition to further condensation, further hydrolysis can occur as well as re-esterification. Re-esterification can be suppressed however, if excess water is used. Syneresis is the process of the shrinkage of the sol-gel network resulting in expulsion of liquid from the pores. It is this process that is believed to be caused by the same condensation reactions that produce gelation. Shrinkage is ultimately stopped by the remaining repulsive forces. Coarsening is the process of dissolution and reprecipitation driven by differences in solubility between surfaces with different radii of curvature. The result is to reduce the net curvature of the solid phase. Small particles disappear and small pores are filled in, so the interfacial area decreases and the average pore size increases. This process does not produce shrinkage, since the centres of the particles do not move closer together.

These phase transformations in the wet stage, along with variations in time, temperature and pH, are all processes that can alter the ageing process of sol-gels. These techniques can allow strengthening to the structure, without greatly affecting the pore structure, and enlarge the pore size and reduce the surface area of the sol-gel.

4.1.4 Drying

It is generally accepted that there are three stages of drying[117]. During the first stage the decrease in volume of the gel is equal to the volume of the liquid lost by evaporation. The compliant gel network is deformed by the large capillary forces, which cause the shrinkage of the object. The rate of evaporation per unit area of the drying surface is independent of time for gels made by colloidal precipitation or by base catalysed alkoxides that have pores $\geq$20 nm. However, analysis of acid-catalysed alkoxide gels shows that for pores $<$20 nm, the rate of drying is not

constant rather it decreases substantially[126]. The first stage of drying is complete when shrinking ceases.

The second stage begins when the "critical point" has been reached. This occurs when the strength of the network has increased due to greater packing density, sufficient to resist further shrinkage. As the gel network resistance increases, the radius of the meniscus equals the radius of the pore. This condition creates the highest capillary pressure causing the pores to empty. The liquid from the pores flows to the surface where evaporation takes place, driven by the gradient in capillary stress.

The third stage of drying is reached when the pores have substantially emptied and surface films along the pores cannot be sustained. The remaining liquid can only escape by evaporation from within the pores and diffusion of vapour to the surface. During this period, there are no further dimensional changes but just a slow progressive loss of weight until equilibrium is reached, determined by ambient temperature and partial pressure of water.

4.1.5 Cracking

Hench and West[126] describe cracking as "drying failure". Samples can fail at distinct points in the drying sequence. Although dried gels were not used in protein encapsulation this work, gels were dried to investigate their characteristics. Cracking during the first stage of drying is not common but it can occur when the gel has had insufficient ageing strength and does not possess the dimensional stability to withstand the increasing compressive stress[117]. In the majority of cases, most failures occur in stage two at the point when the gels stop shrinking. As the second stage is underway, the modulus of the gel is of the order of 100 MPa. The pores that empty first stop shrinking at the point of emptying and can only passively shrink under influence of nearby saturated pores. The possibility of cracking at this point is

great due to high stress and low strain tolerance of the material[126]. Cracking does not occur in the final stage of drying as the moisture level and thus the stress is considerably diminished by this point.

The formation of the silicic acid species, and the subsequent creation of the silica network in this research, was formed from an array of colloidal particles (§4.2) or from the simultaneous hydrolysis and condensation reaction of an alkoxysilane (§4.3)

4.2 Synthesis from Powder

4.2.1 Background Chemistry

Work in this section is concerned with the production of a biocompatible sol-gel from the high grade Aerosil 300 silica powder. This particular silica was chosen due to its high purity and negligible auto fluorescence. The silica powder is dissolved in a basic solution such as sodium hydroxide to produce a sodium silicate. Extensive crystallographic studies by Jamieson and Dent Glasser have shown that hydrated sodium silicates form a Na_2O-SiO_2-H_2O system and contain the tetrahedral $[H_2SiO_4]^{2-}$ group[130-132]. Their calculations and considerations of bond lengths and angles lead them to the conclusion that the constitutional formulae are $Na_2(H_2SiO_4).nH_2O$ where the number of associated water molecules depends on the ratios used. The reactive silicic acid can be formed from this high pH solution of sodium silicate by reaction with acid. Although isolated units of $Na_2(H_2SiO_4)$ will not be present, the reaction of sodium silicate with acid can be represented by equation 4.2.

$$Na_2(H_2SiO_4) + 2H^+ \longrightarrow Si(OH)_4 + 2Na^+ \qquad (4.2)$$

The sodium silicates will solidify of their own accord as the water solvent is allowed to evaporate, although they will not form a gel. Rather they will form complicated sodium silicate crystals with large unit cells.

4.2.2 Experimental Details

Investigation of silica in alkali metal hydroxides by Tanaka and Takahasi has shown that a maximum of 0.1 g of silica can be dissolved in 20 cm^3 of 0.1 mol l^{-1} NaOH or KOH.[133] For this reason 1.94 g of Aerosil 300 (Ineos Silicas) was dissolved in 40 ml

of 0.97 mol l^{-1} sodium hydroxide solution (Volumetric Standard, Sigma-Aldrich Co., Dorset) with vigorous overnight stirring. The resultant clear solution was sealed and stored at 4 °C. If the repeating unit cell in silica is SiO_2, the reaction with aqueous sodium hydroxide can be represented by

$$SiO_{2(s)} + 2NaOH_{(aq)} \longrightarrow Na_2(H_2SiO_4)_{(aq)} \qquad (4.3)$$

The sodium silicate solution was then added to 0.97 mol l^{-1} hydrochloric acid (Sigma-Aldrich, Dorset) at 4 °C to initiate the reaction. Universal indicator was used to ensure a pH neutral solution. The volume of acid required to neutralise a specific volume of sodium silicate was determined on a trial and error basis. Due to the fast gelation of sodium silicate solutions at near neutral pHs, temperatures were kept to 4 °C and gels were not produced in bulk.

4.2.3 Results

Time resolved fluorescence measurements were carried out on the Edinburgh Instruments 299/T fluorometer. The UV radiation required for tryptophan excitation was provided by the IBH co-axial nanosecond flashlamp operating with a repetition rate of 40 kHz and a spark voltage of ~7.5 kV. The lamp was capable of producing a pulse of 1.6 ns FWHM. Detection was by means of a Philips XP2020Q free standing photomultiplier. Data was analysed with the IBH decay analysis software library v4.2 for MS-DOS.

Initially the decay components of L-tryptophan in solution were compared to an identical concentration of L-tryptophan encapsulated in an Aerosil 300 based sol-gel. The use of tryptophan as a probe for investigating protein behaviour has been investigated in this group in the case of AOT microemulsions[53]. For comparison with sol-gels a 10^{-5} mol l^{-1} solution of L-tryptophan (99.9%, Sigma-Aldrich Ltd., Dorset) was prepared in phosphate buffered saline (Oxoid Ltd.) and a 10^{-5} mol l^{-1}

concentration of L-tryptophan in sol-gel prepared using the methods described in §4.2.2. Fluorescence decays were measured with an excitation monochromator tuned to the excitation maximum of tryptophan (279 nm), and a 310 nm high pass filter used to select fluorescence.

Table 4.1 illustrates the triple decay components of L-tryptophan in saline and in Aerosil 300 based sol-gel at ~pH 7.

Media	τ_1 (ns)	Relative Intensity	τ_2 (ns)	Relative Intensity	τ_3 (ns)	Relative Intensity	χ^2
Saline	0.59±0.04	4.48%	2.71±0.07	92.51%	5.90±0.90	3.01%	1.085
A300 gel	0.49±0.05	3.99%	3.03±0.07	87.81%	7.71±0.51	8.20%	1.109

Table 4.1
Comparison of decay components of 10^{-5} mol l^{-1} L-tryptophan in saline and pH 7 Aerosil 300 based sol-gel. Errors are quoted to 3 standard deviations.

The most noticeable variation is the longest decay component, which not only an increase in decay time, but also an increase in relative intensity. It is accepted that in zwitterion form, τ_3 is due to conformer B, as illustrated in Figure 2.13. However this is a higher energy conformation, as the negatively charged carboxyl group is close to the electron rich aromatic ring system and the positively charged amino group is further away. The silica network will be affecting the mobility of tryptophan in order for the longest component to be more easily resolved. The fluorescence rotational decay time of tryptophan in aqueous solution is 0.88 ns, but in sol-gel this decreases to 0.74 ns. This indicates a decrease in the microviscosity experienced by tryptophan but does not suggest it is bound to the surface of the silica pores.

The suitability of the sol-gel for biomolecule entrapment was also investigated. The fluorescence decay of a 2.5 mg/ml hexokinase in Aerosil 300 based sol-gel was

measured (Figure 4.3). Here, 600 µl of stock 10 mg/ml hexokinase from bakers yeast (10,000 units Sigma-Aldrich Co., Dorset) was added to 2.4 ml of phosphate buffered saline at pH 7.4. The experimental set up was as mentioned above.

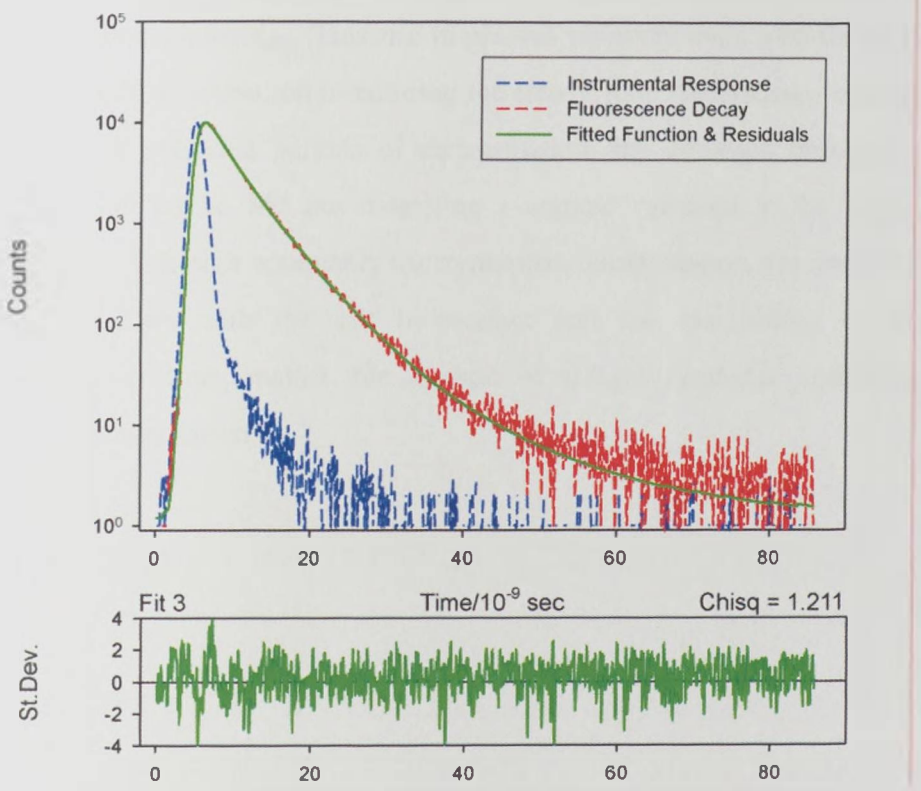

Figure 4.3

Fluorescence decay of 2.5 mg/ml hexokinase in Aerosil 300 based sol-gel.

Unfortunately, even after several attempts, the encapsulation of hexokinase in Aerosil 300 based sol-gel, prepared in the above method, was unsuccessful. The decay analysis yielded unexpected decay components of 2.43, 4.86 and 13.66 ns, vastly different from hexokinase in saline (c.f. Table 4.2). A similar result was seen for HSA encapsulated in an identically prepared Aerosil 300 sol-gel. Equation 4.2

shows that in this sol-gel process, considerable quantities of salt will be produced, which may be detrimental to bioactivity.

In addition, the long term pHs of the sol-gels were monitored. It was found that the pH of the gels tended to dramatically increase with time after t_{gel} indicating that neutralising the highly basic sodium silicate solution with acid will be successful only at times shortly after t_{gel}. This rise in pH was observed even with the inclusion of additional buffers. Also, on monitoring the steady state fluorescence emission of hexokinase over extended periods of encapsulation, the emission maximum red-shifted from 330 nm to 345 nm indicating a marked variation in the tryptophan conformations. Although acceptable for tryptophan encapsulation, the long term pH rise in conjunction with the salt by-product and the red-shifting of protein fluorescence over time, makes this method of sol-gel synthesis unsuitable for biomolecule encapsulation.

4.3 Synthesis from Inorganic Precursor

4.3.1 Background Chemistry

The work in this section is the acid catalysed hydrolysis of the inorganic precursor, tetramethoxysilane (TMOS) to produce the reactive silicic acid species. The initial reaction involving TMOS can be described by an electrophilic attack on the acid catalyst (represented by H^+) by oxygen in the methoxy group and a nucleophilic attack on the centre silicon atom by water creating a pentaco-ordinate silicon intermediate[134]. Methanol is a good leaving group, and is released from the centre silicon as shown in Figure 4.4.

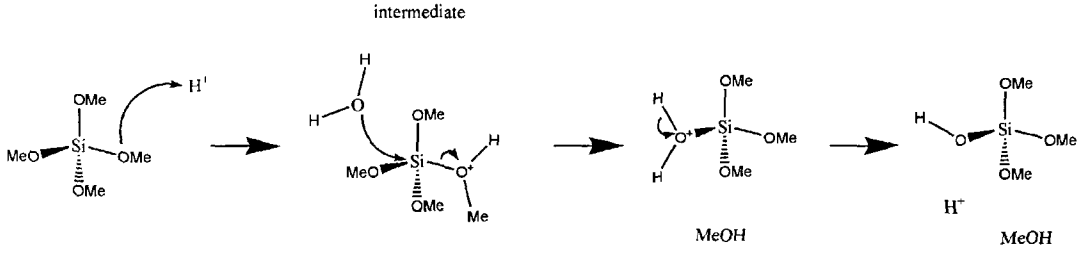

Figure 4.4
Initiating reaction of TMOS and water to produce silicic acid in the acid catalysed reaction. The curly arrows represent a movement of two electrons to form or break a chemical bond.

The overall reaction of TMOS with water to form silicic acid is shown below.

$$Si(OCH_3)_4 + 4H_2O \xrightarrow{H^+} Si(OH)_4 + 4CH_3OH \quad (4.2)$$

TMOS can also be base catalysed although this method was not used in this work. In this reaction, a nucleophilic attack on the centre silicon atom or methoxy carbon by hydroxide anions is most likely. It is also possible to initiate the reaction without any

catalyst and obtain a near neutral pH sol. In this case, a TMOS/water/methanol mixture is used. This reaction is however, also acid catalysed as methanol is a weak Brønsted acid. The uncatalysed reaction was not used in this work, despite the advantage of near neutral pH, as it is not possible to control the start of the reaction, nor is it possible to select the gelation point. Also, the reaction is carried out in methanol, an unsuitable solvent for proteins. The gelation point can be altered by varying the *R*-ratio, i.e. the molar ratio of water to silicon alkoxide.

4.3.2 Experimental

The first step in equation 4.2 shows that 4 moles of water are required to hydrolyse 1 mole of TMOS, i.e. the *R*-value is 4. In this work, small volumes of gel are produced, beginning with 4.5ml of TMOS (99.8%, Fluka, Dorset) similar to the work by Narang *et al*[135]. With this volume of TMOS, molar calculations conclude that 2.2 ml of water are required to guarantee full hydrolysis. To the mixture of TMOS and water, 0.1 ml of 0.1 mol l^{-1} hydrochloric acid (Volumetric Standard, Sigma-Aldrich, Dorset) is added and the mixture subjected to ultrasonic agitation (Ultrawave Model U400) for 10 minutes. Initially an emulsion is formed for a short time but further sonication ensures a clear homogeneous solution as the methanol is produced. This reaction is highly exothermic, therefore the water in the ultrasonic bath must be cool to allow adequate dissipation of heat from the mixture and prevent excessive evaporation of any material. The solution is then stored at 4°C to allow ample hydrolysis.

The low pH and lower temperatures slow down the condensation reaction, but will allow creation of small silica clusters in solution and will also maximise the removal of methoxy groups from the silicon centres. Storage of the solution for a period of 5 days at 4°C yielded the most transparent gels. Gelation of sols stored for a lesser period of time yielded gels that scattered more light indicating that longer chains of silica were formed.

Equation 4.2 indicates that methanol is produced as a by-product in this reaction. Since methanol is harmful to biologically active molecules this must be removed. Methanol was removed by rotary evaporation methods (J. Bibby Vacuum Rotary Evaporator Type 349/2) based on work by Ferrer *et al*[136]. A diagram of the rotary evaporation apparatus is shown in Figure 4.4.

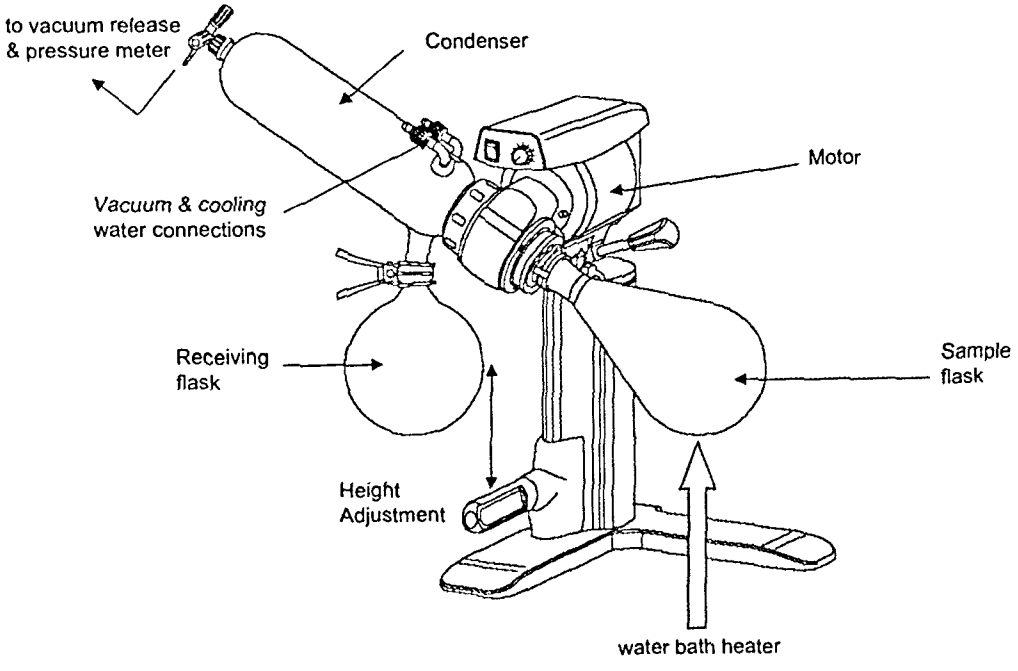

Figure 4.4

Diagram of basic rotary evaporator apparatus

The solution was added to the sample flask and slowly rotated in a water bath kept at 40°C and the methanol removed at a pressure of ~200 mbar. Using equation 4.2, molar calculations predict a volume of methanol of ~5 ml obtained if full hydrolysis has taken place. In reality, only around 40% of this was collected since a large proportion of the methanol in the solution will be lost to the vacuum and hydrolysis will take place after the gelation point.

At this stage, the treated solution is pH neutralised with buffers at 4°C and vigorous mixing to ensure no pH gradients. The selection of buffers was not trivial in this section of preparation. Simply neutralising the solution with phosphate buffered saline at pH 7.4 was not suitable as the buffer naturally attempts to remove the positive charges on the silica clusters induced by the acid and in turn produces gelation at an unworkably fast rate despite the lower temperature used. To provide neutralisation, pH neutrality after gelation and a workable gelation time, a 50% v/v phosphate and borate buffers at 4°C were used. Gelation time with this mixture of buffers was around 10 minutes and produced a sol-gel with the pH of the liquid in the pores of between pH 6 and pH 7, determined by universal indicator. Negligible auto fluorescence was detected from the gels when irradiated with light in the wavelength range 260 – 300 nm.

The gels can be aged and dried under ambient conditions and do not suffer from stress cracks or fractures. The gels are illustrated in Figure 4.5.

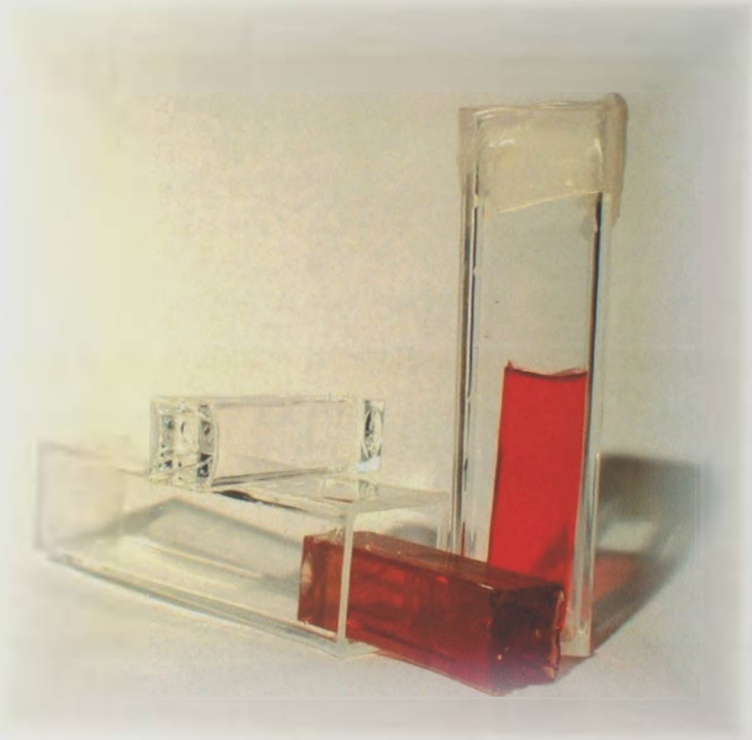

Figure 4.5
Illustration of TMOS based sol-gels aged and dried at ambient conditions. The use of coloured indicators are for illustrative purposes.

The gels in Figure 4.5 were prepared to a total volume of 3 ml and it can be seen that during ageing they have shrunk to around 50% of that volume. Although the entrapment of biomolecules requires hydrated sol-gels, and dried gels were not used in this work, the absence of stress fractures in dried gels prepared using this method may be useful in other applications such as coatings for metal implants[119].

Additives may be added to the sol-gel to further protect protein or enzyme biofunctionality. Nassif *et al* have demonstrated that living bacteria can remain active for up to 50% longer when protecting additives such as poly-ethylene glycol are included[91]. In making gels by the above method, it is preferable to add protecting additives such as poly-ethylene glycol or glycerol, before removal of methanol. The

addition of glycerol not only protects biomolecule activity, it results in a lower density, less shrinkage and fewer stress cracks[137].

4.3.3 Results with proteins

The biocompatibility of the sol-gels was ascertained by entrapment of the enzyme hexokinase, which is key to glucose metabolism and will be discussed in chapter 5. A stock solution was made by dissolving hexokinase from bakers yeast (10,000 units, Sigma-Aldrich, Dorset) in PBS buffer at pH 7.4 in a 10 mg/ml concentration. This stock solution was stored at −20°C until required. Hexokinase does not degrade upon repeated freeze-thaw cycles. A 600 µl volume of hexokinase stock solution was added to 2.4 ml of sol-gel mixture at pH 6, prepared as described, to produce a concentration of 2.5 mg/ml and a gelation time of around 10 minutes. The steady state emission spectra of free and 24 hour entrapped enzyme were compared using a Perkin-Elmer LS50B spectrofluorometer with its excitation monochromator tuned to 295 nm.

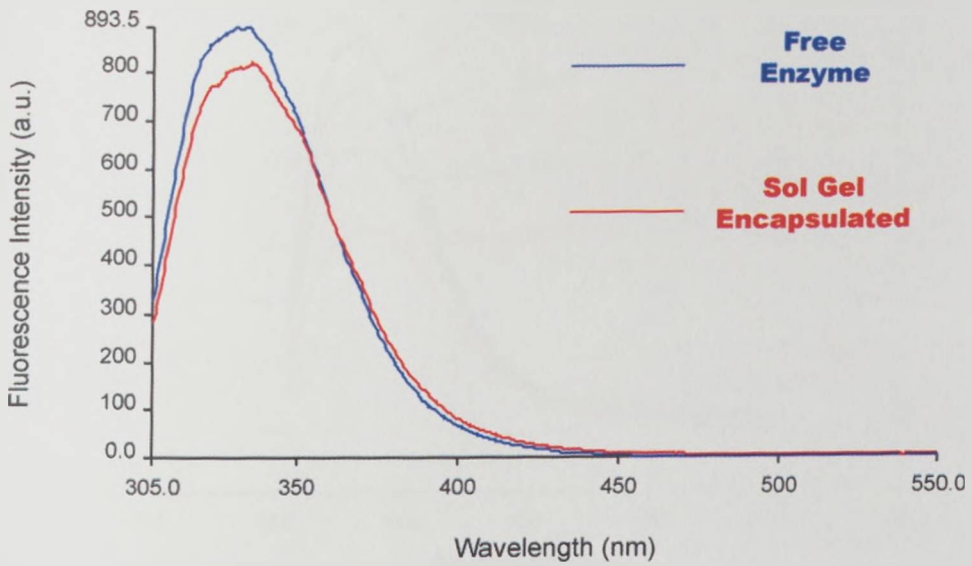

Figure 4.6

Steady state spectrum of 2.5 mg/ml hexokinase in buffer and encapsulated in a sol-gel matrix. λ_{ex} =295 nm.

The emission maximum of hexokinase in solution is 330 nm, and Figure 4.6 shows that the encapsulated enzyme emission maximum does not shift from this maximum. It can be concluded from the intrinsic tryptophan fluorescence, that the sol-gel does not have an effect on the structure of the protein, as a shift in the fluorescence maximum would indicate an alteration the tryptophan local environment. A drop in fluorescence is noted, although this is expected due to the porous nature of the medium. It can also be concluded that a sufficient quantity of methanol was removed from the sol prior to gelation as methanol affects the structure of hexokinase by inducing a red-shift in the tryptophan fluorescence. This phenomenon has been observed in previous studies[93].

The biocompatibility of the sol-gel was investigated over a number of days. Figure 4.7 shows the change in the fluorescence of a 2.5 mg/ml concentration of hexokinase in sol-gel from t_{gel} to t_{gel} +23 days.

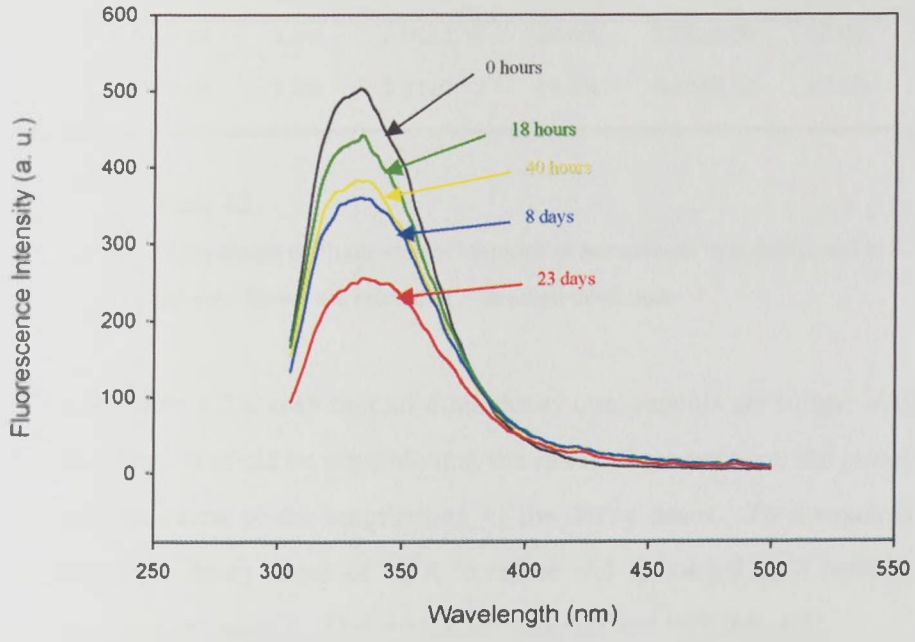

Figure 4.7

Variation in fluorescence intensity of hexokinase in sol-gel over time.

The lack of shifting in the fluorescence maximum and the similarity between the widths of the different spectra suggest that the protein is not noticeably denatured in the sol-gel even over extended periods of encapsulation. Since the polycondensation process continues long after t_{gel}, it can be concluded that the effects of incident light scattering may be the cause of the fluorescence intensity decrease. Another possible cause, is the hindered rotation of hexokinase by the sol-gel as shown in Table 4.4.

The fluorescence decay parameters of hexokinase in buffered saline the sol-gel were studied. Table 4.3 summarises the fluorescence decay times of a 2.5 mg/ml concentration of hexokinase in PBS and in sol-gel. The fluorescence decays were collected using the IBH 5000U fluorescence lifetime system with the 295 nm LED described in §3.3, and then fitted to a three-exponential model.

Media	τ_1 (ns)	Relative Intensity	τ_2 (ns)	Relative Intensity	τ_3 (ns)	Relative Intensity	χ^2
Saline	0.75±0.24	3.8%	3.00±0.15	59.8%	5.00±0.09	36.6%	0.998
Sol-gel	1.00±0.24	5.2%	3.51±0.13	67.5%	6.28±0.12	27.3%	0.990

Table 4.2
Comparison of fluorescence lifetimes of hexokinase in solution and in sol-gel. Errors are quoted to 3 standard deviations.

The data in Table 4.2 shows that all three decay components are longer in the sol-gel than in solution. It could be possible that the interactions between the protein and the sol-gel are the cause of the lengthening of the decay times. To investigate further, the fluorescence decay times of HSA in saline and in sol-gel, at a concentration of 2.5 mg/ml, were measured. The results are summarised in Table 4.3.

Media	τ_1 (ns)	Relative Intensity	τ_2 (ns)	Relative Intensity	τ_3 (ns)	Relative Intensity	χ^2
Saline	0.55±0.05	4.5%	3.24±0.23	33.8%	6.65±0.05	61.6%	1.01
Sol-gel	0.59±0.06	9%	2.47±0.19	36%	6.04±0.05	55%	1.08

Table 4.3

Comparison of decay times of HSA in solution and in sol-gel. Errors are quoted to 3 standard deviations.

It is clear from the HSA decay time comparisons that the sol-gel does not necessarily increase the decay times of tryptophan residues in proteins. It is difficult to draw any conclusions from this information as hexokinase contains four tryptophan residues, making its kinetics more complicated than those of single tryptophan residue HSA.

Further investigation was carried out by measuring the rotational decay times of hexokinase in solution and making a comparison to those of the sol-gel entrapped protein. Figures 4.8 and 4.9 show the anisotropy decays with fitted model. These figures illustrate the presence of two rotational decay times with the short rotational decay attributable to the tryptophan local motion and the long component attributable to the Brownian rotation.

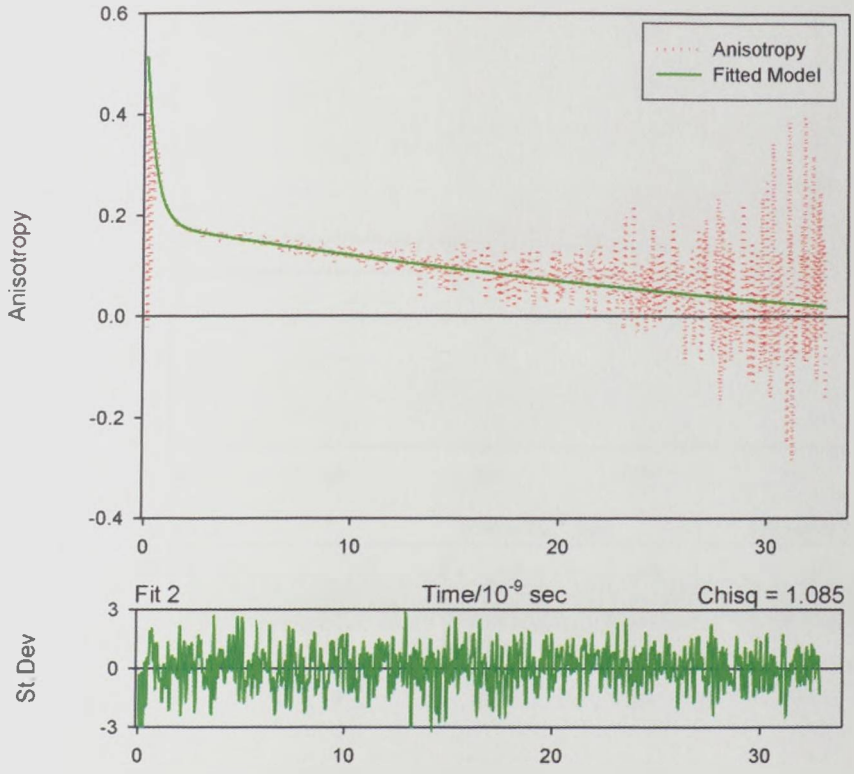

Figure 4.8

Anisotropy decay of hexokinase in saline (2.5 mg/ml).

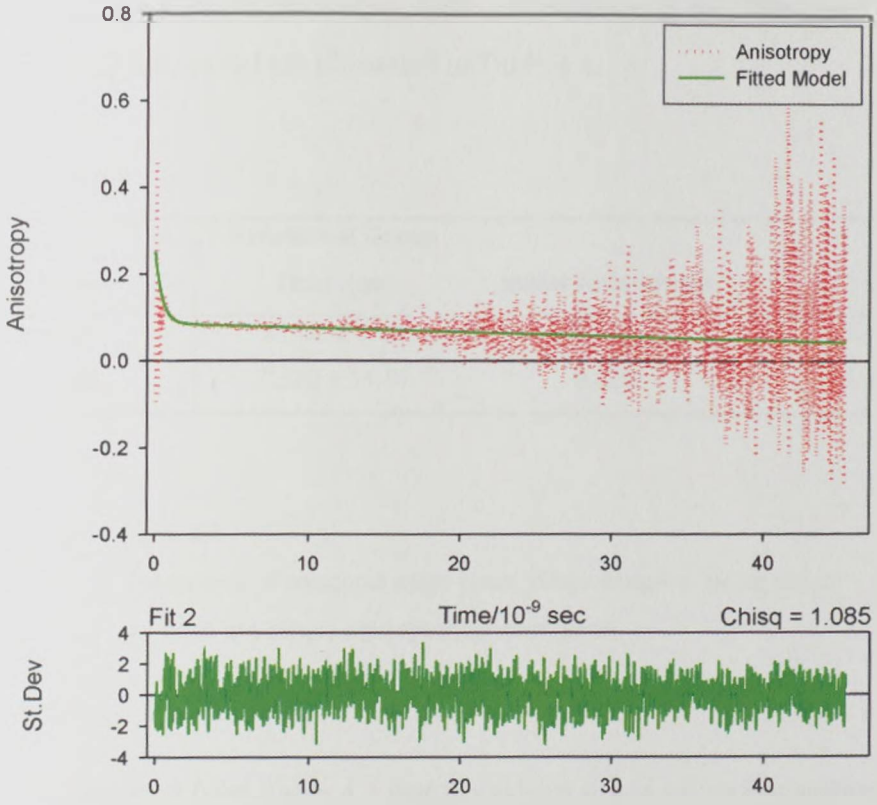

Figure 4.9

Anisotropy decay of hexokinase in sol-gel (2.5 mg/ml).

Both Figure 4.8 and 4.9 illustrate a two rotational decay for hexokinase, constituting the tryptophan local motion and the overall Brownian rotation as expected. However it was not possible to provide an adequate fit to the anisotropy decay for hexokinase in sol-gel using a two component model. Using this model yielded a tryptophan local motion that was unphysically fast. The data could however, be fitted to the simple rigid spherical rotor model (see equation 2.29). However, the kidney shaped hexokinase molecule (see §5.1) gives rise to uneven dimensions and cannot be approximated to a sphere (unlike conA and, to a lesser extent, aTf). Therefore a model accounting for the differing motions and diffusion co-efficients in each spatial dimension should be used[13]. Nonetheless, the model can be used to illustrate the variations in microviscosity between saline and sol-gel. One should note however,

that the rotational decay times cannot be used to obtain molecular volumes. A comparison of the rotational decay times of hexokinase in saline and in sol-gel obtained using this model are illustrated in Table 4.4.

Media	Rotational Decay Time (ns)	Initial Anisotropy	χ^2
saline	21.82 ± 1.14	0.176	1.042
sol-gel	72.20 ± 11.57	0.087	1.078

Table 4.4

Comparison of rotational decay times of hexokinase in saline and sol-gel fitted to a simple rigid spherical rotor model.

It can be concluded from Table 4.4 that the sol-gel described in this section severely hinders the rotation of entrapped proteins. The longer rotational decay time indicates that the sol-gel microenvironment is over three times more viscous than that of saline. The lower initial anisotropy indicates at the possibility of the protein being bound to the surface of the sol-gel pores, rather than being allowed to freely rotate in the water within the pores.

4.3.4 Characterisation

The sol-gels produced by the above method were investigated to determine the quantity of methanol, if any, in the pores and to ensure all of the TMOS was consumed in the hydrolysis reaction. To achieve this, the distillate from the rotary evaporator and the sol-gel itself was studied using ^{1}H nuclear magnetic resonance (NMR). ^{1}H NMR is particularly useful in the investigation of other products produced along with silica, as the silica itself will not be probed since it contains no hydrogen atoms.

NMR is one of the most powerful structural and spectroscopic methods available to researchers, with its wide and diverse range of methods and applications. NMR has been used in the investigation of the reaction kinetics of sol-gels for some time[127]. The property of a nucleus known as its spin is the basis of nuclear magnetic resonance spectroscopy[138]. Every isotope of every element has a ground state nuclear spin quantum number, I, which will have a value $n/2$ where n is an integer. Isotopes with even atomic number and even atomic mass have $I = 0$ and therefore have no NMR spectra. In this work the isotope ^{1}H was used, with a spin quantum number of $I = ½$. When I is non-zero, the nucleus has a magnetic moment, μ, defined by

$$\mu = \gamma\hbar\left[I(I+1)\right]^{1/2} \tag{4.3}$$

where γ is the magnetogyric ratio, a constant characteristic of a particular isotope. In the case of ^{1}H, the magnetogyric ratio is 2.675×10^8 rad T^{-1} s^{-1}. In the presence of a strong magnetic field, the spin axis orientation is quantised with magnetic quantum number m. Irradiation at an appropriate radio frequency causes transitions in the spin axis orientation, with selection rule $\Delta m = -1$, and it is these that are observed in NMR spectroscopy. The chemical shift of a nucleus is the difference between the

resonance frequency (ν) of the nucleus and a standard, relative to the standard (usually tetramethyl silane $Si(CH_3)_4$). This quantity is reported in parts per million (ppm) and given the symbol delta, δ.

$$\delta = \frac{(\nu - \nu_{REF}) \times 10^6}{\nu_{REF}} \tag{4.4}$$

Figure 4.10 illustrates the ^1H NMR spectrum of the distillate obtained from rotary evaporation of the sol at low pH. The ^1H NMR measurement was carried out on a Bruker Avance 400 9.6 T NMR spectrometer operating at 400 MHz, with a typical signal-to-noise ratio of 140:1 for a ^1H multiplet. The measurement was carried out in a 507-PP Wilmad NMR tube with the sample dissolved in deuterated chloroform in a concentration of 10 mmol l^{-1}, and filled to a sample depth of 4 cm in the tube.

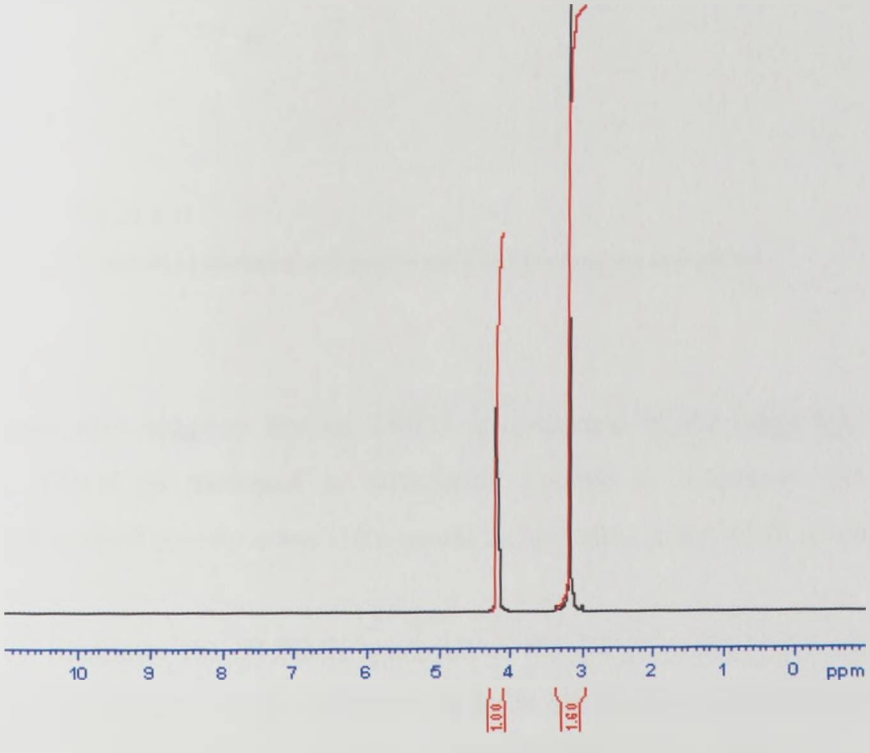

Figure 4.10

^1H NMR spectrum of distillate from sol in deuterated chloroform ($CDCl_3$) at 400 MHz.

The spectrum illustrates two resonances at δ – 3.1 and 4.2 ppm with relative intensities of 1.6:1. These shifts are indicative of the sole presence of methanol, although relative intensities of 3:1 would be expected due to the three equivalent protons from the methyl group and the one proton from the hydroxyl group. However, this can be explained by the acidic nature of the initial sol, where it is expected that some aqueous acid (H_3O^+) is transferred with the methanol in the distillation, and the methanol can be protonated[139] represented by the equilibrium in Figure 4.11.

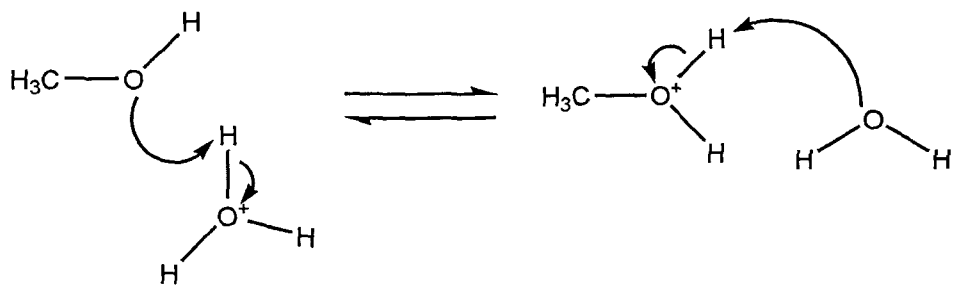

Figure 4.11

Reaction of methanol and acid in the distillate from the low pH sol.

The spectrum also suggests that all TMOS is consumed in the initial hydrolysis reaction. TMOS in methanol is sufficiently volatile to evaporate under the conditions described above, so any trace would be identified in the NMR spectrum.

Figure 4.11 illustrates the ^1H NMR spectrum of the sol-gel, carried out using the same equipment as above. The ungelated sol-gel at low pH was diluted in D_2O to a concentration of 10 mmol l^{-1} and added to the NMR tube as described.

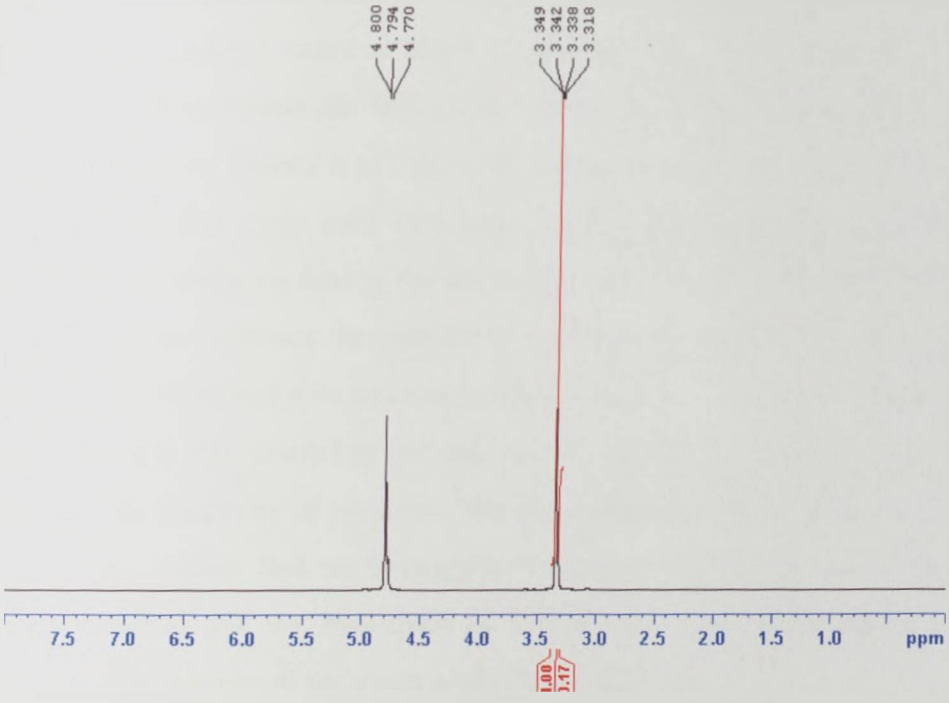

Figure 4.11

^{1}H NMR spectrum of ungelated sol-gel in deuterated water (D_2O) at 400 MHz, after rotary evaporation treatment.

The prominent resonance at δ – 4.8 ppm is characteristic of water and is expected due to the highly aqueous nature of the sol-gel synthesis. The resonance at δ – 3.3 ppm is likely to be $-CH_3$ groups from methanol, either left over from the distillation, from further hydrolysis or bound to the silica surface. The presence of methanol can be considered very small, due to the absence of the –OH resonance at δ – 4.2 ppm. However, D – H exchange between the D_2O solvent and the hydroxyl group of methanol will also contribute to the absence of the resonance at δ – 4.2 ppm.

4.4 Remarks

This chapter has demonstrated that of the powder and inorganic precursor sol-gel synthesis methods, sol-gel matrices based on the precursor TMOS are the most effective method of encapsulating biologically active molecules with no noticeable effect on their activity. Indeed it has been shown that whole *Escherichia Coli* cells are well preserved, and retain their enzymatic activity when entrapped in sol-gels prepared by a very similar method to the one used in this work[140]. The TMOS based gels can be treated to overcome the problem of methanol by-product and the pH can be neutralised and stabilised over extended periods of time. It appears that the salt production and the pH instability of the powder synthesis method used was detrimental to the bioactivity of proteins. The characterisation of the TMOS sol-gel and the distillate indicate that no measurable methanol and TMOS remain in the matrix demonstrating that the hydrolysis of TMOS was total and complete, and demonstrating effectiveness of the rotary evaporation methods.

The behaviour of proteins in the TMOS based sol-gel environment is difficult to understand. Using fluorescence decay times alone provides little information on the environment, however the rotational times from the fluorescence anisotropy give an interesting insight. It would appear that the protein has its movement restricted and is either bound to the surface of the sol-gel pores or hindered by high microviscosity in the pores. This theory can be supported by work by Gottfried *et al* on the encapsulation of a substituted myoglobin in TMOS based sol-gels, where they report the hindered rotation of the encapsulated molecule[141]. Brennan and co-workers also report on a similar phenomenon with Rhodamine 6G in aqueous sol-gels[142]. However, Brennan and co-workers also report on sugar modified sol-gel matrices that can discourage the binding of the fluorophore to the pore surface[143], a possible solution to hindered rotation.

5

Glucose Sensing

5.1 Clinical Outline

Sensors have played an important role in many industries providing the mechanical vision used for counting, sorting, reading and robotic guidance. Many sensor technologies used in industry can be applied in medicine. Sensors will be unlikely to have a transforming effect on health care in the short term, but it is a realistic goal within 10 years[144]. Work in this chapter is concerned with research into eventual fabrication of a device for *in vivo* measurement of glucose, based on fluorescence spectroscopy. One of the main reasons for developing these devices is the detection of hypoglycemia in people with insulin dependent, or type 1 diabetes. Self-monitoring of glucose concentrations with finger-prick samples of capillary blood is an integral part of modern management of diabetes. A painless, non-invasive technique would enormously increase patients' compliance with management and, if the technique was continuous, would allow detection of hypoglycemia or hyperglycaemia[145]. An audible alarm for this would be of great importance during the night as glucose levels can go undetected for many hours. The Diabetes Control and Complications Trial Group demonstrated the importance of tight control of glucose concentrations by way of a computer simulation. The group estimate an additional 5 years of life, 8 years of sight, 6 years free from kidney disease and 6 years free from amputations for a diabetic following tight control versus the standard regimen[146]. The enormous potential healthcare benefits of non-invasive monitoring have stimulated considerable research and development efforts. The notion of an *in vivo* glucose sensor coupled to a portable insulin infusion pump to create an artificial endocrine pancreas controlled by feedback is the ultimate goal. However, such a

system will require many years of "open loop" testing to ensure totally reliable glucose sensing, a stage far out of reach at this time[147].

At this time there are a number of commercially available *in vivo* glucose sensors available making use of different technologies. These devices can already detect hypo- and hyperglycemia, a benefit missed by previous technologies[148]. Due to some remaining problems with these first generation systems, further research has been carried out to explore alternative glucose monitoring techniques. The technique of interest in this work is the fluorescence spectroscopy approach. Work by the Photophysics Group at Strathclyde University and Guy's Hospital in London has demonstrated the use of a fluorescence resonance energy transfer (FRET) based assay for glucose, where concanavalin A is labeled with the infrared fluorescent protein allophycocyanin, and dextran labeled with the fluorescent dye malachite green[149]. Also investigated by the Photophysics Group and Guy's Hospital is the monitoring of fluorescence from fluorescent nicotinamide adenine dinucleotide phosphate NAD(P)H from the non-fluorescent oxidised form, NAD(P), by measuring the fluorescence from skin[150,151]. Fluorescence from NAD(P)H has also been studied by Piston and Knobel using two-photon excitation microscopy[152]. Other techniques used for monitoring glucose concentrations are numerous and include the use of modified carbon electrodes[153], near infrared spectroscopy[154,155], long wavelength dyes[156], bacterial glucose-binding proteins[157-159], boronic acid derivatives[160] and glucose oxidase[161].

Work in this section concerns a simpler measuring strategy whereby the intrinsic fluorescence of the enzyme hexokinase is monitored on addition of glucose. This approach has been investigated by Hussain *et al* using fluorescence intensity measurements[93]. This work will further investigate the hexokinase system using fluorescence decays. Fluorescence decays offer advantages over fluorescence intensities as they are independent of fluorophore concentration, easy to discriminate against artefacts and simple to calibrate.

5.2 Hexokinase Structure and Function

Yeast hexokinase (ATP:D-hexose-6-phosphotransferase) belongs to a class of enzymes (EC 2.7.1.1) which catalyse the transfer of phosphate from adenine triphosphate (ATP) to an acceptor. In the hexokinase reaction (with Mg^{2+} co-factor), the γ-phosphoryl group of ATP is transferred to the hydroxyl group at the C6 position of glucose.

$$D-glucose + ATP^{4-} \xrightarrow{\text{Hexokinase, } Mg^{2+}} D-glucose-6-phosphate^{2-} + ADP^{3-} + H^{+} \quad (5.1)$$

The hexokinase reaction is central to the metabolism of glucose since formation of glucose-6-phosphate makes glucose available for glycolysis and for the synthesis of polysaccharides.

There are two known isoenzymes of yeast hexokinase, type A or P-I, and type B or P-II, with an overall homology in their amino acid sequence of about 75%[162,163]. The P-II isoenzyme is the most predominant form in the participation of the catabolism of glucose. At physiological pHs, native yeast hexokinase mostly exists as a homodimer which has a molecular weight of 104 kDa.[164] Upon an increase in pH or ionic strength, the dimer will dissociate into two identical 52 kDa polypeptide chains, or monomers[165,166]. Each monomer consists of 461 amino acids folded into unequal domains. The large and small domains are separated by a cleft, which represents the glucose binding site. Hexokinase P-II consists of 14 α-helices and 13 β-strands and resembles a kidney with approximate dimensions 59×78×54 $Å^3$, determined from high resolution crystal structure analysis[167]. Figure 5.1 illustrates the secondary structure in open conformation.

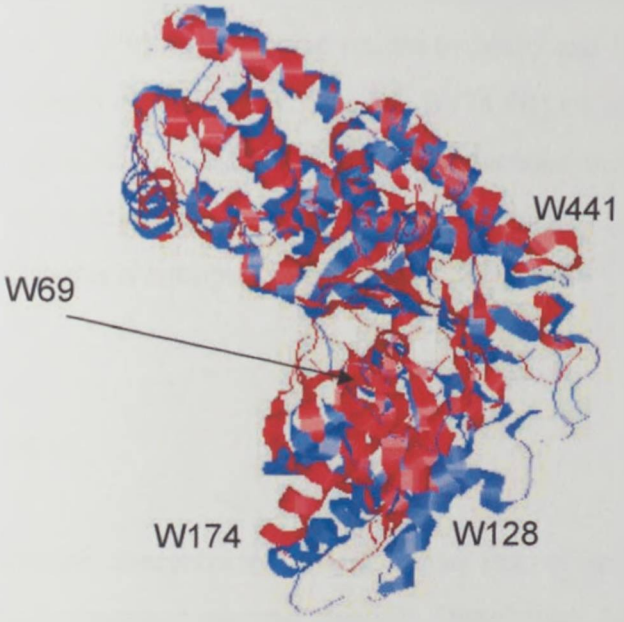

Figure 5.1

Structure of hexokinase molecule in open conformation showing tryptophan locations. The active site is located between the two domains. Structure from The Protein Data Bank[88].

The hexokinase subunit contains four tryptophan residues at amino acid positions W69, W128, W174 and W441. With extensive titrations of the quenching of tryptophan fluorescence in hexokinase, Kramp and Feldman classify the four tryptophan residues as: 1. a highly accessible surface tryptophan (W441), 2. a surface tryptophan with restricted accessibility (W128), 3. a glucose-quenchable cleft tryptophan (W174) and 4. a "buried" tryptophan (W69) in the hydrophobic interior[168]. The percentages of the total emission attributable to the individual tryptophans are 9, 22, 28 and 41% respectively. Binding of glucose to the hexokinase causes a 12° rotation of one lobe of the enzyme relative to the other[169]

resulting in a movement of up to 9 Å in combination of with a closure of the cleft where glucose is bound[170]. With this conformational change, a quenching of tryptophan fluorescence occurs[171] by the alteration of the microenvironment of tryptophan residues[172]. Further quenching studies by Maity and Jarori suggest that it is the microenvironment of residues W69 and/or W174 that are altered as a result of glucose induced quenching[173]. Although there is a decrease in the configurational entropy due to the binding, the binding-induced increase in hydrational entropy prevails, thus the process is entropically favourable[174].

5.3 Enzyme Kinetics

The effect of substrate concentration on the initial rate of an enzyme-catalysed reaction is a central concept in enzyme kinetics. Hexokinase, like many enzymes does not exhibit linear trends of initial rate, v, against substrate concentration [S]. Rather it exhibits a rectangular hyperbolic type curve. It was these observations that, in 1913, lead Leonor Michaelis and Maud Menten to derive an algebraic equation, known as the Michaelis-Menten equation[175]. The Michaelis-Menten equation can be derived by considering the following generalised scheme for an enzyme-catalysed production of a product P from substrate S. The enzyme must first form an intermediate complex with the substrate (ES) before product is produced.

$$E + S \underset{k_{-1}}{\overset{k_1}{\rightleftharpoons}} ES \xrightarrow{k_2} E + P \qquad (5.2)$$

Here k_1, k_{-1} and k_2 are the rate constants for the association of substrate and enzyme, the dissociation of unaltered substrate from the enzyme and the dissociation of product from the enzyme, respectively. The overall rate of reaction, v, is limited by

step k_2 and by the concentration of substrate bound enzyme, [ES] and can be written as

$$v = k_2[\mathrm{ES}] \tag{5.3}$$

At this stage, two assumptions have been made. The first is the availability of a vast excess of substrate so that [S] >>[E]. The second is that the complex ES is formed and broken down at the same rate so that the concentration of ES is constant, i.e. the system is in catalytic steady-state. The rate equations can then be expressed as follows:

$$k_1[\mathrm{E}][\mathrm{S}] = k_{-1}[\mathrm{ES}] + k_2[\mathrm{ES}] \tag{5.4}$$

By re-arranging the rate constants, equation 5.4 can be re-written as:

$$\frac{[\mathrm{E}][\mathrm{S}]}{K_\mathrm{M}} = [\mathrm{ES}] \tag{5.5}$$

where K_M is defined as the Michaelis Constant and is given by:

$$K_\mathrm{M} = \frac{k_{-1} + k_2}{k_1} \tag{5.6}$$

The total quantity of enzyme in a system, E_0 must be equal throughout an experiment, either existing as free or bound enzyme such that:

$$[\mathrm{E}_0] = [\mathrm{E}] + [\mathrm{ES}] \tag{5.7}$$

Using equation 5.7, equation 5.5 can be rearranged in several steps to give:

$$[ES] = \frac{[E_0][S]}{[S] + K_M} \tag{5.8}$$

Now substituting the right hand side of equation 5.8 into equation 5.3 in place of [ES] gives

$$v = k_2 \frac{[E_0][S]}{[S] + K_M} \tag{5.9}$$

The maximum rate of reaction, v_{max}, would be achieved when all enzyme molecules have substrate bound to them. Under the conditions where $[S] >> [E]$ it is fair to assume that all enzyme will be in bound form such that $[E_0] = [ES]$. Once again, returning to equation 5.3, substituting v_{max} for v and $[E_0]$ for [ES], the following can be written

$$v_{max} = k_2[E_0] \tag{5.10}$$

Now combining equation 5.10 with equation 5.9, a final equation can be written

$$v = \frac{v_{max}[S]}{[S] + K_M} \tag{5.11}$$

This is the Michaelis-Menten equation. If we consider this equation when the rate is at half maximum, it illustrates that in fact the K_M of an enzyme is the substrate concentration at which the reaction will occur at half maximum rate. It also shows that the lower the value of K_M, the stronger affinity an enzyme will have for a given substrate. The value of K_M can be extracted from equation 5.11 by plotting the reciprocal of the reaction rate against the reciprocal of substrate concentration. This Lineweaver-Burke (or double-reciprocal plot) yields a straight line with equation

$$\frac{1}{v} = \frac{K_M}{v_{max}} \frac{1}{[S]} + \frac{1}{v_{max}} \qquad (5.12)$$

giving the gradient of the plot equal to K_M/v_{max} and the y-intercept as $1/v_{max}$.

5.4 Fluorescence Response of Hexokinase to Glucose

The fluorescence response of hexokinase to increasing glucose concentrations was measured by monitoring the variations in the fluorescence intensity (§5.4.1), fluorescence decays (§5.4.2), fluorescence anisotropy (§5.4.3) and steady state emission of a complex with the visible dye Nile Red (§5.4.4).

5.4.1 Fluorescence Intensity

Initially the fluorescence intensity as a function of glucose concentration was measured using the Perkin Elmer LS50B spectrophotometer as in previous studies[93]. A 3 ml solution of hexokinase from bakers yeast (10,000 units, Sigma-Aldrich Co.

Ltd, Dorset) was prepared in a concentration of 2.5 mg/ml in phosphate buffered saline (Oxoid Ltd.) at pH 7.4. Glucose (99.9%, Sigma-Aldrich Co. Ltd., Dorset) was dissolved in PBS at pH 7.4 to a concentration of 0.1 mol l^{-1}, and was added to the hexokinase solution in 3 µl increments to provide an increase in glucose concentration in the system of 0.1 mmol l^{-1} per increment. The glucose concentration was varied from 0.1 to 1 mmol l^{-1}. Fluorescence measurements were carried out in 4 × 1 × cm quartz type fluorometric cells.

The fluorescence intensity with increasing glucose concentration is displayed in Figure 5.2.

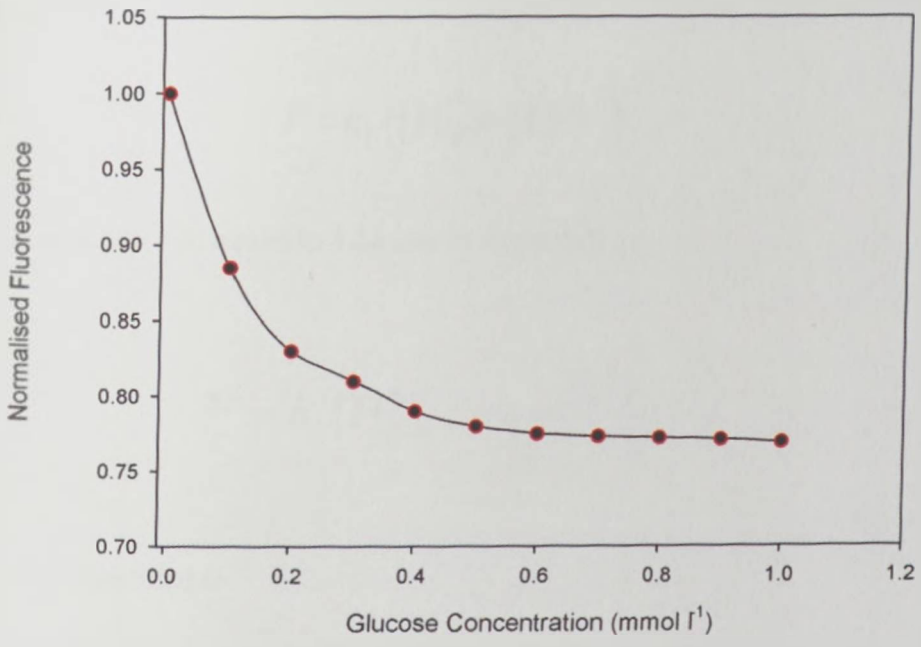

Figure 5.2
Variation in fluorescence intensity with increasing glucose concentrations.

It can be seen from Figure 5.2 that the fluorescence intensity decreases by ~23% at a glucose concentration of 1 mmol l^{-1}, consistent with previous studies[93]. No further change in the fluorescence is detected at glucose concentrations above 1 mmol l^{-1}.

A simple mathematical expression can be derived from the normal fluorescence rate equation to explain the decrease in fluorescence. The fluorescence F from free hexokinase can be given by:

$$F = k_F[H^*] \tag{5.13}$$

where [H*] represents the concentration of excited free hexokinase molecules. By considering equation 5.7 which states that the total concentration of enzyme is equal to the sum of the concentrations of free and bound enzyme, equation 5.13 can be written as

$$F = k_F\left([H_0^*] - [HG^*]\right) \tag{5.14}$$

By using equation 5.8, equation 5.14 can be expressed as

$$F = k_F[H_0^*]\left(1 - \frac{[G]}{[G] + K_M}\right) \tag{5.15}$$

This can be simplified to

$$F = (1 - s)k_F[H_0^*] \tag{5.16}$$

where s is a dimensionless co-efficient that is dependent on the binding strength of the enzyme for its substrate (K_M) and the concentration of the substrate in the solution. Here s must fall within the range

$$0 \geq s \geq \frac{[G]_{max}}{[G]_{max} + K_M} \tag{5.17}$$

where $[G]_{max}$ is the maximum glucose concentration that hexokinase will respond to (for hexokinase, this will be 1 mmol l^{-1}). The term $k_F[H_0^*]$ in equation 5.16 represents the fluorescence from hexokinase with zero glucose concentration. Strictly speaking however, equation 5.16 describes the decrease in fluorescence from free hexokinase only. Since bound hexokinase emits at the same wavelength, we will see the total fluorescence from free and bound hexokinase.

This total fluorescence F_T can be given by the following equation

$$F_T = (1-s)k_{FH}[H_0^*] + sk_{FHG}[H_0^*] \tag{5.18}$$

where k_{FH} is the rate of fluorescence from free hexokinase and k_{FHG} is the rate of fluorescence from glucose bound hexokinase. The above equation provides a trend in fluorescence intensity against glucose concentration very similar to that obtained from experiment if k_{FHG} is taken to be ~75% of k_{FH}. A comparison is shown in Figure 5.3.

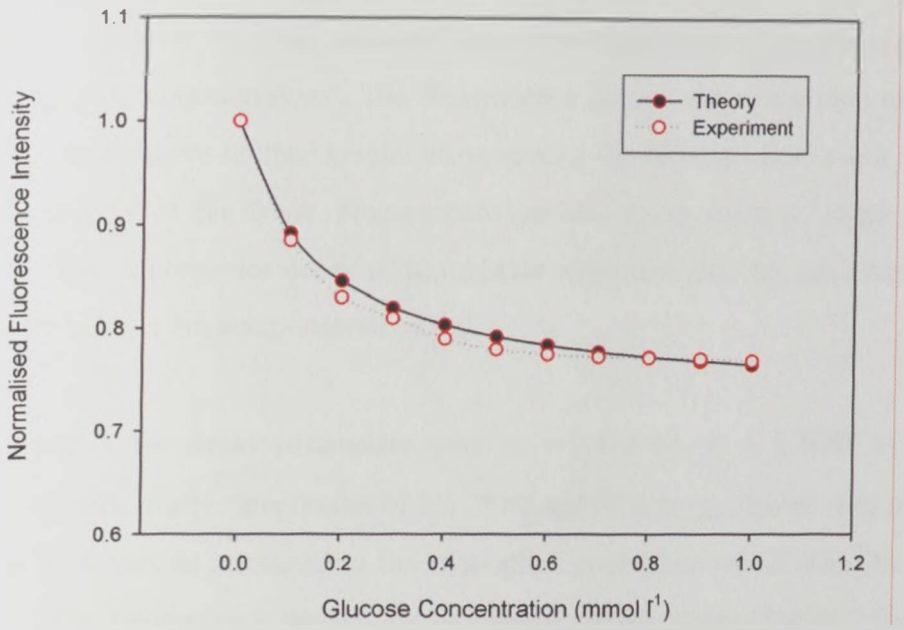

Figure 5.3

Comparison of fluorescence intensity against glucose concentration as obtained by experiment and by equation 5.18.

Figure 5.3 illustrates the same trend from experiment and from theoretical calculations. However, the data points obtained from experiment appear to drop slightly sharper than that of those obtained form equation 5.18. For equation 5.18, K_M was set to the accepted value of 0.15 mmol l^{-1}. The experimental data yielded a K_M of 0.11 mmol l^{-1} indicating that the binding of glucose is stronger. However, caution should be exercised when using fluorescence intensity data alone, as fluorescence intensity data is susceptible to bleaching effects, instrumental effects, etc.

5.4.2 Fluorescence Decay

This section discusses the time-resolved fluorescence response of hexokinase to increasing glucose concentrations. The fluorescence decays were measured on the IBH 5000U fluorescence lifetime system incorporating the 295 nm LED as described in previous sections of this thesis. Fluorescence was selected by using a 310 nm high pass filter. The fluorescence decay of hexokinase with zero glucose concentration was analysed using a three-exponential model.

As in Chapter 3, the decay parameters were $\tau_1 = 0.514$ ns, $\tau_2 = 2.1084$ ns and $\tau_3 = 5.037$ ns with relative amplitudes of 3%, 59% and 38% respectively. The triple component fit is can be attributed to the tryptophan conformer model described in chapter 2. The fluorescence decays for increasing glucose concentration may be fitted to a three exponential model with all three decay components variable in the fitting. However, with all components variable in the fitting algorithm, useless "curve fitting" is sometimes the best that can be obtained[176]. Many decay curves can be analysed with three components irrespective of whether their values have any physical meaning. For this reason, the analysis can sometimes be simplified by fixing one or more of the decay parameters if they are well known[11]. Table 5.1 illustrates the decay parameters obtained from a three-exponential model where all parameters are freely variable in the fitting algorithm and this shows that it is difficult to extract significant trends from any of the parameters.

[Glucose] mmol l^{-1}	τ_1 (ns)	Fractional Int. f_1	τ_2 (ns)	Fractional Int. f_2	τ_3 (ns)	Fractional Int. f_3	χ^2
0.0	0.51±0.14	2.99%	2.98±0.13	58.60%	5.04±0.07	38.51%	0.948
0.1	0.55±0.12	5.33%	2.95±0.16	49.37%	4.87±0.07	45.30%	1.007
0.2	0.60±0.07	6.12%	2.79±0.26	46.48%	4.86±0.08	47.40%	0.985
0.3	0.62±0.07	7.12%	2.98±0.26	48.32%	4.91±0.07	44.57%	0.948
0.4	0.63±0.06	7.50%	2.99±0.24	49.75%	4.98±0.07	42.75%	0.978
0.5	0.65±0.07	7.80%	2.91±0.30	45.90%	4.90±0.07	46.31%	1.003
0.6	0.54±0.06	6.75%	2.64±0.23	42.105%	4.79±0.06	50.30%	0.974
0.7	0.59±0.06	7.62%	2.74±0.29	44.36%	4.83±0.06	48.02%	0.951
0.8	0.54±0.06	7.21%	2.64±0.25	42.09%	4.82±0.05	50.69%	0.939
0.9	0.66±0.06	8.88%	2.92±0.26	48.67%	4.97±0.07	42.46%	0.965
1.0	0.61±0.06	8.11%	2.77±0.30	43.69%	4.83±0.06	48.20%	0.975

Table 5.1

Decay parameters for increasing glucose concentration, obtained from a three-exponential model with all parameters variable. Errors are quoted to 3 standard deviations.

In proteins, tryptophan will be bonded into the polypeptide chain as illustrated in the following schematic diagram:

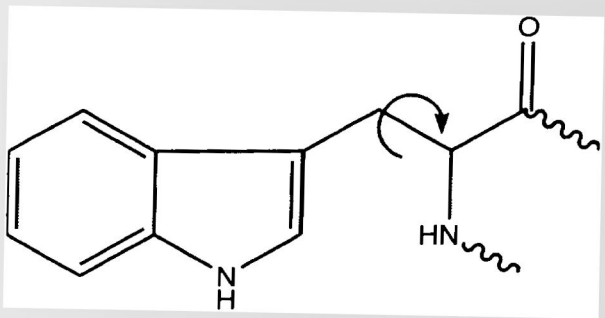

Figure 5.4

Representation of tryptophan in a polypeptide chain. The wavy lines represent the covalent bonds to the previous and next amino acid in the sequence.

Although tryptophan will be included in a polypeptide chain, and free rotation about the C_α-C_β bond may not be possible, the three conformers (Figure 2.13) will still be present by way of different fixed orientations of the indole ring system around the C_α-C_β bond illustrated in Figure 5.3. In the tryptophan conformer model, the decay component τ_2 (~3 ns) is attributed to the decay from the indole ring system. In subsequent analysis of hexokinase fluorescence decays with increasing glucose concentration, the decay component τ_2 will be fixed at the value obtained for zero glucose concentration, shown in Table 2. In doing so, the assumption that the indole ring systems will be unaffected by the presence of glucose, or by the conformational change of hexokinase, is made. Allowing components τ_1 and τ_3 to remain variable allows for changes in the orientation of the indole ring system of some tryptophan residues as hexokinase undergoes its conformational change.

The results of the analysis are illustrated in Table 5.2.

[Glucose] mmol l⁻¹	τ_1 (ns)	Fractional Intensity, f_1	Fractional Intensity, f_2	τ_3 (ns)	Fractional Intensity, f_3	χ^2
0.0	0.51±0.14	2.99%	58.60%	5.04±0.07	38.51%	0.948
0.1	0.61±0.08	5.73%	54.44%	5.01±0.08	39.63%	0.975
0.2	0.68±0.07	7.12%	52.70%	5.02±0.08	40.18%	0.958
0.3	0.66±0.06	7.60%	52.09%	5.02±0.08	40.31%	0.911
0.4	0.66±0.06	8.03%	52.10%	5.08±0.08	39.01%	0.979
0.5	0.71±0.06	8.80%	51.14%	5.04±0.08	40.07%	0.986
0.6	0.64±0.06	8.40%	53.48%	5.08±0.09	38.12%	0.961
0.7	0.66±0.06	8.77%	52.16%	5.05±0.08	39.08%	0.975
0.8	0.65±0.05	8.92%	52.42%	5.11±0.08	38.68%	0.987
0.9	0.68±0.06	9.21%	50.73%	5.04±0.08	40.06%	0.921
1.0	0.67±0.06	9.16%	50.66%	5.02±0.08	40.18%	0.995

Table 5.2

Decay components and relative amplitudes obtained from hexokinase with increasing glucose concentrations, and τ_2 fixed at zero glucose concentration value (2.98 ns). Errors are quoted to 3 standard deviations.

It can be seen that only the fractional intensities f_1 and f_2 and the decay component τ_1 have any significant variation with increasing glucose concentrations. The decay component τ_3 and fractional intensity f_3 remain significantly unaltered for all glucose concentrations. Due to the lack of variation in decay time and fractional amplitude of the third component, the analysis was carried out again with both τ_2 and τ_3 fixed at the values obtained for zero glucose concentration to further increase stability in the results. Table 5.3 illustrates the values obtained with these constraints in place.

[Glucose] mmol l⁻¹	τ_1 (ns)	Fractional Intensity, f_1	Fractional Intensity, f_2	Fractional Intensity, f_3	χ^2
0.0	0.51 ± 0.14	2.20%	58.60%	38.51%	0.948
0.1	0.60 ± 0.06	5.81%	55.24%	38.95%	0.981
0.2	0.68 ± 0.07	7.05%	53.11%	39.84%	0.963
0.3	0.65 ± 0.06	7.49%	52.72%	39.79%	0.950
0.4	0.68 ± 0.05	8.22%	51.86%	39.92%	1.024
0.5	0.71 ± 0.06	8.84%	50.82%	40.34%	1.036
0.6	0.66 ± 0.05	8.64%	52.19%	39.18%	1.055
0.7	0.66 ± 0.05	8.80%	51.95%	29.25%	0.996
0.8	0.69 ± 0.05	9.25%	50.53%	40.22%	1.017
0.9	0.68 ± 0.05	9.25%	50.57%	40.18%	0.996
1.0	0.69 ± 0.05	9.09%	51.05%	39.86%	0.997

Table 5.3

Decay components and fractional amplitudes obtained from hexokinase with increasing glucose concentrations. Components τ_2 and τ_3 are fixed at zero glucose concentration values (2.98 ns and 5.04 ns respectively). Errors are quoted to 3 standard deviations.

Again, the fractional intensity f_3 remains significantly unaltered. If a fluorescence quenching operation is taking place as glucose binds to hexokinase, a decrease in the values of τ_1 would be expected in conjunction with the decrease in fluorescence intensity rather than an increase. However, the increase in fluorescence decay time

τ_1 can be explained by first considering the fluorescence quantum yield of the excited state of component 1 of hexokinase (ϕ_1).

$$\phi_1 = \frac{k_{F1}}{k_{F1} + k_{NR}} \tag{5.19}$$

where k_{F1} is the rate of fluorescence due to the excited state given by τ_1. Due to the presence of glucose in the hexokinase solution, the technical quantum yield Φ_1 is given by

$$\begin{aligned} \Phi_1 &= \frac{k_{F1}}{(1-s)k_{F1} + k_{NR}} \\ &= \frac{k_{F1}}{k_{F1} - sk_{F1} + k_{NR}} \end{aligned} \tag{5.20}$$

Here, the term $-sk_{F1}$ will cause the technical quantum yield to increase from the normal quantum efficiency with increasing concentrations of glucose (given by s). The technical quantum yield can be expressed in terms of the normal quantum efficiency[1] as follows:

$$\begin{aligned} \Phi_1 &= \frac{\phi_1}{1 - \tau_1 s k_{F1}} \\ &= \frac{\phi_1}{1 - s\phi_1} \end{aligned} \tag{5.21}$$

It should be noted that the technical quantum yield given above will be for the excited state given by component 1 only. The $(1-s)$ multiplier in equation 5.16 will

also alter the standard rate of depopulation of excited states equation (2.11). If equation 5.16 is included into equation 2.11, the equation for the rate of depopulation of excited states is modified to give

$$\frac{d[\mathrm{H}^*]_1}{dt} = -\left((1-s)k_{\mathrm{F1}} + k_{\mathrm{NR}}\right)[\mathrm{H}^*]_1 \tag{5.22}$$

This will give an instrumental response function $i(t)$ of

$$i(t) = k_{\mathrm{F1}} \exp\left(-t/\tau\right) \tag{5.23}$$

where τ can be considered as the technical fluorescence decay time for component 1 and is given by

$$\tau = \frac{1}{(1-s)k_{\mathrm{F}} + k_{\mathrm{NR}}} \tag{5.24}$$

It should be noted that equation 5.23 is only representative of the excited species represented by component τ_1. Equation 5.24 can also be written as[1]:

$$\tau = \frac{\tau_1}{1 - s\phi_1} \tag{5.25}$$

where τ_1 is the decay time for component 1 at glucose concentration equal to zero, and ϕ_1 is the fluorescence quantum efficiency of free hexokinase as given in equation 5.19. Equation 5.25 provides a means of predicting the technical fluorescence decay

time τ for increasing glucose concentrations (given by the term s). A comparison of the decay times obtained for component 1 from equation 5.25 and from experiment is shown in Figure 5.5.

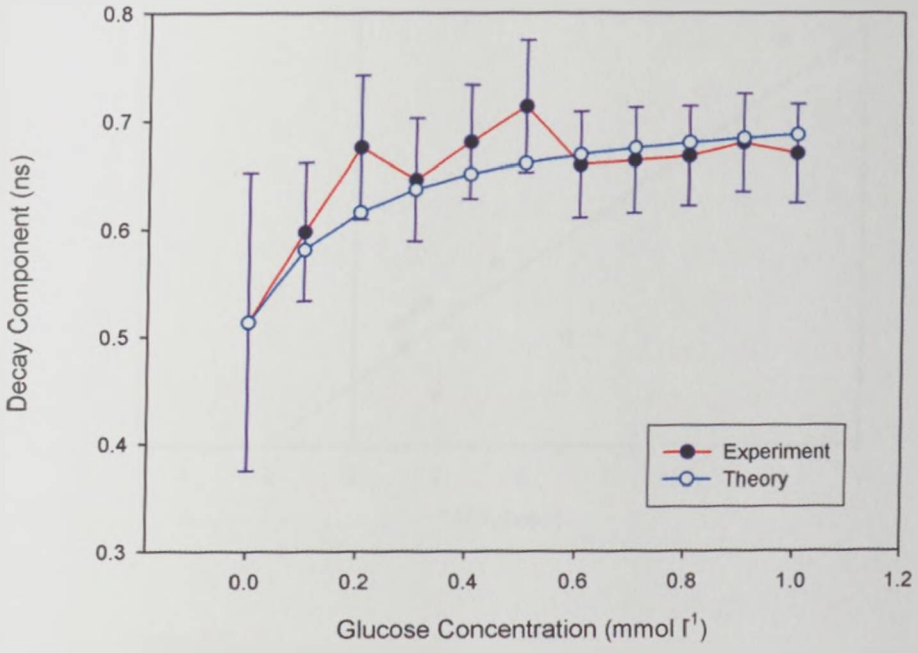

Figure 5.5

Variation of decay component τ_1 with increasing glucose concentrations from experiment and equation 5.25. For equation 5.25, ϕ_1 is assumed to be -0.3. Error bars are 3 standard deviations as given in Table 5.3.

Figure 5.5 illustrates the characteristic Michaelis-Menten trend in τ_1 with increasing glucose concentration and the similarity of theoretical values of τ_1 compared with those obtained from experiment, with all values within error.

The trend from Figure 5.5 can be analysed using the Lineweaver-Burke analysis as given by equation 5.12. Here, the reciprocal of the change in decay time is plotted against the reciprocal of glucose concentration (Figure 5.7).

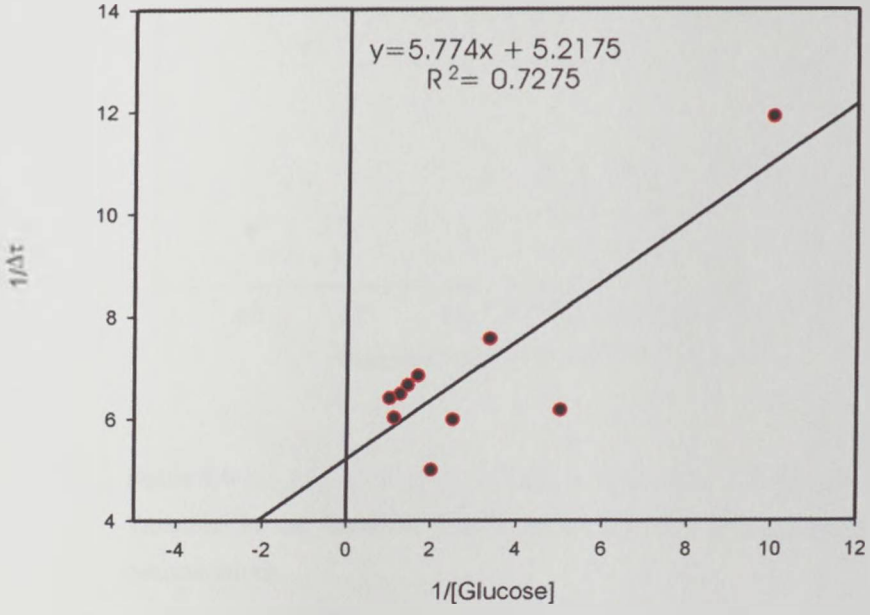

Figure 5.7

Double-reciprocal plot of change in decay component against glucose concentration. R^2 co-efficient of determination is shown.

The fitting of the straight line in Figure 5.7 yields a value of K_M =0.111 mmol l^{-1}. However, although this value is close to the accepted value, a R^2 value of 0.7275 indicates a poor straight line fit and thus the value obtained for K_M cannot be fully trusted. This is due to the significant errors on the values of τ_1 as shown in Figure 5.5 and the very small change in the decay time (<0.2 ns). However, the fractional amplitude of decay component 1 (f_1), follows the same trend as the fluorescence intensity and the decay time (Figure 5.8) with a more significant change.

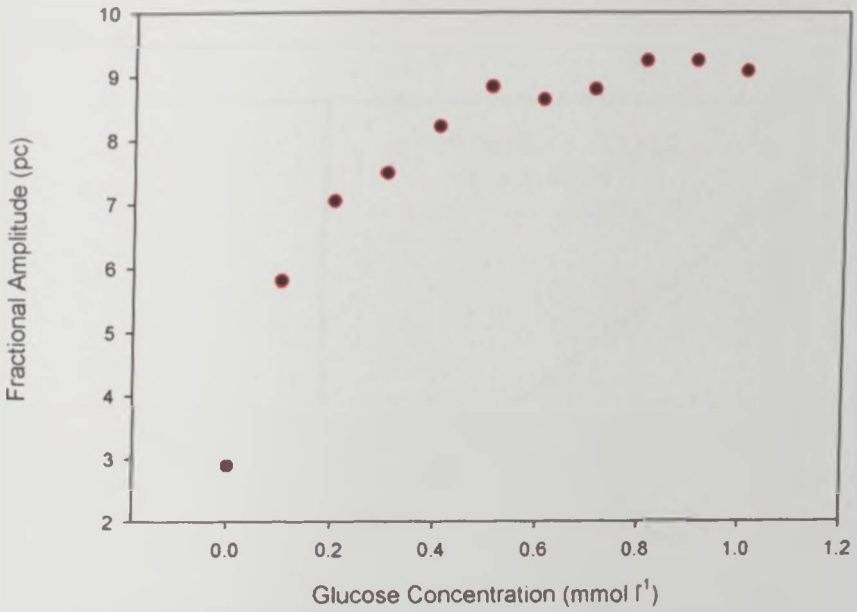

Figure 5.8
Variation in the fractional amplitude (f_1) with increasing glucose concentrations.

Figure 5.8 shows that the variation of the fractional amplitude produces a more stable trend than that of the decay time. The fractional amplitude is related to the decay time as follows[9]

$$f_i = \frac{B_i \tau_i}{\sum_j B_j \tau_j} \tag{5.27}$$

where B is the pre-exponential factor in the fitting model. It should be noted that the values for B_1 with increasing glucose concentration also increase with the same trend as f_1. Since f is related to τ by equation 5.27, a value for K_M should be obtainable by

plotting the reciprocal of f_1 against the reciprocal of glucose concentration. Figure 5.9 illustrates the double reciprocal plot.

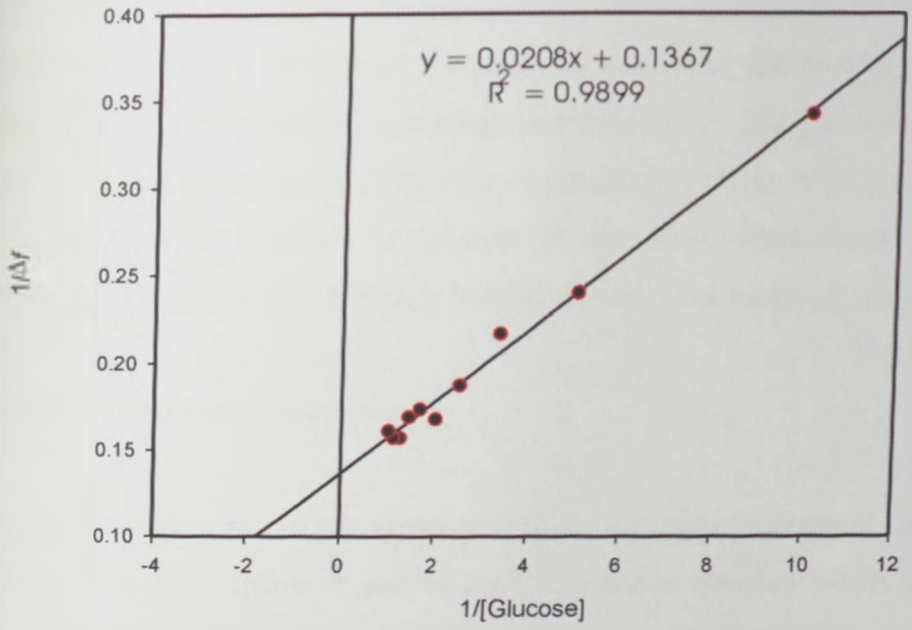

Figure 5.9

Double reciprocal plot of the change in fractional intensity against glucose concentration. R^2 co-efficient of determination is shown.

The analysis shown in Figure 5.9 yields a value of $K_M = 0.152$ mmol l^{-1}, within an acceptable range and close to the accepted value. The R^2 co-efficient of determination indicates a greater quality fit to the data, and thus a more reliable value of K_M.

From the fluorescence decay data, if we are to accept the tryptophan conformer model for hexokinase, it can be concluded that it is the component representing the conformer for which the NH group is closest to the indole ring that is increasingly altered as the interactions with glucose become more frequent. It would also appear that the change in the microenvironment experienced by tryptophan has bearing on its conformational alignment, although, one must be aware that these results are for the average of 4 tryptophan residues, each with different contributions to the overall

fluorescence intensity. As mentioned above, only 1, or possibly 2 of the residues' microenvironment is affected by the overall conformational change of hexokinase. A major discovery of modeling the variation in fluorescence decays with increasing glucose concentration using a three-exponential model is that it may not be (or may not exclusively be) the process of fluorescence quenching that is taking place as glucose binds. If a collisional quenching operation takes place exclusively in a system, we would expect decay components to decrease with the same trend. As we view an increase in a single component of the fluorescence decay with the fluorescence intensity decrease, clearly another process must be taking place.

Possibilities for additional process are:

(i) Radiative Migration. In the Birks Radiative Migration description, there is a possibility of self-absorption of part of the fluorescence emission which competes with the escape of fluorescence emission[1]. Birks describes the probability of self-absorption of an emitted photon is a, and therefore the probability of photon escape is $(1-a)$. This can be considered similar to the $(1-s)$ term used above, as it can be used to illustrate an increase in fluorescence decay time. If radiative migration were taking place, the technical quantum yield of the whole system, Q_H, (not just that of the excited state given by component 1) could be expressed by[177]

$$\begin{aligned} Q_H &= \phi_H(1-s)[1+s\phi_H+s^2\phi_H^2+.....] \\ &= \frac{\phi_H(1-s)}{1-s\phi_H} \end{aligned} \tag{5.28}$$

where the successive terms in the series correspond to photon escape after 1, 2, ... emissions. It turns out that if ϕ_H is taken to be ~0.3, and using equation 5.28, the technical quantum yield for increasing glucose concentration has the same decreasing trend as that of the fluorescence intensity for increasing glucose

concentration. A possible explanation is that the fluorescence emission is absorbed in the protein structure as a whole to a greater degree as it changes in conformation. However this may not be the case, as two tryptophan residues would need to become closely aligned with each other and the distance change of 9 Å may not be sufficient for this to take place. It is also unlikely that emission photons would be absorbed in the water solvent.

(ii) Refractive Index Change. The Strickler-Berg equation shows that the fluorescence decay time is proportional to the square of the refractive index of the medium. As glucose is added to the system, the refractive index will be altered. However, if the refractive index was influencing the fluorescence, the intensity and decay time would both decrease. In this case they do not, so is therefore this is an unlikely scenario.

(iii) Intra-tryptophan energy transfer. It is entirely possible that energy may be transferred between tryptophan residues as the conformation of hexokinase is altered with the binding of glucose. With this process, a decrease in the quantum yield and the fluorescence decay time is expected. This is seen if a two-exponential model is used, where the short component decreases with increasing glucose concentration as has been shown by other groups[173]. However, a three-exponential model would be more representative as it is generally accepted that a three-exponential model is required to describe the photophysics of aqueous tryptophan molecules. As this model shows, a decay component increases as the total quantum yield decreases. Therefore, energy transfer is less likely.

5.4.2 Fluorescence Anisotropy

The results in this section focus on the possible variations in the rotational times of hexokinase upon increasing concentrations of glucose. It was reasoned that since hexokinase undergoes a conformational change upon interaction with glucose, there would be some variation in its anisotropy decay. Fluorescence anisotropy measurements were carried out on the IBH 5000U fluorescence lifetime system, set up in an optical geometry shown in Figure 2.4, incorporating the 295 nm light emitting diode. The data was analysed as described in §2.4.3.

Hexokinase exhibits two rotational parameters, attributable to the overall Brownian rotation and the tryptophan local motion. Table 5.4 illustrates the overall change in the rotational parameters between no glucose and maximum glucose concentration.

Concentration of Glucose	τ_{r1} (ns)	Relative Intensity	τ_{r2} (ns)	Relative Intensity	Initial Anisotropy	χ^2
0 mmol l^{-1}	1.59±0.18	0.32%	23.09±1.62	99.68%	0.179	1.022
1 mmol l^{-1}	0.59±0.33	0.57%	23.72±1.51	99.43%	0.192	1.003

Table 5.4

Rotational decay times of hexokinase with no glucose and maximum glucose concentration. Errors are quoted to three standard deviations.

Unexpectedly the addition of glucose had no noticeable affect on the overall Brownian rotation of hexokinase. It was envisaged that the conformational change would produce an effective reduction in the volume of the enzyme, and yield faster rotational times. However, the fluorescence anisotropy shows that the tryptophan local motion is vastly altered in the presence of glucose – a ~66% reduction in rotational decay time (Table 5.4). A change in rotational times of this magnitude suggests that the microenvironment of at least one tryptophan residue is substantially altered, a concept supported by previous work[171]. Another explanation for this decrease in rotational time is intra-tryptophan energy transfer, an explanation

suggested in the previous sub-section. It is also noted that the error on the short rotational decay time of hexokinase in the presence of maximum glucose concentration is larger than that of the shorter rotational decay time of that of hexokinase in the presence of zero glucose. The rotational decay time of 589 ps is very fast and is close to the pulse width of the 295 nm LED, making resolution of this component more demanding. With increasing the glucose concentration beyond 1 mmol l^{-1}, no further variation in the tryptophan local motion was observed, indicating that the microenvironment of tryptophan cannot be altered any further.

5.4.3 Nile Red Probe

The molecule Nile Red (Nile Blue A Oxazone) is a highly fluorescent laser dye with intense environment dependent fluorescence. The structure of Nile Red is shown in Figure 5.12.

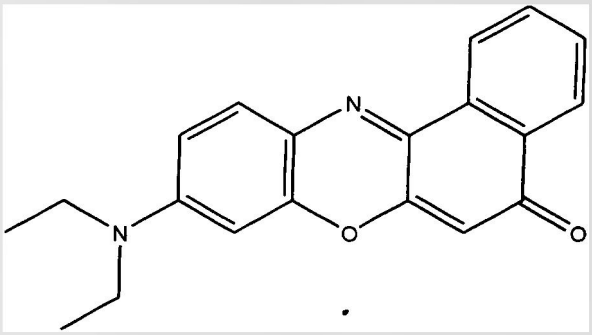

Figure 5.12
Structure of the Nile Red molecule

Nile Red is weakly soluble and exhibits almost negligible fluorescence in aqueous solutions, but is strongly fluorescent in organic solvents. It was reasoned that aqueous Nile Red would preferentially occupy the hydrophobic areas of hexokinase if added to an aqueous solution of hexokinase. The glucose induced conformational change should alter the fluorescence of the Nile Red. Indeed this approach has been used in previous studies to monitor the folding and unfolding pathways of human serum albumin[178].

Nile Red (99%, Sigma-Aldrich Ltd, Dorset) was dissolved in PBS at pH 7.4 with vigorous stirring and repeated ultrasonic agitation. Because of the relatively insoluble nature of Nile Red, much of the solid added to solution did not dissolve. For this reason the solution was vacuum filtered to remove undissolved solid. Fluorescence measurements were carried out on the Perkin-Elmer LS-50B fluorescence spectrophotometer with the excitation monochromator tuned to 530 nm, the absorption maximum of Nile Red in water. Around 20 minutes after the addition of 600 μl of hexokinase (10,000 units, Sigma-Aldrich Co., Dorset) of concentration 10 mg/ml, there was a ~25% increase in the fluorescence intensity from Nile Red, indicating that some of the molecule had occupied the hydrophobic area. Figure 5.13 illustrates the variation in the fluorescence intensity of Nile Red with increasing glucose concentrations. Also shown is a control experiment of aqueous Nile Red with no hexokinase present.

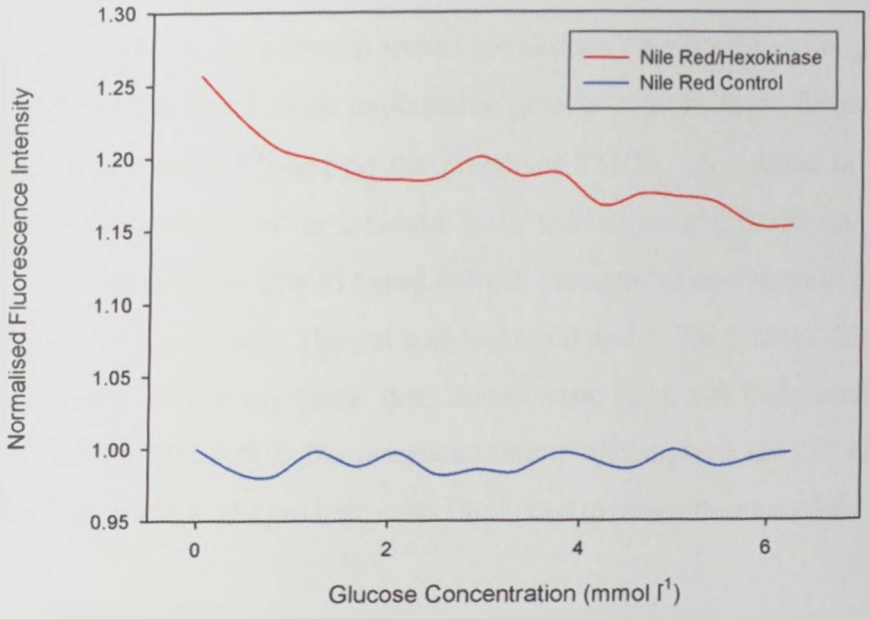

Figure 5.13

Variation in fluorescence intensity of Nile Red in hexokinase with increasing glucose concentrations. A Nile Red control is also shown. Fluorescence intensities are normalised to first free Nile Red measurement.

It can be seen that the fluorescence intensity falls rapidly as the glucose concentration approaches hexokinase's maximum of 1 mmol l^{-1}. With concentrations greater that 1 mmol l^{-1}, the fluorescence appears to fall further, indicating that further changes in the hydrophobic interior are taking place. The aqueous Nile Red control (shown in blue) indicates that the fall in fluorescence intensity is not due to the free Nile Red in water. However, the signal-to-noise ratio in this experiment is very poor due to the very weak fluorescence from aqueous Nile Red and the high excitation intensities required to excite the fluorescence.

5.5 Sol Gel Entrapment

This section discusses the potential use of hexokinase entrapped in a sol-gel derived matrix, as a possible route to an implantable glucose sensor. Here, hexokinase was encapsulated in a sol-gel based on the precursor TMOS. A volume of 600 µl of 10 mg/ml stock solution of hexokinase from bakers yeast (10,000 units, Sigma-Aldrich) was added to the TMOS based sol-gel, prepared as described in §4.2.3, to a concentration of 2.5 mg/ml. The gel was wet-aged at 4°C for 5 days. The samples were measured in 4 × 1 × 1 cm quartz type fluorometric cells, and fluorescence decays obtained with the IBH 5000U fluorescence lifetime system, with the 295 nm LED as excitation source and a 310 nm high-pass filter used to select fluorescence.

As seen in §4.2.3, hexokinase responds well to the sol-gel encapsulation, with no apparent denaturing or variation in conformation. However, it did appear that hexokinase did have its rotation severely hindered by the encapsulation. Here, the variation in the fluorescence decays with increasing glucose concentration to the sol-gel matrix will be monitored. As with §5.4.2, the decays will be analysed using three-exponential kinetics with the second component lifetime, τ_2, constrained at the value obtained for hexokinase in saline. Once again, in making this constraint, the assumption is being made that the indole ring systems of the tryptophan residues will be unaltered by the presence of glucose, the conformational changes induced by the binding of glucose, the hindered rotation of hexokinase in the sol-gel pores and the polar nature of the silicon-oxygen bonds in the matrix. This constraint has to be made, as although allowing all parameters free variation in the iteration program yields good fits, it is pure curve fitting and no useful information from the parameters was obtained. Figure 5.14 illustrates the fit of the fluorescence decay of hexokinase in sol-gel with τ_2 constrained at 2.11 ns. The near unity χ^2 goodness of fit shows that this model agrees well with the data.

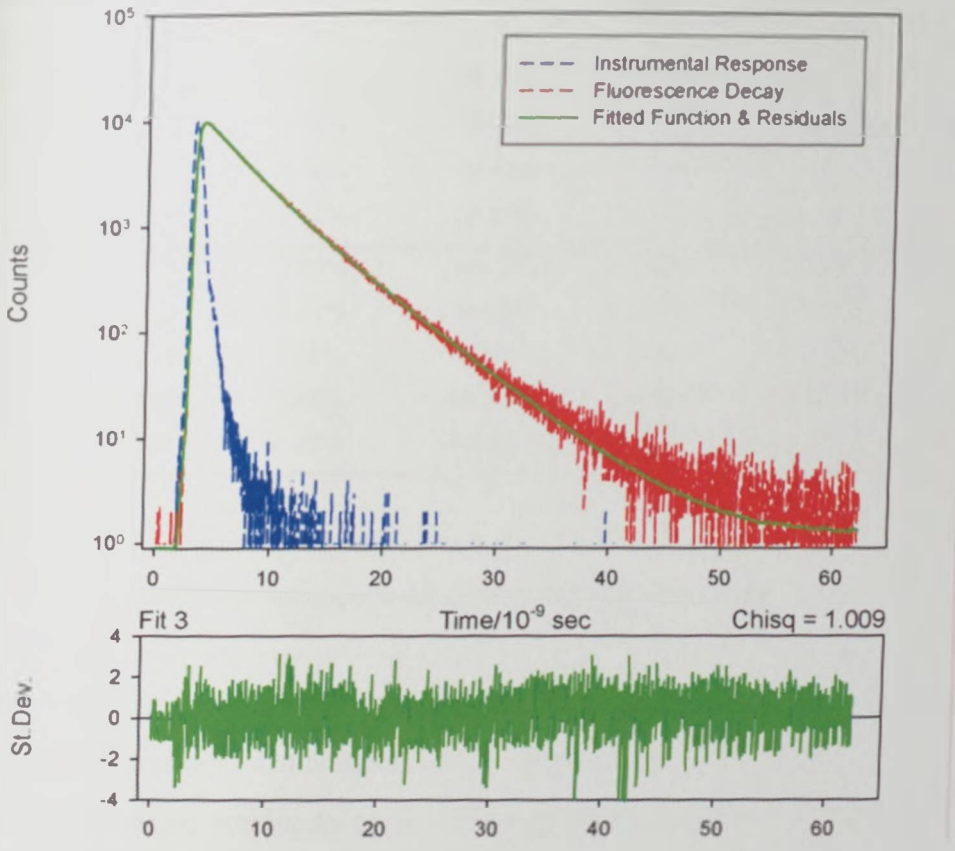

Figure 5.14

Fitted function to hexokinase in sol-gel fluorescence decay with τ_2 constrained.

With this model, the decay parameters are $\tau_1 = 0.603$ ns, $\tau_2 = 2.108$ ns and $\tau_3 = 5.545$ ns with relative intensities of 3%, 51% and 46% respectively. The decay times of τ_1 and τ_3, and all relative intensities are close to that of hexokinase in saline, indicating that the tryptophan conformations are relatively unaffected by the matrix. Table 5.5 illustrates the variation in the free parameters with varying concentrations of glucose. A time of 10 minutes was allowed between each addition of glucose to the sol-gel in an attempt to allow diffusion and eliminate concentration gradients.

[Glucose] mmol l^{-1}	τ_1 (ns)	Fractional Intensity, f_1	Fractional Intensity, f_2	τ_3 (ns)	Fractional Intensity, f_3	χ^2
0.0	0.60	2.27%	51.04%	5.55	41.70%	1.009
0.1	0.61	2.23%	52.73%	5.59	45.05%	1.076
0.2	0.74	2.10%	51.72%	5.54	45.36%	1.061
0.3	0.66	3.00%	52.73%	5.59	44.27%	1.042
0.4	0.68	3.10%	54.13%	5.70	42.78%	1.066
1.4	0.65	3.20%	53.12%	5.58	43.68%	1.055
2.4	0.62	3.07%	54.62%	5.69	42.32%	1.078
3.4	0.67	3.38%	54.43%	5.72	42.20%	0.972
4.4	0.74	3.83%	52.70%	5.64	43.47%	1.051
5.4	0.67	4.35%	52.03%	5.78	43.62%	1.106

Table 5.5

Variation in fluorescence decays with varying glucose concentration.

Table 5.5 shows only the component of the short decay changing with increasing glucose concentrations. On addition of 0.1 mmol l^{-1} increments, it appears that the increases in relative amplitude of τ_1 are much slower than that of hexokinase in saline. Increasing the increments to 1 mmol l^{-1} show that the sol-gel does limit the access of glucose to hexokinase by way of increased diffusion through the pores, since a larger increase in the relative amplitude of component τ_1 is not seen. Since glucose is added at the top of the cell and mixing is not possible, it will take a considerable length of time for the concentration gradient from top to bottom to equilibrate.

5.6 Remarks

In the analysis of hexokinase fluorescence decays, a three-exponential model assumes that the tryptophan conformer model can be applied. One must make certain assumptions before attempting analysis of hexokinase photophysics due to its complexity. Here, one cannot assign the three decay components to three discrete excited states of tryptophan residues in hexokinase. Other researchers have fitted the decay of hexokinase to a bi-exponential function. In using such a function here, an agreement in results is obtained. However, using impulse reconvolution methods, a third component is found, increasing in fractional intensity as the glucose concentration is increased.

Other models for the fluorescence decay can be invoked. Clearly, assigning a fluorescence decay component for each tryptophan residue as early literature suggests (chapter 2), is unacceptable as four distinguishable decay times would be present, and this is not seen here. One could take the view of thinking of hexokinase's four tryptophan residues each possessing three decay components, thus requiring a 12-exponential model for hexokinase. This is clearly excessive and would be unlikely to provide any physical information. Another possibility is to try an exponential model with more than three components with the addition of many constraints. This approach was investigated in this work, although it became clear that even increasing the number of components to four was an overparameterisation. Even if three out of four components are fixed, the fitting algorithm still cannot find a fourth component that can be easily interpreted as being physical.

The three-exponential model representative of the tryptophan conformer model proved successful if a constraint is placed on the component representing the fluorescence from the indole ring system. With this constraint, the variation in the relative intensity of the short component in the analysis could be used as a method for monitoring glucose concentrations. It also provides an insight into the

microenvironment of the tryptophan residues, suggesting that the conformers in which the amino group is closest to the aromatic ring system are significantly altered by the presence of glucose. However, one must be cautious when making any statements regarding the variations in tryptophan residue conformations upon conformational change of hexokinase. There are four tryptophan residues in hexokinase each with differing contributions to the overall fluorescence intensity. It is suspected that only one, or perhaps two, have their microenvironments altered by the glucose induced conformational change in hexokinase, thus the kinetics are more complicated than they appear.

Results from this chapter have indirectly suggested the possibility of a process other that fluorescence quenching taking place as glucose binds to hexokinase. Initial observations suggest that radiative migration or self-absorption of emission photons is the "most likely" process, although this would require further investigation. Due to the complexity of hexokinase photophysics and the additional complexity of the conformationally altered and unaltered hexokinase both emitting at 330 nm, it is possible that there are a number of processes taking place. If we are considering the technical quantum yield of decay component 1 in the model (equation 5.21), it increases with increasing glucose concentration thus to give rise to the increase in decay time. However, the technical quantum yield of the whole system (equation 5.28) decreases with increasing glucose concentration.

The methods of monitoring glucose concentration by fluorescence anisotropy and monitoring the fluorescence of Nile Red, can provide an interesting insight into the conformational changes taking place upon glucose binding, but they are unsuitable for glucose sensing. The fluorescence anisotropy approach illustrates a marked change in the tryptophan microenvironment when the glucose-induced conformational change of hexokinase takes place. However, fluorescence anisotropy measurements are relatively time consuming, even with modern excitation sources and are therefore not practical for *in vivo* sensing. Also, as with the three-

exponential model, it is an average of 4 tryptophan residues contributing to the overall time-resolved depolarisation seen, and two or possibly three residues may not have their microenvironments altered.

Fluorescence intensity studies of Nile Red suggest that it is capable of occupying the hydrophobic interior of hexokinase, demonstrated by a 25% increase in intensity when hexokinase is introduced. The variation in intensity with increasing glucose concentrations also illustrates that the hydrophobic interior is altered somewhat when the glucose induced conformational change takes place. This method is not suitable for glucose sensing due to the poor signal-to-noise ratio and the extremely weak Nile Red fluorescence. However, this system may warrant further investigation with more sophisticated incubation equipment, as it has been shown that Nile Red can be used to monitor conformational changes of HSA[178].

Encapsulation of hexokinase in a sol-gel derived matrix proved successful and the enzyme did respond to the presence of glucose. However, it would appear that the diffusion of glucose through the sol-gel was severely limited, suggested by the lower than expected response to higher glucose concentration increments. However, Hussain *et al* did report a higher K_M of hexokinase when entrapped in sol-gel when monitoring with fluorescence intensity[93], as a result of weaker binding caused by increased viscosity and slower diffusion. However, one should exercise caution when using fluorescence intensities, as they are not independent of scattered light and interferents, and could lead to distorted results. Although it has been reported that binding constants of enzymes can increase when encapsulated, it has also been reported that they can decrease when encapsulated[121].

In this work, it would appear that the process is diffusion limited by the sol-gel matrix. Here we cannot assume that the binding constant has increased, and we cannot rule out the possibility of large concentration gradients, since no change in the increase of amplitude f_1 was noted when increasing the glucose concentration

increments to from 0.1 to 1 mmol l^{-1}. It would appear that the volume of a 4 × 1 × 1 cm sol-gel matrix is too large to allow adequate equilibrium of concentration. Further investigation could be carried out using sol-gel thin films or spin coating. However this is not a trivial exercise. Preliminary investigation of spin coated thin films, prepared using the same synthesis method, revealed cracked sol-gels to the extent of forming fine powders.

Another explanation of the reduced response of hexokinase to glucose in the silica sol-gel matrix is the possibility that the whole protein could be bound in some way to the surface of the sol-gel pores, thus hindering its rotation. Although this hindered rotation does not have a detrimental effect on the nature of the enzyme, it may have a detrimental effect on its function, and this cannot be ruled out. As mentioned in chapter 4, this effect in sol-gels has been reported by Gottfried *et al*[141] in the case of proteins, and by Brennan & co-workers in the case of Rhodamine 6G[142]. This must also be investigated, perhaps by adopting the approach by Brennan and co-workers, by modifying the sol-gel pores with covalently bound sugars[143] in an attempt to prevent the molecule binding with the surface and hindering its rotation.

Although the methods presented in this work may not definitively describe the complex process of glucose binding to hexokinase, they could one day form part of a non or minimum invasion glucose sensor for diabetes based on fluorescence spectroscopy. Using hexokinase entrapped in a silica sol-gel is a promising route as the protein is not noticeably denatured, however the synthesis conditions of the sol-gel will need to be tuned to prevent hindered movement of the enzyme within the pores. The largest advancement has been in the use of the UV LEDs, which not only provide fluorescence decay data easily; they lend themselves to the optical "lab-on-a-chip" sensor which is so sought after. Such optical sensors are of particular interest as they are safe by being electrically isolated from the patient during *in vivo* studies and with fibre optic technology, can be easily miniaturised[179].

These techniques may be long awaited, and as noted by Hirsch, many patients and providers may be frustrated by the apparent lack of progress or continued delays. However, Hirsch also states that we should be aware of the fact that we are very fortunate to have the current technologies and therapies available to us, even when new technologies may be many further years in the making[180].

6

References

[1] J. B. Birks, *Photophysics of Aromatic Molecules*, (John Wiley & Sons Ltd., New York, 1970).

[2] P. Debye and J. O. Edwards, *Science*, **116**, (1952), 143.

[3] M. Lasagna, E. Gratton, D. M. Jameson, and J. E. Brunet, *Biophys. J.*, **76**, (1999), 443.

[4] T. R. Flotte, S. E. Beck, K. Chesnut, M. Potter, A. Poirier, and S. Zolotukhin, *Gene Therapy*, **5**, (1998), 166.

[5] M. Sato, T. Ozawa, K. Inukai, T. Asano, and Y. Umezawa, *Nature Biotechnol.*, **20**, (2002), 287.

[6] G. S. Waldo, B. M. Standish, J. Berendzen, and T. C. Terwilliger, *Nature Biotechnol.*, **17**, (1999), 691.

[7] A. Jablonski, *Z. Phys.*, **94**, (1935), 38.

[8] G. G. Stokes, *Phil. Trans. R. Soc. London*, **142**, (1852), 463.

[9] J. R. Lakowicz, *Principles of Fluorescence Spectroscopy*, 2nd ed., (Kluwer Academic/Plenum Publishers, New York, 2002).

[10] J. B. Birks, D. J. Dyson, and I. H. Munro, *Proc. Roy. Soc. A*, **275**, (1963), 575.

[11] D. J. S. Birch and R. E. Imhof, *Anal. Instrum.*, **14**, (1985), 293.

[12] Th. Förster, *Rad. Res. Suppl.*, **2**, (1960), 326.

[13] R. F. Steiner, Fluorescence Anisotropy: Theory and Applications, in *Topics In Fluorescence Spectroscopy, Volume 2: Principles*, edited by J. R. Lakowicz, (Plenum Press, New York, 1991), pp. 1-52.

[14] I. Munro, I. Pecht, and L. Stryer, *Proc. Nat. Acad. Sci. USA*, **76**, (1979), 56.

[15] D. J. S. Birch and C. D. Geddes, *Phys. Rev. E*, **62**, (2000), 2977.

[16] D. J. S. Birch and R. E. Imhof, Time-Domain Fluorescence Using Time-Correlated Single-Photon Counting, in *Topics in Fluorescence Spectroscopy, Volume 1: Techniques*, edited by J. R. Lakowicz, (Plenum Press, New York, 1991), pp. 1-95.

[17] L. M. Bollinger and G. E. Thomas, *Rev. Sci. Instrum.*, **32,** (1961), 1044.

[18] D. V. O'Connor and D. Phillips, *Time-correlated Single Photon Counting*, (Academic Press, London, 1984).

[19] A. Hallam and R. E. Imhof, *J. Phys. E: Sci. Instrum.*, **13,** (1980), 520.

[20] R. E. Imhof, *Fundamentals of Decay Curve Analysis*, 3rd ed., (IBH Consultants Ltd., Glasgow, 1989).

[21] C. D. McGuinness, K. Sagoo, D. McLoskey, and D. J. S. Birch, *Meas. Sci. Technol.*, **15,** (2004), L19.

[22] E. Cáceres, A. J. Goñi, and J. L. Alvarez Rivas, *J. Phys. E: Sci. Instrum.*, **7,** (1973), 178.

[23] D. J. S. Birch and R. E. Imhof, *Rev. Sci. Instrum.*, **52,** (1981), 1206.

[24] S. Goldberg and J. Rothstein, *Adv. Electron El. Phys.*, **14,** (1961), 207.

[25] C., *J. Franklin Inst.*, **215,** (1933), 225.

[26] N. A. Campbell, *Biology*, 4th ed., (The Benjamin/Cummings Publishing Co. Inc., California, 1996).

[27] C. Branden and J. Tooze, *Introduction to Protein Structure*, 2nd ed., (Garland Publishing, New York, 1999).

[28] The L- and D- nomenclature is defined by drawing the amino acid with the carboxyl group at the top and the variable R group at the bottom. If the amine group is on the left, it is the L-form, if it is on the right, it is the D-form.

[29] A. S. Sato, T. L. Religa, V. Daggett, and A. R. Fersht, *Proc. Nat. Acad. Sci. USA*, **101,** (2004), 6952.

[30] T. L. Religa, J. S. Markson, U. Mayor, S. M. V. Freund, and A. R. Fersht, *Nature*, **437,** (2005), 1053.

[31] A. V. Finkelstein and O. V. Galzitskaya, *Physics of Life Reviews*, **1,** (2004), 23.

[32] A. Tramontano, *Physics of Life Reviews*, **1,** (2004), 103.

[33] L. Pauling and R. B. Corey, *J. Am. Chem. Soc.*, **72,** (1950), 5349.

[34] L. Pauling and R. B. Corey, *Proc. Nat. Acad. Sci. USA*, **37,** (1951), 235.

[35] L. Pauling and R. B. Corey, *Proc. Nat. Acad. Sci. USA*, **37,** (1951), 241.

[36] L. Pauling and R. B. Corey, *Proc. Nat. Acad. Sci. USA*, **37,** (1951), 251.

[37] L. Pauling and R. B. Corey, *Proc. Nat. Acad. Sci. USA*, **37,** (1951), 256.

[38] L. Pauling and R. B. Corey, *Proc. Nat. Acad. Sci. USA*, **37,** (1951), 261.

[39] L. Pauling and R. B. Corey, *Proc. Nat. Acad. Sci. USA*, **37,** (1951), 272.

[40] L. Pauling and R. B. Corey, *Proc. Nat. Acad. Sci. USA*, **37,** (1951), 282.

[41] L. Pauling and R. B. Corey, *Proc. Nat. Acad. Sci. USA*, **37,** (1951), 235.

[42] B. Valuer, *Molecular Fluorescence: Principles and Applications*, (WILEY-VCH Verlag GmbH, Weinheim, 2002).

[43] A. S. Ladokhin, Fluorescence Spectroscopy in Peptide and Protein Analysis, in *Encyclopedia of Analytical Chemistry*, edited by R. A. Meyers, (John Wiley & Sons Ltd, Chichester, 2000), pp. 5762-5779.

[44] P. Y. Bruice, *Organic Chemistry*, 2nd ed., (Prentice-Hall Inc., New Jersey, 1998).

[45] M. Friedman and J. -L. Cuq, *J. Agric. Food Chem.*, **36,** (1988), 1079.

[46] E. A. Permyakov, *Luminescent Spectroscopy of Proteins*, (CRC Press, Boca Raton, FL, 1993).

[47] W. B. De Lauder and Ph. Wahl, *Biochem.*, **9,** (1970), 2750.

[48] D. Creed, *Photochem. Photobiol.*, **39,** (1984), 537.

[49] D. M. Rayner and A. G. Szabo, *Can. J. Chem.*, **56,** (1978), 743.

[50] A. G. Szabo and D. M. Rayner, *J. Am. Chem. Soc.*, **102,** (1980), 554.

[51] J. W. Petrich, M. C. Chang, D. B. McDonald, and G. R. Flemming, *J. Am. Chem. Soc.*, **105,** (1983), 3824.

[52] R. A. Engh, L. X. Q. Chen, and G. R. Flemming, *Chem. Phys. Lett.*, **126,** (1986), 365.

[53] D. M. Davis, D. McLoskey, D. J. S. Birch, P. R. Gellert, R. S. Kittlety, and R. M. Swart, *Biophys. Chem.*, **60,** (1996), 63.

[54] Z. Bajzer and F. G. Prendergast, *Biophys. J.*, **65,** (1993), 2313.

[55] F. R. Beierlein, O. G. Othersen, H. Lanig, S. Schneider, and T. Clark, *J. Am. Chem. Soc.*, **128,** (2006), 5142.

[56] R. E. Richards and N. A. Thomas, *J. Chem. Soc., Perkin Trans. 2*, **3,** (1974), 368.

[57] W. J. Colucci, L. Tilstra, M. C. Sattler, F. R. Fronczek, and M. D. Barkley, *J. Am. Chem. Soc.*, **112,** (1990), 9182.

[58] M. Van Gilst and B. S. Hudson, *Biophys. Chem.*, **63,** (1996), 17.

[59] P. E. Czabotar, S. R. Martin, and A. J. Hay, *Virus Res.*, **99,** (2004), 57.

[60] T. Araki and H. Misawa, *Rev. Sci. Instrum.*, **66,** (1995), 5469.

[61] T. Araki, Y. Fujisawa, and M. Hashimoto, *Rev. Sci. Instrum.*, **68,** (1997), 1365.

[62] M. L. Chithambo and R. B. Galloway, *Meas. Sci. Technol.*, **11,** (2000), 418.

[63] H. Szmacinski and Q. Chang, *Appl. Spectrosc.*, **54,** (2000), 106.

[64] W. J. O'Hagan, M. McKenna, D. C. Sherrington, O. J. Rolinski, and D. J. S. Birch, *Meas. Sci. Technol.*, **13,** (2002), 84.

[65] A. Yasan, R. McClintock, K. Mayes, S. R. Darvish, P. Kung, and M. Razeghi, *Appl. Phys. Lett.*, **81,** (2002), 801.

[66] A. Yasan, R. McClintock, K. Mayes, S. R. Darvish, P. Kung, M. Razeghi, and R. J. Molnar, *Opto-Electron. Rev.*, **10,** (2002), 287.

[67] V. Adivarahan, J. Zhang, A. Chitnis, W. Shuai, J. Sun, R. Pachipulusu, M. Shatalov, and M. A. Khan, *Jpn. J. Appl. Phys.*, **41,** (2002), L435.

[68] W. H. Sun, J. P. Zhang, V. Adivarahan, A. Chitnis, M. Shatalov, S. Wu, V. Mandavilli, J. W. Yang, and M. A. Khan, *Appl. Phys. Lett.*, **85,** (2004), 531.

[69] K. Mayes, A. Yasan, R. McClintock, D. Shiell, S. R. Darvish, P. Kung, and M. Razeghi, *Appl. Phys. Lett.*, **84,** (2004), 1046.

[70] A. J. Fischer, A. A. Allerman, M. H. Crawford, K. H. A. Bogart, S. R. Lee, R. J. Kaplar, W. W. Chow, S. R. Kurtz, K. W. Fullerman, and J. J. Figiel, *Appl. Phys. Lett.*, **84,** (2004), 3394.

[71] Y. Xi, J.-Q. Xi, Th. Gessmann, J. M. Shah, J. K. Kim, E. F. Schubert, A. J. Fischer, M. H. Crawford, K. H. A. Bogart, and A. A. Allerman, *Appl. Phys. Lett.*, **86,** (2005), 031907.

[72] A. Yasan, R. McClintock, K. Mayes, D. Shiell, L. Gautero, S. R. Darvish, P. Kung, and M. Razeghi, *Appl. Phys. Lett.*, **83,** (2003), 4701.

[73] Y. Bilenko, A. Lunev, X. Hu, J. Deng, T. M. Katona, J. Zhang, R. Gaska, M. S. Shur, W. Sun, V. Adivarahan, M. Shatalov, and A. Khan, *Jpn. J. Appl. Phys.*, **44,** (2005), L98.

[74] A. A. Allerman, M. H. Crawford, A. J. Fischer, K. H. A. Bogart, S. R. Lee, D. M. Follstaedt, P. P. Provencio, and D. D. Koleske, *J. Cryst. Growth*, **272,** (2004), 227.

[75] H. Peng, E. Makarona, Y. He, Y.-K. Song, A. V. Nurmikko, J. Su, Z. Ren, M. Gherasimova, S.-R. Jeon, G. Cui, and J. Han, *Appl. Phys. Lett.*, **85,** (2004), 1436.

[76] C. D. McGuinness, K. Sagoo, D. McLoskey, and D. J. S. Birch, *Appl. Phys. Lett.*, **86,** (2005), 261911.

[77] C. D. McGuinness, A. M. Macmillan, K. Sagoo, D. McLoskey, and D. J. S. Birch, *Appl. Phys. Lett.*, **89,** (2006), 063901.

[78] E. W. Small, Laser Sources and Microchannel Plate Detectors for Pulse Fluorometry, in *Topics in Fluorescence Spectroscopy Volume 1: Techniques*, edited by J. R. Lakowicz, (Plenum Press, New York, 1991), pp. 97-182.

[79] A. R. West, *Basic Solid State Chemistry*, 2nd ed., (John Wiley & Sons Ltd., Chichester, 2000).

[80] T. Nishida and N. Kobayashi, *phys. stat. sol. (a)*, **176,** (1999), 45.

[81] J. Li, B. Nam, M. L. Nakarmi, J. Y. Lin, and H. X. Jiang, *Appl. Phys. Lett.*, **81,** (2002), 33653.

[82] K. H. Kim, Z. Y. Fan, M. Khizar, M. L. Nakarmi, J. Y. Lin, and H. X. Jiang, *Appl. Phys. Lett.*, **85,** (2004), 4777.

[83] H. Daulet, P. Deschamps, B. Dion, A. D. MacGregor, D. MacSween, R. J. McIntyre, C. Trottier, and P. P. Webb, *Appl. Optics*, **32,** (1993), 3894.

[84] J. P. Zhang, A. Chitnis, V. Adivarahan, S. Wu, V. Mandavilli, R. Pachipulusu, M. Shatalov, G. Simin, J. W. Yang, and M. A. Khan, *Appl. Phys. Lett.*, **81,** (2002), 4910.

[85] M. Shatalov, A. Chitnis, V. Mandavilli, R. Pachipulusu, J. P. Zhang, V. Adivarahan, S. Wu, G. Simin, M. A. Khan, G. Tamulaitis, A. Sereika, I. Yilmaz, M. S. Shur, and R. Gaska, *Appl. Phys. Lett.*, **82,** (2003), 167.

[86] X. M. He and D. C. Carter, *Nature*, **358,** (1992), 209.

[87] S. Sugio, A. Kashima, S. Mochizuki, M. Noda, and K. Kobayashi, *Protein Eng.*, **12,** (1999), 439.

[88] F. C. Bernstein, T. F. Koetzle, G. J. Williams, E. E. Meyer Jr, M. D. Brice, J. R. Rogers, O. Kennard, T. Shimanouchi, and M. Tasumi, *J. Mol. Biol.*, **112,** (1977), 535.

[89] K. K. Flora and J. D. Brennan, *Chem. Mater.*, **13,** (2001), 4170.

[90] X. Sui, J. A. Cruz-Aguado, Y. Chen, Z. Zhang, M. A. Brook, and J. D. Brennan, *Chem. Mater.*, **17,** (2005), 1174.

[91] N. Nassif, O. Bouvet, M. N. Rager, C. Roux, T. Coradin, and J. Livage, *Nature Mater.*, **1,** (2002), 42.

[92] D. J. S. Birch, A. Ganesan, and J. Karolin, *Synth. Met.*, **155,** (2005), 410.

[93] F. Hussain, D. J. S. Birch, and J. C. Pickup, *Anal. Biochem.*, **339,** (2005), 137.

[94] K. M. Hirshfield, D. Toptygin, G. Grandhige, H. Kim, B. Z. Packard, and L. Brand, *Biophys. Chem.*, **62,** (1996), 25.

[95] Y. Kabuyama, M. K. Homma, T. Kurosaki, and Y. Homma, *Eur. J. Biochem.*, **269,** (2002), 664.

[96] K. Vos, A. van Hoek, and A. J. W. G. Visser, *Eur. J. Biochem.*, **165,** (1987), 55.

[97] R. H. Khan, A. Naeem, and M. A. Baig, *Cell. Mol. Biol. Lett.*, **10,** (2005), 61.

[98] G. N. Reeke Jr., J. W. Becker, and G. M. Edelman, *J. Bio. Chem.*, **250,** (1975), 1525.

[99] P. Martel, S. M. Kim, and B. M. Powell, *Biophys. J.*, **31,** (1980), 371.

[100] R. T. A. MacGillivray, E. Mendez, S. K. Sinha, M. R. Sutton, J. Lineback-Zins, and K. Brew, *Proc. Nat. Acad. Sci. USA*, **79,** (1982), 2504.

[101] R. Ballerstadt and J. S. Schultz, *Sensor. Actuat. B-Chem.*, **46,** (1998), 50.

[102] R. J. Russell, M. V. Pishko, C. C. Gefrides, M. J. McShane, and G. L. Cote, *Anal. Chem.*, **71,** (1999), 3126.

[103] O. J. Rolinski, D. J. S. Birch, L. J. McCartney, and J. C. Pickup, *Phys. Med. Biol.*, **46,** (2001), N221.

[104] L. J. McCartney, J. C. Pickup, O. J. Rolinski, and D. J. S. Birch, *Anal. Biochem.*, **292,** (2001), 216.

[105] S. D'Auria, N. DiCesare, M. Staiano, Z. Gryczynski, M. Rossi, and J. R. Lakowicz, *Anal. Biochem.*, **303,** (2002), 138.

[106] S. S. Lehrer, *J. Bio. Chem.*, **244,** (1969), 3613.

[107] W. Breuer and Z. I. Cabantchik, *Anal. Biochem.*, **299,** (2001), 194.

[108] M. S. Navati, U. Samuni, P. Aisen, and J. M. Friedman, *Proc. Nat. Acad. Sci. USA*, **100,** (2003), 3832.

[109] M. R. Eftink, Fluorescence Techniques for Studying Protein Structure, in *Protein Structure Determination*, edited by C. H. Suelter, (John Wiley & Sons, New York, 1991), pp. 127-205.

[110] H. Du, R. A. Fuh, J. Li, L. A. Corkan, and J. S. Lindsey, *Photochem. Photobiol.*, **68,** (1996), 141.

[111] E. Leroy, H. Lami, and G. Laustriat, *Photochem. Photobiol.*, **14,** (1971), 411.

[112] A. Rzeska, J. Malicka, K. Stachowiak, A. Szymañska, L. Lankiewicz, and W. Wiczk, *J. Photochem. Photobiol. A: Chem.*, **140,** (2001), 21.

[113] J. P. Duneau, N. Garner, G. Cremel, G. Nullans, P. Hubert, D. Genest, M. Vincent, J. Gallay, and M. Genest, *Biophys. Chem.*, **73,** (1998), 109.

[114] W. R. Laws, J. B. A. Ross, H. R. Wyssbrod, J. M. Beechem, L. Brand, and J. C. Sutherland, *Biochem.*, **25,** (1986), 599.

[115] B. Barbieri, E. Terpetschnig, and D. M. Jameson, *Anal. Biochem.*, **344,** (2005), 298.

[116] P. Vita, N. Kurilcik, S. Juršenas, A. Žukauskas, A. Lunev, Y. Bilenko, J. Zhang, X. Hu, J. Deng, T. Katona, and R. Gaska, *Appl. Phys. Lett.*, **87,** (2005), 084106.

[117] C. J. Brinker and G. W. Scherer, *The Physics and Chemistry of Sol-Gel Processing*, (Academic Press, New York, 1990).

[118] J. D. Brennan, *Appl. Spectrosc.*, **53,** (1999), 106A.

[119] M. Vallet-Regí, *J. Chem. Soc., Dalton Trans.*, **2,** (2001), 97.

[120] S. Braun, S. Rappoport, R. Zusman, D. Avnir, and M. Ottolenghi, *Mater. Lett.*, **10,** (1990), 1.

[121] W. Jin and J. D. Brennan, *Anal. Chim. Acta*, **461,** (2002), 1.

[122] L. C. Klein, *Ann. Rev. Mater. Sci.*, **15,** (1985), 227.

[123] M. Ebelmen, *Ann. Chemie Phys.*, **16,** (1846), 129.

[124] M. Ebelmen, *C. R. Acad. Sci.*, **25,** (1847), 854.

[125] T. Graham, *J. Chem. Soc.*, **17,** (1864), 318.

[126] L. L. Hench and J. K. West, *Chem. Rev.*, **90,** (1990), 33.

[127] R. A. Assink and B. D. Kay, *Ann. Rev. Mater. Sci.*, **21,** (1991), 491.

[128] J. E. Martin and D. Adolf, *Ann. Rev. Phys. Chem.*, **42,** (1991), 311.

[129] R. K. Iler, *The Chemistry of Silica*, (John Wiley & Sons Ltd., New York, 1955).

[130] P. B. Jamieson and L. S. Dent Glasser, *Acta Cryst.*, **20,** (1966), 373.

[131] P. B. Jamieson and L. S. Dent Glasser, *Acta Cryst.*, **20,** (1966), 688.

[132] P. B. Jamieson and L. S. Dent Glasser, *Acta Cryst.*, **22,** (1967), 507.

[133] M. Tanaka and K. Takahashi, *Anal. Sci.*, **15,** (1999), 1241.

[134] R. J. P. Corriu and D. Leclercq, *Angew. Chem. Int. Ed.*, **35,** (1996), 1420.

[135] U. Narang, R. Wang, P. N. Prasad, and F. V. Bright, *J. Phys. Chem*, **98,** (1994), 17.

[136] M. L. Ferrer, F. del Monte, and D. Levy, *Chem. Mater.*, **14,** (2002), 3619.

[137] A. V. Rao and M. M. Kulkarni, *Mater. Chem. Phys.*, **77,** (2002), 819.

[138] E. A. V. Ebsworth, D. W. H. Rankin, and S. Cradock, *Structural Methods in Inorganic Chemistry*, 2nd ed., (Blackwell Scientific Publications, Oxford, 1991).

[139] Communication with Dr. J. A. Parkinson, NMR Specialist, Dept. of Pure & Applied Chemistry, University of Strathclyde.

[140] S. Fennouh, S. Guyon, C. Jourdat, J. Livage, and C. Roux, *C. R. Acad. Sci. Paris, t. 2, Serie II C*, **2,** (1999), 625.

[141] D. S. Gottfried, A. Kagan, B. M. Hoffman, and J. M. Friedman, *J. Phys. Chem. B*, **103,** (1999), 2803.

[142] D. Tleugabulova, J. Sui, P. W. Ayers, and J. D. Brennan, *J. Phys. Chem. B*, **109,** (2005), 7850.

[143] X. Sui, T. -Y. Lin, D. Tleugabulova, Y. Chen, M. A. Brook, and J. D. Brennan, *Chem. Mater.*, **18,** (2006), 887.

[144] C. B. Wilson, *Br. Med. J.*, **319,** (1999), 1288.

[145] J. C. Pickup, *Lancet*, **355,** (2000), 426.

[146] The Diabetes Control and Complications Trial Research Group, *J. Am. Med. Assoc.*, **276,** (1996), 1409.

[147] J. C. Pickup, L. J. McCartney, O. J. Rolinski, and D. J. S. Birch, *Br. Med. J.*, **319,** (1999), 1289.

[148] J. C. Pickup, F. Hussain, N. D. Evans, and N. Sachedina, *Biosens. Bioelectron.*, **20,** (2005), 1897.

[149] O. J. Rolinski, D. J. S. Birch, L. J. McCartney, and J. C. Pickup, *J. Photochem. Photobiol. B: Biol.*, **54,** (2000), 26.

[150] N. D. Evans, L. Gnudi, O. J. Rolinski, D. J. S. Birch, and J. C. Pickup, *Diabetes Technol. Therap.*, **5,** (2003), 807.

[151] N. D. Evans, L. Gnudi, O. J. Rolinski, D. J. S. Birch, and J. C. Pickup, *J. Photochem. Photobiol. B: Biol.*, **80,** (2005), 122.

[152] D. W. Piston and S. M. Knobel, *Trends Endocrinol. Metab.*, **10,** (1999), 413.

[153] S. A. Jaffari and J. C. Pickup, *Biosens. Bioelectron.*, **11,** (1996), 1167.

[154] M. R. Robinson, R. P. Eaton, D. M. Haaland, G. W. Koepp, E. V. Thomas, B. R. Stallard, and P. L. Robinson, *Clin. Chem.*, **38,** (1992), 1618.

[155] R. Ballerstadt, A. Polak, A. Beuhler, and J. Frye, *Biosens. Bioelectron.*, **19,** (2004), 905.

[156] L. Tolosa, H. Malak, G. Raob, and J. R. Lakowicz, *Sensor. Actuat. B-Chem.*, **45,** (1997), 93.

[157] J. S. Marvin and H. W. Hellinga, *J. Am. Chem. Soc.*, **120,** (1998), 7.

[158] L. Tolosa, I. Gryczynski, L. R. Eichhorn, J. D. Dattelbaum, F. N. Castellano, G. Rao, and J. R. Lakowicz, *Anal. Biochem.*, **267,** (1999), 114.

[159] K. Ye and J. S. Schultz, *Anal. Chem.*, **75,** (2003), 3451.

[160] T. D. James, K. R. A. S. Sandanayake, and S. Shinkai, *Angew. Chem. Int. Ed.*, **35,** (1996), 1910.

[161] S. D'Auria, P. Herman, M. Rossi, and J. R. Lakowicz, *Biochem. Biophys. Res. Commun.*, **263,** (1999), 550.

[162] K. U. Frohlich, K. D. Entian, and D. Mecke, *Gene*, **36,** (1985), 105.

[163] E. Kopetzki, K. D. Entian, and D. Mecke, *Gene*, **39,** (1985), 95.

[164] N. R. Lazarus, M. Derechin, and E. A. Barnard, *Biochem.*, **7,** (1968), 2390.

[165] J. R. Pringle, *Biochem. Biophys. Res. Commun.*, **39,** (1970), 46.

[166] A. Ramel, E. A. Barnard, and H. K. Schachman, *Angew. Chem. Int. Ed.*, **2,** (1963), 745.

[167] P. R. Kuser, S. Krauchenco, O. A. C. Antunes, and I. Polikarpov, *J. Bio. Chem.*, **275,** (2000), 20814.

[168] D. C. Kramp and I. Feldman, *Biochim. Biophys. Acta*, **537,** (1978), 406.

[169] W. S. Bennett and T. A. Steitz, *Proc. Nat. Acad. Sci. USA*, **75,** (1978), 4848.

[170] M. Forstner, M. Kriechbaum, P. Laggner, and T. Wallimann, *Biophys. J.*, **75,** (1998), 1016.

[171] H. Maity, N. C. Maiti, and G. K. Jarori, *J. Photochem. Photobiol. B: Biol.*, **55,** (2000), 20.

[172] I. Feldman and D. C. Kramp, *Biochem.*, **17,** (1978), 1541.

[173] H. Maity and G. K. Jarori, *Physiol. Chem. Phys. & Med. NMR*, **34,** (2002), 43.

[174] R. Filfil and T. V. Chalikian, *FEBS Lett.*, **554,** (2003), 351.

[175] L. Michaelis and M. Menten, *Biochem. Z.*, **49,** (1913), 333.

[176] R. E. Imhof, *Decay Analysis Software Support Manual*, 2nd ed., (IBH Consultants Ltd., Glasgow, 1989).

[177] J. B. Birks, *Phys. Rev.*, **94,** (1954), 1567.

[178] M. K. Santra, A. Banerjee, S. S. Krishnakumar, O. Rahaman, and D. Panda, *Eur. J. Biochem.*, **271,** (2004), 1789.

[179] J. C. Pickup, *Lancet*, **326,** (1985), 817.

[180] I. B. Hirsch, *Clin. Diabetes*, **19,** (2001), 2.